UNIVERSIDADE D
COIMBRA

Ricardo Jorge Ferreira Faustino

NEW MORPHOMETRIC BIOMARKERS OF THE CEREBELLUM BY MAGNETIC RESONANCE:
VALIDATION IN MACHADO-JOSEPH DISEASE

Tese de Doutoramento do Programa de Doutoramento em Ciências da Saúde, ramo de Ciências Biomédicas, orientada pelo Professor Doutor Miguel Castelo-Branco e pelo Professor Doutor Antero José Pena Afonso de Abrunhosa e apresentada à Faculdade de Medicina da Universidade de Coimbra.

Junho de 2020

Universidade de Coimbra

Faculdade de Medicina

New morphometric biomarkers of the cerebellum by magnetic resonance: validation in Machado-Joseph disease

Novos biomarcadores morfométricos do cerebelo por ressonância magnética: validação na doença de Machado-Joseph

Doctoral Thesis of the Doctoral Programme in Health Sciences, area of Biomedical Sciences, supervised by Miguel Castelo-Branco, MD PhD, and co-supervised by Antero José Pena Afonso de Abrunhosa, PhD, and presented to the Faculty of Medicine of the University of Coimbra

Tese de Doutoramento do Programa de Doutoramento em Ciências da Saúde, ramo de Ciências Biomédicas, orientada pelo Professor Doutor Miguel Castelo-Branco e pelo Professor Doutor Antero José Pena Afonso de Abrunhosa e apresentada à Faculdade de Medicina da Universidade de Coimbra

Ricardo Jorge Ferreira Faustino

Junho de 2020

The studies presented in this thesis were carried out at ICNAS (Institute of Nuclear Sciences Applied to Health) and IBILI (Institute for Biomedical Imaging and Life Sciences), Faculty of Medicine, University of Coimbra, Portugal, and supported by grants from: UID/NEU/04539/2013–COMPETE, POCI-01-0145-FEDER-007440, AND CENTRO-07-ST24-FEDER-00205, and the Portuguese Foundation For Science and Technology: FCT - SFRH/BD/69735/2010.

Á minha família

Agradecimentos

A realização de um projecto de doutoramento está condicionada pelo acesso às condições logísticas necessárias para a realização dos trabalhos definidos, mas sobretudo pela existência de massa crítica e de um ecossistema académico que permita o crescimento humano e científico de cada candidato. Nesse sentido, as minhas primeiras palavras de agradecimento vão para o Professor Doutor Miguel Castelo Branco, director do Instituto de Ciências Nucleares Aplicadas à Saúde, que me orientou na realização deste projecto no seio de uma instituição única em Portugal. O seu fascínio pelas neurociências foi, sem dúvida, um factor motivador para a realização deste projecto na área da neuroimagiologia.

Ao longo destes anos, tive a sorte de partilhar um caminho fantástico no mundo das ciências radiológicas, desde os bancos da faculdade até àquela que, um dia, seria a minha profissão: se alguém influenciou grandemente as minhas escolhas em matéria de ciência, de dedicação e persistência foi o Professor Doutor Antero Abrunhosa, sem dúvida, um dos meus mestres, a ele agradeço tudo o que fez por mim ao longo da minha formação académica.

Seria impossível não falar das amizades que se cultivam ao longo destes anos, os laços que se criaram com os colegas de doutoramento e os momentos de convívio que fazem parte destas vivencias. Obrigado a vós meus amigos por terem partilhado este caminho comigo. Um sincero obrigado ao Filipe Palavra, à Carla Pinto, à Margarida Coucelo, à Juliana Roda, à Leonor Ramos, à Helena Antunes, ao Rui Falacho, ao Miguel Marto, ao João Oliveira, ao Nuno Madeira, ao Ricardo Borges, ao André Lázaro, à Esmeralda Costa,ao Sérgio Leal, à Raquel Alves, ao Ricardo Morais, à Joana Silva, e à Vanessa Santos.

Agradeço também aos meus antigos colegas de profissão no ICNAS, que tornaram a minha vida em Coimbra mais interessante, permitindo-me crescer e ficar mais forte. Pelos momentos de convívio e partilha, sem dúvida que os primeiros anos foram um desafio do qual nos saímos muito bem.

Não poderia deixar de agradecer a todos aqueles que comigo participaram neste projecto, nomeadamente ao João Duarte pelo seu entusiasmo e humildade na ciência que faz, à equipa da Ressonância Magnética: Carlos Ferreira, César Nunes, Sónia

Afonso, João Paulo e Andreia Santos. Que os momentos de convívio tenham tempos de repetição elevados e tempo de eco inconfundíveis!

Ao João Pereira pela partilha, presença e apoio que jamais poderei esquecer, obrigado pela tua amizade.

Um profundo sentimento de gratidão e reconhecimento para a minha família, a começar pelos meus pais, pela sua presença e apoio constante apesar dos momentos difíceis porque passamos, mas que desde da minha infância apoiaram e encorajaram as minhas motivações e ambições académicas.

Ao meu irmão pelas partilhas, aventuras, brincadeiras, camaradagem, e a comunhão de um sentimento que só os irmãos podem entender, grande mano!

Aos meus sogros sempre presentes e disponíveis para ajudar, seria impossível pedir mais.

Aos meus restantes familiares, cujos nomes não irei citar por medo de me esquecer de alguém e cometer alguma injustiça, mas com um pensamento muito forte para os mais pequeninos!

Aos que já partiram, mas cuja memória não esquecemos.

Finalmente, à minha mulher, Liliana, com a qual partilho o caminho da vida, um caminho que é bem mais fácil quando olhamos para o lado e vemos quem amamos. Bem posso falar no plural, porque as nossas vidas jamais serão iguais agora que tu nasceste Leonor, basta olhar para ti e esperar pelo teu sorriso, e aí sim, todos os mistérios da vida se resumem numa só palavra… Amor.

Cooperatores veritatis

Contents

List of Abbreviations

[18F]-FDG	Fluorine-18-fluoro-2-deoxy-D-glucose
2D-FT	Two-dimensional Fourier transform
3D-FT	Three-dimensional Fourier transform
3D MP-RAGE	Three-dimensional magnetization-prepared rapid gradient-echo
AC-PC	Anterior commissure - posterior commissure
ANCOVA	Analysis of covariance
ATP	Adenosine triphosphate
ATXN3	Ataxin 3 protein
AUC	Area under the curve
BA	Brodmann area
BOLD	Blood oxygenation level dependent
CAG	CAG repeats expansions
CAV	Cerebellar activation volume
Cr	Creatine
CSF	Cerebrospinal fluid
DUB	Deubiquitinating enzyme
EPI	Echo-planar imaging
EPO	External progressive ophthalmoplegia
FDR	False discovery rate
FID	Free induction decay
FLAIR	Fluid attenuation inversion recovery
fMRI	Functional magnetic resonance imaging
FOV	Field of view
FWE	Family-wise error rate
FWHM	Full width at half maximum
GLM	General linear model
GM	Grey matter
GP	Phase encoding gradient

HRF	Hemodynamic response function
Hz	Hertz
kDa	Kilodalton
L-DOPA	Levodopa
LTG	Lamotrigine
MJD	Machado—Joseph disease
MNI	Montreal Neurological Institute
MP-RAGE	Magnetization-prepared rapid gradient-echo
MR	Magnetic resonance
MRI	Magnetic resonance imaging
MRS	Magnetic resonance spectroscopy
NAA	N-acetyl aspartate
NESSCA	Neurological Examination Score for the Assessment of Spinocerebellar Ataxia
NGF	Nerve growth factor
NT	Number of thumbs
OEF	Oxygen extraction fraction
PD	Proton density-weighted
PDB	Protein Data Bank
PET	Positron emission tomography
PolyQ	Polyglutamine
PTB	Psychophysics toolbox
rCBF	Regional cerebral blood flow
RCSB	Research Collaboratory for Structural Bioinformatics
REM	Rapid eye movement
RF	Radiofrequency
RFX	Random effects
RISCA	Biological and clinical characteristics of individuals at risk for spinocerebellar ataxia study
ROC	Receiver operating characteristic
ROI	Region of interest

SARA	Scale for assessment and rating of ataxia
SBMA	Spinobulbar muscular atrophy
SCA	Spinocerebellar ataxias
SD	Standard deviation
SE	Spin echo
SEM	Standard error of the means
siRNA	Small interfering RNA
SIRT1	Sirtuin-1
SMA	Supplementary motor area
SNR	Signal-to-noise ratio
SPM	Statistical parametric mapping
T_1	T_1-weighted
T_2	T_2-weighted
T_2*	T_2*-weighted
TAL	Talairach coordinates
TE	Echo time
TR	Repetition time
VBM	Voxel-based morphometry
VOI	Volume of interest
WM	White matter

Summary

The Machado–Joseph Disease (MJD), or type 3 spinocerebellar ataxia (SCA3), is an hereditary autosomal dominant and degenerative disease that was described for the first time among Portuguese individuals. This disease mainly affects the cerebellum, usually manifests between 50–70 years of age, and includes dysarthria and march ataxia.

The objective of this thesis was to develop a morphometric, in vivo, and non-invasive biomarker with high spatial resolution, sensitivity, and replicability for identification of cases with SCA3. The necessary focus on the effect on the cerebellum additionally benefits a better understanding of this structure, which is highly relevant, but is less studied compared to the rest of the brain.

This thesis includes functional magnetic resonance imaging (fMRI) that revealed reduced cerebellar activations in the initial stage of MJD suggesting that functional differences may occur even prior to early morphological alterations. We also identified compensatory phenomena, which were dependent on task difficulty. Particularly, the cerebellar activation volume decreased in patients with SCA3 after performing a functional paradigm that required participants to perform synchronous and asynchronous motor tasks.

A quantitative analysis of the morphometric transformations using magnetic resonance (MR) is useful for identification of early lesions and, above all, monitoring the progression of cerebellar diseases. However, the majority of the previous studies were carried out in advanced stages of the disease with low statistical power and/or signal/noise relation, which was overcome by a strong collaboration with the University Hospital and ICNAS technological facilities in Coimbra. Additionally, alterations identified in other studies were often analyzed as general group differences in the pathological profile instead of developing a biomarker, which was the primary objective of this thesis.

This study required the acquisition of high resolution MR images at 3T and the extraction of morphometric information using voxel-based morphometry (VBM), a whole brain analysis method to determine, without bias, an atrophy pattern facing a control group or correlated with genetic and clinical metrics. This analytical process was complemented by using a statistical classifier-based model to define the predictive values, sensitivity, and specificity in order to validate a method with clinical application, especially at the disease progression monitoring level.

The study was conducted using VBM to identify important areas of neurodegeneration in patients with SCA3, at the thalamus, cerebellum, parietal lobe (post-central gyrus), and the insular level.

To define a biomarker, ataxias were the models of choice, as their relationship with cerebellar pathology is known. The development of this morphometric biomarker is an important tool for the realization and monitoring of clinical assays whose observations enable the validation of the objective measures of their result, in order to, for example, identify pre-clinical alterations that may justify the treatment of mutation carriers without established disease.

Neuroimaging and neuropathology have consistently demonstrated cerebellar alterations. Here, we further aimed to discover whole-brain functional biomarkers based on parametric performance-level-dependent signals. The study was performed in 13 patients with early SCA3 and in 14 healthy participants. We used a combined parametric behavioral/functional neuroimaging design to investigate disease fingerprints, as a function of performance levels, coupled with structural MRI and VBM. The fMRI was designed to parametrically analyze behavior and neural responses to audio-paced bilateral thumb movements at temporal frequencies of 1, 3, and 5 Hz. Our performance-level-based design probing neuronal correlates of motor coordination found that neural activation and behavior show critical loss of parametric modulation, specifically in SCA3, associated with frequency-dependent cortico/subcortical activation/deactivation patterns. Cerebellar/cortical rate-dependent dissociation patterns could clearly differentiate between groups irrespective of grey matter loss. Our findings suggest a motor network functional reorganization and indicate a possible role of fMRI as a tool to monitor disease progression in SCA3. Accordingly, fMRI patterns proved to be potential biomarkers in early SCA3, as tested by receiver operating characteristic analysis of both behavior and neural activation at different frequencies. The sensitivity and specificity of discrimination analysis based on the blood oxygen level dependent (BOLD) signal in response to the applied parametric finger-tapping task were often significantly >80% in single regions-of-interest. Functional fingerprints based on cerebellar and cortical BOLD performance-dependent signal modulation can thus be combined diagnostic and/or therapeutic targets in hereditary ataxia.

Sumário

A doença de Machado-Joseph (MJD), ou ataxia espinocerebelosa do tipo 3 (SCA3), é uma doença hereditária autossómica dominante e degenerativa, descrita pela primeira vez entre Portugueses. Esta doença afecta principalmente o cerebelo e geralmente manifesta-se entre a quinta e sétima década de vida e inclui disartria e ataxia da marcha.

Pretendeu-se desenvolver um biomarcador morfométrico, *in vivo*, não invasivo, com elevada resolução espacial, sensibilidade e replicabilidade para a identificação de casos de SCA3. O necessário enfoque no cerebelo para o efeito tem o benefício adicional de ajudar à melhor compreensão desta estrutura, tão relevante mas menos estudada que o resto do cérebro.

Esta tese incluiu estudos de ressonância magnética funcional (fMRI), que revelaram uma diminuição das activações cerebelosas numa fase inicial da SCA3, o que sugeriu que diferenças funcionais podem ocorrer ainda antes de alterações morfológicas precoces. Nós também identificámos fenómenos compensatórios, que dependiam da dificuldade da tarefa. Em particular, observou-se a diminuição do volume de activação ao nível do cerebelo no grupo de doentes portadores de SCA3 após realizarem um paradigma funcional que exigia que os participantes realizassem tarefas motoras síncronas.

Uma análise quantitativa das alterações morfométricas por RM é útil na identificação de lesões precoces e, sobretudo, na monitorização da progressão de doenças do cerebelo. Contudo, a grande maioria dos estudos anteriores foram realizados em fases já relativamente avançadas da doença e com pouco poder estatístico e/ou baixa relação sinal/ruído, que foi ultrapassada pela forte colaboração com o Hospital Universitário e os meios tecnológicos existentes no ICNAS em Coimbra. Adicionalmente, as alterações identificadas noutros estudos foram frequentemente analisadas como uma diferença geral entre grupos, considerando o perfil patológico ao invés do desenvolvimento de um biomarcador, que era o principal objetivo desta tese.

Este estudo requereu a aquisição de imagens por RM de alta resolução, a 3T, e a extracção de informação morfométrica do cerebelo por VBM, um método de análise global do cérebro para determinar, sem enviesamentos, um padrão de atrofia face a um grupo de controlo ou correlacionado com alguma métrica genética ou clínica. Este

processo analítico foi complementado através do uso de um modelo baseado em classificadores estatísticos, para definir valores preditivos, sensibilidade e especificidade, e assim validar um método com aplicação clínica, em particular ao nível da monitorização de progressão da doença.

O estudo realizado por VBM permitiu identificar importantes áreas de neurodegeneração nos doentes portadores de SCA3/MJD, nomeadamente ao nível do tálamo, cerebelo, lobo parietal (giro pós-central) e insula.

Na definição de um biomarcador inovador, foram escolhidas as ataxias como modelo, dado que é conhecida a sua relação com a patologia cerebelosa. O desenvolvimento deste biomarcador morfométrico é uma ferramenta importante na realização e monitorização de ensaios clínicos, cujas observações permitem a validação de medidas objetivas de resultado dos mesmos, de forma a, por exemplo, identificar alterações pré-clínicas que podem justificar tratamento em portadores de mutações sem doença estabelecida.

A Neuroimagiologia e neuropatologia têm demonstrado consistentemente alterações cerebelares. Para além disso, pretendemos aqui descobrir biomarcadores funcionais do cérebro, com base em sinais paramétricos dependentes do nível de desempenho. O estudo foi realizado em 13 pacientes com SCA3 em fase inicial da doença e 14 participantes saudáveis. Utilizamos um desenho combinado de neuroimagiologia funcional/comportamental paramétrico para investigar as características das doenças, em função dos níveis de desempenho, juntamente com a ressonância magnética estrutural e a morfometria baseada em voxel. A ressonância magnética funcional (fMRI) foi projectada para analisar de forma paramétrica o comportamento e as respostas neurais aos movimentos do polegar bilateralmente com ritmo auditivo em frequências temporais de 1, 3 e 5 Hz. O desenho baseado no nível de desempenho que avaliou as correlações neuronais da coordenação motora possibilitou a descoberta que a activação neural e o comportamento apresentam uma perda crítica da modulação paramétrica especificamente no grupo SCA3, associado a padrões de activação/desactivação, córtico/subcortical, dependentes da frequência. Os padrões de dissociação dependentes da frequência cerebelar/cortical podem diferenciar-se claramente entre os grupos independentemente da perda de matéria cinzenta. Estes achados sugerem a reorganização funcional da rede motora e indicam um possível papel da fMRI como ferramenta para monitorizar a progressão da doença na SCA3. Consequentemente, os

padrões obtidos por fMRI provaram ser potenciais biomarcadores numa fase inicial da SCA3, conforme testado pela análise Receiver Operating Characteristic (ROC) dos comportamentos e da activação neural em diferentes frequências. A análise de discriminação baseada no sinal BOLD em resposta à tarefa motora paramétrica aplicada, atingiu valores estatisticamente significativos, >80%, de sensibilidade e especificidade em regiões de interesse únicas. As características funcionais baseadas na modulação do sinal dependente da performance BOLD a nível cerebral e cortical podem assim ser considerados alvos para o diagnóstico ou terapia na ataxia hereditária.

Author's contribution

The author contributed on the conception and experimental design of the study. He actively participated in the recruiting of patients and volunteers, which came from Coimbra University Hospitals' Neurogenetics Unity, and in the organization of demographic and molecular diagnosis data. The author also engaged with the study's participants, explaining its goals, using the approved informed consent.

The author actively participated in the participants' preparation and in the acquisition of structural and functional MR data; processed the imaging data thus collected, making the necessary corrections in order to use them for further analyses. He carried out the morphometric analyses using the VBM (Voxel-based morphometry) method, executing all the necessary steps of the process; he did the data preprocessing and performed the calculus of cerebellum activation volumes and whole brain statistical parametric maps, using the software Brainvoyager. Only the latter part was shared with the researcher João V. Duarte (JVD). The author carried out the data codification and the statistical analyses, and afterwards discussed and extracted new outcomes from parametric analyses. Ultimately, he wrote and discussed the article with the other authors, being the work in the chapters 4 and 5 of this thesis the result of the experimental work, and he produced the chapters 1, 2 and 3, with extensive professional revision concerning language that is now homogeneous across chapters. Revision of basic physics concepts was also carefully performed.

Contribuição do autor:

O autor contribuiu para a concepção e design experimental deste estudo. Ele participou activamente no recrutamento dos doentes e voluntários, provenientes da unidade de neurogenética, dos Hospitais da Universidade de Coimbra, e na organização dos dados demográficos e de diagnóstico molecular. O autor também acompanhou os participantes do estudo, explicando os objectivos do mesmo, fazendo uso do consentimento informado aprovado.

O autor participou activamente na preparação dos participantes e na aquisição dos dados de RM estrutural e funcional; tratou os dados imagiológicos obtidos, efectuando as correcções necessárias de forma a poderem ser usados nas posteriores análises. Ele realizou as análises morfométricas pelo método VBM (Voxel-based morphometry), efectuando todos os passos necessários; procedeu ao pré-processamento dos dados e cálculo dos volumes de activação do cerebelo e os mapas estatísticos paramétricos de todo o cérebro usando o software Brainvoyager. Somente a última parte foi realizada com a colaboração do investigador João V. Duarte (JVD). O autor efectuou a codificação dos dados e realizou a análise estatística, discutindo e apurando novos dados provenientes da análise paramétrica. Por fim, ele escreveu e discutiu o artigo em colaboração com os restantes autores, sendo os capítulos 4 e 5 o resultado desse trabalho experimental, e redigiu os capítulos 1, 2 e 3, com profunda revisão profissional no que concerne à linguagem tornando-a uniforme ao longo dos capítulos. Também foi realizada uma revisão cuidadosa dos conceitos básicos de física.

CHAPTER 1

Introduction

Introduction

The use of the word “ataxia” originates from the description of tabes dorsalis, in which, Guillaume Duchenne described it as being a locomotor ataxia (Vora and Lyons, 2004). Nowadays, this term is used to describe important changes in muscle coordination due to lesions present in the cerebellum and changes in the respective neuronal connections.

Ataxias are grouped into the following three groups:

- Hereditary
    - Autosomal recessive ataxias
    - Autosomal dominant ataxias
    - X-linked ataxias
    - Ataxias due to mitochondrial mutation
- Non-hereditary or sporadic
- Acquired ataxia

Spinocerebellar ataxias (SCA) are autosomal dominant-inherited ataxias. These conditions represent a heterogeneous group with late-onset symptoms and progressive neurodegenerative disorders, mainly characterized by cerebellar dysfunction and central and peripheral nervous system findings (Soong BW and Paulson HL, 2007; Carlson et al., 2009; Tsuji et al., 2008). Currently, 30 SCA subtypes have been identified globally and classified into the following three major categories in function of the observed mutation: polyglutamine ataxias, non-coding repeat ataxias, and ataxias caused by a conventional mutation in specific genes (Soong et al., 2007; Bettencourt and Lima, 2011; Bettencourt et al., 2007, 2008, 2010; Bettencourt and Lima, 2011).

The aim of this thesis is to develop and validate new morphometric and functional, magnetic resonance (MR) cerebellar biomarkers, with validation in spinocerebellar ataxia type 3 (SCA3), also known as Machado–Joseph disease (MJD). Cerebellar and brainstem dysfunction constitutes one of the most important neurological alterations, causing progressive gait imbalance and vestibular and speech difficulties, and have an important impact on a patient’s early life (young and mid-adulthood). To achieve the goal of this thesis, different methods are used to identify the cerebellar and brain regions affected and to analyze which regions relate to functional loss or, alternatively, compensatory brain dysfunctions. To perform *in vivo* brain studies, we used MR imaging. This medical imaging approach has played an important role in neuroscience

over the last few decades and has significantly improved our analysis of neuro-anatomy and physiology. Advanced neuroimaging has a major role in understanding and elucidating the pathophysiological mechanisms and providing fundamental methods that helped develop an imaging biomarker based on functional and structural data from patients with SCA3 and healthy participants. The development of this new biomarker is a potentially relevant feature for other types of ataxia and movement disorders like Parkinson disease; it is also a helpful tool for future clinical trials.

The first part of this introduction is focused on clinical and main genetic features, as well as on brain structure and function in SCA3 disease, which is the model used for validating the imaging biomarker developed and described in this thesis. The second part is dedicated to the contribution of different neuroimaging modalities applied for studying SCA3. Brain image processing techniques for analyzing anatomic and functional magnetic resonance (fMRI) data and their contribution on neuroscience research are also discussed.

The origin and first description of SCA3/MJD

SCA3 was first described in the early seventies upon studying the following three families of Portuguese Azorean ancestry: Machado, Thomas, and Joseph. The families of these Portuguese immigrants in Massachusetts, United States of America were studied by different researchers and the first conclusion pointed out the possibility of them being three independent diseases (Nakano et al., 1972; Woods et al., 1972; Rosenberg et al., 1976). In the following years, a new family of Azorean descent was described (Romanul et al., 1977), and the disease was described in other regions of the world, but without Azorean ancestry (Rosenberg, 1992).

Affected families living in both the Azores Islands and mainland Portugal have been newly identified, and the dissemination of description of clinical manifestation opened a way for the unification of all the characteristics into a single clinical entity. In fact, since then, MJD has been understood to be a single genetic disease with different phenotypic expressions. The genetic variability and clinical heterogeneity cause difficulty in the clinical classification of the disease (Coutinho and Andrade, 1978). The corollary of these important characteristic disease observations could define the following two important features in studies on MJD: inheritance as an autosomal dominant condition and a marked clinical heterogeneity (Bettencourt et al., 2007, 2008, 2010, 2011). Early descriptions classified the different phenotypes into three major clinical types. The first

type, also called “Joseph type,” shows an early onset of the disease and a rapid progression of symptoms, cerebellar ataxia, external progressive ophthalmoplegia (EPO), and pyramidal and extrapyramidal signs. In the second type, the “Thomas type,” the disease is characterized by an intermediate onset, cerebellar ataxia, and EPO; however, in this type, pyramidal signs may or may not be observed. In the third and last type, the “Machado type,” the disease has EPO and cerebellar ataxia along with peripheral alterations in some cases with minor pyramidal and extrapyramidal signs (Coutinho, 1992).

In some cases, a rare presentation of MJD with parkinsonian signs may be observed. According to some researchers, this points towards a possible fourth type of the condition (Suite et al., 1986). A fifth type was proposed with spastic paraplegia and no cerebellar ataxia (Sakai and Kawakami, 1996).

In Europe, throughout the nineties, genetic researchers believed to have discovered a new form of ataxia, which was denominated as SCA3. Further, the same genetic profile was discovered in MJD; hence, it was designated MJD/SCA3.

Epidemiology of MJD/SCA3

The SCAs are rare neurodegenerative diseases, with a very low prevalence estimated between 0.3 to 0.2 per 100,000. At present, 31 SCA types are known; but novel types are still being discovered by advanced genetic analysis.

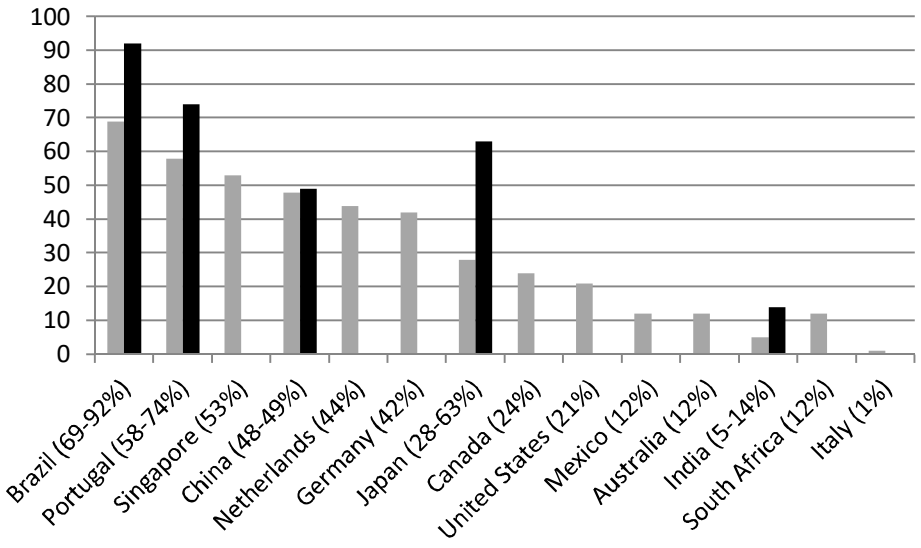

Figure 1: Relative frequency of MJD/SCA3 among SCAs (%). The MJD/SCA3 is most widely distributed worldwide, but the geographic distribution pattern of MJD/SCA3 is highly heterogeneous (Bettencourt et al., 2011).

The relative frequencies of MJD, among SCAs, have important geographic variation, with the disease being more common in Brazil, China, Germany, Japan, Netherlands, Portugal, and Singapore. It is relatively less common in Australia, Canada, India, Mexico, and the United States (Figure 1). In Italy and South Africa, it is considered to be relatively rare. In the Portugal mainland, MJD/SCA3 is relatively rare, (1/100000; with the exception of Tagus river valley); however, the highest prevalence (1/239) is seen in Flores Island (Azores; Bettencourt et al., 2011).

Diagnosis of SCA3

SCA3 is the most prevalent inherited cerebellar ataxia worldwide (Rüb et al., 2008). It is an autosomal dominant neurodegenerative disease caused by an expansion of the CAG sequence in the ATXN3 gene coding for the protein ataxin-3. Ataxin-3 has de-ubiquitinating properties and, in normal conditions, acts as a cytoplasmic protein in neurons. In a diseased brain, this subcellular distribution is altered, and the concentration of ataxin-3 is essentially localized in the nuclei of the neurons.

SCA3 is usually diagnosed using molecular genetic testing to detect an abnormal CAG trinucleotide repeat expansion in ATXN3. This molecular genetic test can detect all individual carriers of SCA3.

Allele sizes – The following allele sizes are observed in SCA3 (Costa and Paulson 2012; Padiath et al., 2005; Kawaguchi et al., 1994):

- Normal: Alleles with 12 to 44 CAG repeats. Overall, 93.5% normal alleles have fewer than 31 CAG repeats.
- Intermediate-length: Corresponds to the values between the normal and full-penetrance allele intervals. However, some of these alleles are not associated with the classic clinical features of SCA3. Until now, it was observed that the least unstable allele described, in terms of clinical consequences, had 45 CAG repeats).
    - Full-penetrance: Alleles of affected individuals with the classic SCA3 phenotype have approximately 60–87 CAG repeats.

Clinical features

SCA3, as described previously, has an important phenotypic heterogeneity. From an historical point of view and along the previous years of research, patients with SCA3 can be classified into five clinical subtypes (Table 1); however, some researchers do not

recognize the last two types. Due to the phenotypic heterogeneity (Figure 2), the classification of some patients into one of the five subtypes (Table 1) may be difficult and therefore not particularly useful from a practical point of view; however, the clinical features can be divided into motor and non-motor manifestations.

The subtype I is seen in 13% individuals and has a relationship with long disease-causing repeat alleles (Lu et al., 2004), showing earlier onset and characterized by dystonia and spasticity. The most common subtype, seen in 57% individuals, is the subtype II that is associated with a large diversity of disease-causing repeat alleles. This subtype is the most frequent phenotype and is manifested usually in the mid-adult years (Landau et al., 2000). The subtype III, seen in 30% individuals, is characterized by a late onset. This subtype is associated with short disease-causing repeat alleles. This subtype is characterized by the presence of ataxia and peripheral neuropathy (distal muscle atrophy and areflexia). The subtype IV is not associated with any particular repeat length or age of onset, and the main feature is the presence of a parkinsonian phenotype. Finally, some researchers have suggested that subtype V is similar to hereditary spastic paraplegia, but this classification has not been commonly accepted (Wang et al., 2009).

Table 1: Clinical subtypes and principal characteristics of Machado–Joseph disease.

Clinical subtype	Clinical characteristics
I	Prominent spasticity, rigidity, bradykinesia, and low ataxia.
II	Ataxia and upper motor neuron signs. Spastic paraplegia.
III	Ataxia and polyneuropathy.
IV	Dopa-responsive parkinsonism.
V	Hereditary spastic paraplegia.

Motor symptoms

The observed progressive ataxia in the different subtypes is due to cerebellar and brainstem dysfunction. The most common ocular system dysfunctions are diplopia, nystagmus, abnormal saccades (slow), jerky ocular pursuits, bulging eyes appearance, impaired vestibular-ocular reflex, and supranuclear vertical gaze palsy and ophthalmoplegia (Sequeiros and Coutinho, 1993; Coutinho, 1992 Takiyama et al., 1993;

Cancel et al., 1995; Sasaki et al., 1995; Durr et al., 1996; Igarashi, 1996; Matsumura et al., 1996; Schöls et al., 1996; Soong et al., 1997; Zhou et al., 1997; Watanabe et al., 1998; Friedman, 2002; Lin and Soong, 2002; Rüb et al., 2002a, b, 2003, 2004a, b, 2006; Friedman et al., 2003; Gordon et al., 2003; Bürk et al., 1996; De Oliveira et al., 2010; Vale et al., 2010; Horimoto et al., 2011).

Another important clinical feature in SCA3 is pyramidal dysfunction in patients with early onset and increased expansion of CAG repeats. When associated with the age of onset, this is responsible for the variability of symptom onset in patients as young as 5 years or as old as 70 years (Subramony and Currier, 1996). When the disease onset is early the ataxia symptoms are minimal, and the principal characteristics are bradykinesia, rigidity, and spasticity, corresponding to the clinical "Subtype I." The most frequent representation of disease occurs in the transition of young to mid-adulthood ("Subtype II"), showing progressive ataxia and upper motor signs. The late onset ("Subtype III") is represented by significant peripheral nerve involvement, which causes amyotrophy. In some studies, a "Subtype IV" has been described with parkinsonian characteristics; however, some researchers consider that there is "no obvious clinical utility in making these distinctions, the fact that different subtypes exist highlights the remarkable heterogeneity of MJD" (Paulson, 2012). However, if dystonia is the most specific movement disorder observed in MJD/SCA3, the parkinsonism represented in MJD/SCA3 favorably responds to L-dopa therapy (Rosenberg et al., 1992; Jardim et al., 2001; Munchau et al., 1999; Wilder-Smith et al., 2003; Gwinn-Hardy et al., 2003; Klockgether et al., 1999).

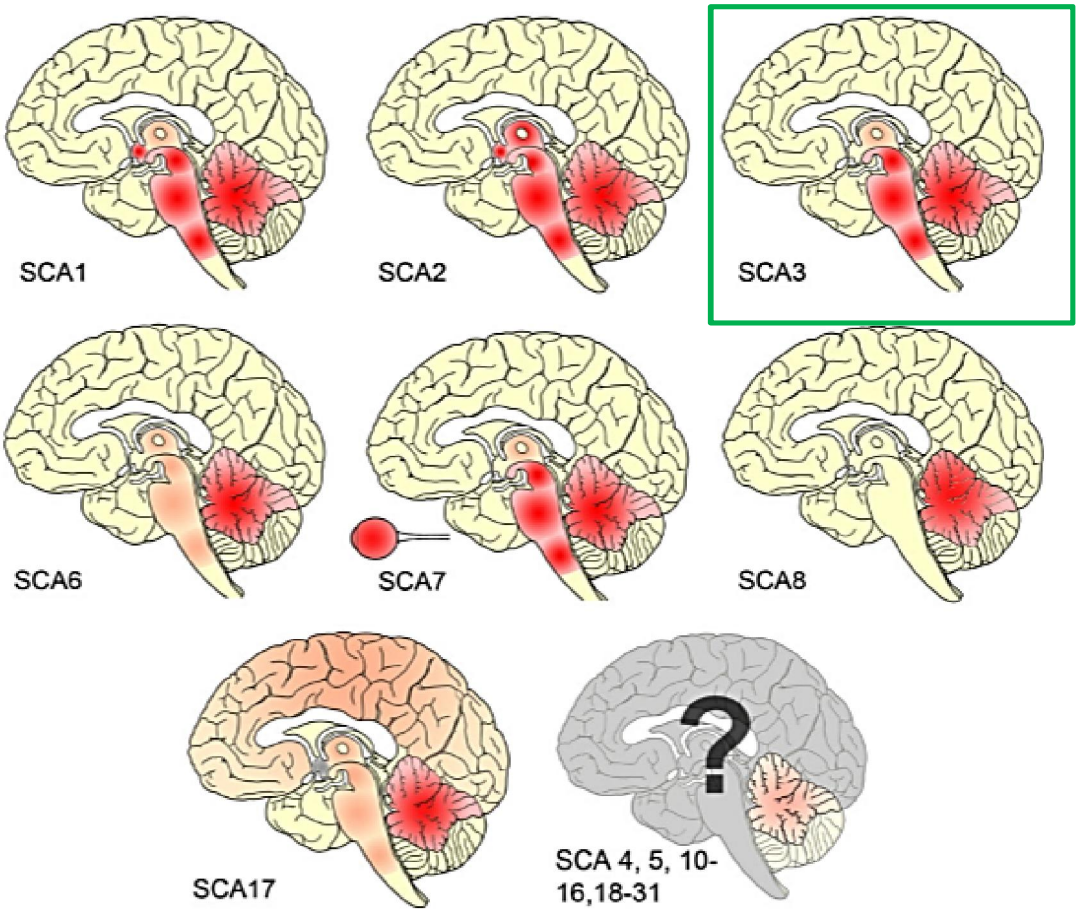

Figure 2: Schematic representation of neuronal loss patterns in SCA. Distribution of different types of spinocerebellar ataxias in the brain. The green box indicates the brain atrophy region in Machado—Joseph disease or SCA3. Adapted from: Seidel et al., 2012.

In MJD/SCA3, peripheral neuropathy is referred as being predominantly determined by duration of disease and present in old patients. The sensory fibers are most frequently affected with extensive areas of tactile and proprioceptive hypoesthesia. Patients can sometimes suffer from neuropathic pain. The handicaps are acquired and worsened by the presence of motor fiber damage, muscle atrophy, and fasciculations. In MJD/SCA3, autonomic manifestations like genitourinary and sudomotor systems disturbances are common (Schmitz-Hubsch et al., 2008; Yeh et al., 2005).

Non-motor symptoms

SCA3/MJD patients can suffer from non-motor symptoms; they can also show daytime sleepiness due to impaired nocturnal sleeping. These complaints can be divided into two sleep related disorders:

- Restless legs syndrome;
- Rapid eye movement (REM) sleep behavior disorders.

The restless legs syndrome is observed in 50% patients with SCA3/MJD. In REM sleep behavior disorders, when no muscle atonia is observed, patients suffer disturbed night sleep and insomnia (Friedman et al., 2003; Schöls et al., 1998; D´Abreu et al., 2009; Kawai et al., 2004; Zawacki et al., 2002; Cecchin et al., 2007; França et al., 2007, 2008; Friedman and Ammick, 2008). In patients with long disease duration fatigue maybe observed partly due to the above described symptomatology. In SCA3, it is also common to observe depressive symptoms, and psychotic symptoms have also been reported in few cases (Cecchin et al., 2007). Patients with SCA3 suffer from cramps and disabling symptoms (França et al., 2008), and chronic pain is a relevant clinical condition observed commonly in the lumbar region in 50% patients with SCA3 (França et al., 2007). Non-motor symptoms in SCA3 have important implications in patient life quality and may be under-recognized manifestations of the SCA3 disease (Zawacki et al., 2002).

Genetics of SCA3/MJD

Since the first study, the disease has been described as being a dominantly inherited genetic disorder (Nakano et al., 1972) and, years later, the gene was mapped to chromosome 14q32.1 (Figure 3; Takiyama et al., 1996). In 1994, the MJD1 gene was cloned and identified to be an unstable CAG repeat expansion in the coding region of the MJD1 gene, now identified as ATXN3. This trinucleotide repeat expansion (CAG) is localized in the 10^{th} exon and is responsible for an abnormally long polyglutamine (polyQ) tract in the encoded protein (near carboxyl terminus, 42 kDa protein), ataxin-3. Due to these genetic characteristics, MJD/SCA3 integrates to polyQ disorders like Huntington disease, spinobulbar muscular atrophy (SBMA), and SCA1 (Bettencourt, et al., 2010).

Figure 3: Diagram of the ATXN3 gene. SCA3 is caused by a mutation in the dynamic segment $(CAG)_n$ of the ATXN3 gene (Cr14q32.1).
Adapted from: http://www.genecards.org/cgi-bin/carddisp.pl?gene=ATXN3

In polyQ disorders, when the CAG repeat size exceeds a threshold length, the disease is expressed. In case of MJD/SCA3, the characteristic alleles have more than 51 repeats, and the normal alleles range vary between 12 and 47 repeats. In fact, these alleles are associated with a high risk of clinical manifestations of the disease. The phenotype is more severe in homozygote individuals than in heterozygous individuals, suggesting a possible dosage effect (Kawaguchi et al., 1994; Carvalho et al., 2008). In polyQ disorders, the mutation is unstable, and the repeat length increases at each parental transmission. This fact is responsible for an early disease onset with a severe phenotype in subsequent generations (Maruyama et al., 1995). The sporadic case of MJD/SCA3 ("de novo") is not evident in most cases.

Protein function

The 42 kDa Ataxin-3 protein (Figure 4) is expressed in the nucleus and cytoplasm of cells. It is a part of the protein quality control pathways in the cell, and this control is possible through interaction with the ubiquitin protein. Ataxin-3 is an enzyme that cleaves ubiquitin from ubiquitinated substrates and is also known as a deubiquitinating enzyme (DUB). Transcriptional regulation activities have also been proposed as a possible function of ataxin-3; however, the relationship between this mechanism and DUB activity is still unclear (Bettencourt et al., 2010; Costa and Paulson, 2012).

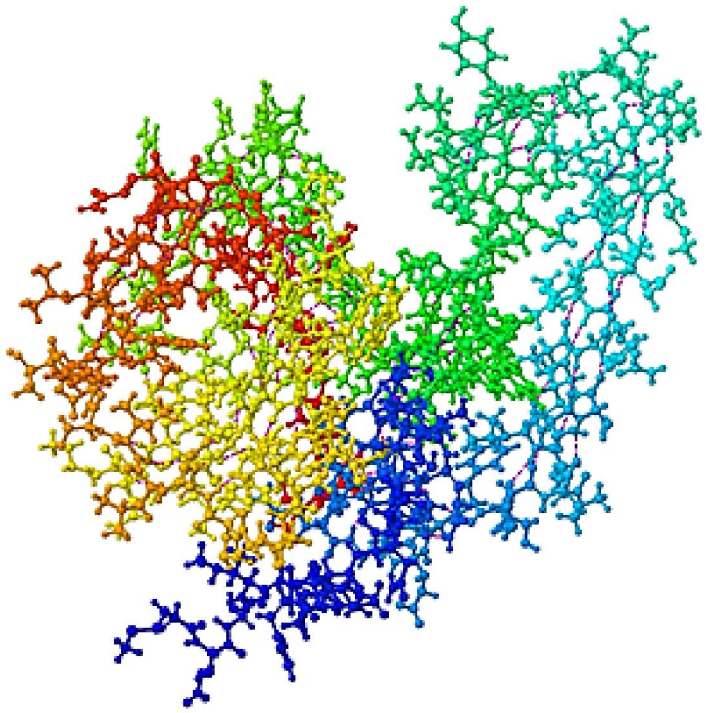

Figure 4: ATXN3 protein. Structure obtained from the Protein Data Bank (PDB) of the Research Collaboratory for Structural Bioinformatics (RCSB) and the article by Satoh et al., 2014, about the Mode of substrate recognition by the Josephin domain of ataxin-3, which has an endo-type deubiquitinase activity:
http://www.rcsb.org/pdb/explore/jmol.do?structureId=2DOS&bionumber=1

Phenotype in SCA3

The phenotype variations of SCAs are an important subject of research, which have been intensively studied in the past few decades. However, despite substantial effort to understand the mechanisms underlying early manifestations of the disease, many questions remain unanswered. Research focusing on the preclinical stage of neurodegenerative diseases like SCAs is increasing, thus improving the knowledge about the natural history of the disease. This is also relevant for designing new therapeutic strategies that can act before severe neurodegeneration occurs. In SCAs, CAG repeat mutation has a relatively high level of penetrance, and the studies performed in subjects without manifested disease can be an important window to analyze and characterize the range of subtle signs before clinical onset (Schmitz-Hubsch et al., 2008; Globas et al., 2008; Klockgether et al., 2011).

To identify morphological and functional brain modifications in the preclinical stage of different phenotypes before the onset of SCA (SCA1, SCA2, SCA3, and SCA6), a large

longitudinal observational study, also called the RISCA study, was performed to observe the biological and clinical characteristics of individuals at risk for spinocerebellar ataxia (Jacobi et al., 2013). For this purpose, 276 participants were enrolled at 14 European centers. To collect genetic information, anonymous genetic testing was performed to identify mutation carriers. Furthermore, clinical scales, questionnaires, performance-based coordination tests, and 1.5 T MRI scan acquisition were performed (in eight of 14 centers). In this study, carriers of SCA3 revealed a high rate of horizontal gaze-evoked nystagmus, but the frequency of double vision, dysphagia, urinary dysfunction, cognitive impairment, speech disturbances, handwriting difficulties, and vertigo did not differ between carriers and non-carriers of any mutation. When the cerebellar functional score was analyzed, the results showed a decreased score in participants closer to the age of onset in SCA2; but this relation was not significant in SCA3. Volumetric analysis was performed, and the results showed a small but non-significant loss of brainstem volume in SCA3 mutation carriers; the difference in cerebellar volumes compared with non-carriers was not significant. The MRI study suggested that brain structural modifications are present in preclinical mutation carriers, and the atrophy present in SCA1, SCA2, and SCA3 is more widespread and involves the brainstem. These data have important implications as they suggest that SCA mutation carriers have disease manifestations that might indeed be detected before the clinical onset of ataxia (Jacobi et al., 2013), paving the way for new avenues of clinical research.

Contribution of brain MR techniques

MRI has been considered an important imaging modality in the clinical assessment and research on SCA3. The principal findings in MRI are mainly atrophy of the pons, middle and superior cerebellar peduncles, frontal and temporal lobes, and the globus pallidus. Morphological changes can be observed in the midbrain and medulla oblongata. In these findings, r the interacting effects of age on atrophy of the pons and midbrain should be considered. The atrophy of the globus pallidus, and the temporal or occipital lobe was correlated with the disease duration (D'Abreu et al., 2010). The volumes of the cerebellum and cerebellar nuclei are also reduced (Stefanescu et al., 2015). Enlargement of the fourth ventricles is commonly described (Onodera et al., 1998). Yamada and colleagues described an abnormal linear high intensity of the globus

pallidus interna, using T2 weighted and fluid attenuation inversion recovery (FLAIR) sequences (Yamada et al., 2005).

In single-voxel proton MR spectroscopy (MRS) performed on the deep white matter in the superior-posterior region of the left hemisphere, which is localized at the level of the corpus callosum, a decrease in signal intensity of N-acetylaspartate relative to creatine-phosphocreatine signal (NAA/Cr) was seen in patients with SCA3 when compared to healthy controls. These observations suggest the presence of metabolic abnormalities in the deep white matter and possibly the manifestation of extensive neuronal and axonal damage in patients with SCA3 (D'Abreu et al., 2008).

Contribution of brain functional imaging

Stafanescu and colleagues performed 7 T fMRI studies to compare functional MR data of the cerebral cortex, cerebellar cortex, and dentate nuclei of SCA3, SCA6, and Friedreich's ataxia (Stefanescu et al., 2015). The behavior task was simply to perform an opening and closing movement using the right fist. The fist action was paced at 1.66 Hz by opening the fist to one tone and closing it to the next, using auditory and visual signals (projection screen of a background composed by two different colors). A 2 KHz tone was used. All subjects realized one fMRI run with alternating rest and active blocks. In this study, a relatively decreased fMRI signal (as compared to a control group) was observed in the cerebellar cortex, which was explained by the possibility of existence of spinocerebellar tracts degeneration, which is also observed in Friedreich's ataxia (Koeppen et al., 2013) and the decrease of synaptic Purkinje cell dendritic targets. In the patients with SCA3, the ventral areas of the dentate nuclei and posterolateral areas of the cerebellar hemisphere were more activated compared to those of the patients with Friedreich's ataxia and SCA6. Nonetheless, the fMRI activation of ventral dentate nucleus was statistically significant when the SCA3 group and the control group were compared. Another observation in these studies was that patients with SCA3 seemed to compensate the spinocerebellar dysfunction with pontocerebellar area activation. Although it is not statistically significant after correction for multiple comparisons when compared with the healthy controls, the neighboring BA44 and premotor cortex were activated. These fMRI studies reveal that pathology in SCA3 is not restricted to the cerebellar nuclei and includes a functional involvement of the cerebellar cortex, most importantly of the Crus I (Stefanescu et al., 2015). This is an important observation because this cerebellar cortical activation has an impact on

functional connections with the premotor cortex, as observed in macaques (Hashimoto et al., 2010).

Contribution of nuclear neuroimaging

Brain SPECT (single photon emission computed tomography) with ^{99m}Tc-hexylmethylpropylene amineoxine) showed perfusion changes in the parietal lobes, inferior portion of the frontal lobes, mesial and lateral portions of the temporal lobes, basal ganglia, and cerebellar hemispheres and vermis (Etchebehere et al., 2001).

Positron Emission Tomography (PET) is one of the most important imaging methods used to understand brain activity at the molecular level. Many studies have been performed in the past with important results about the physiopathology of different movement disorders. In this particular case, our attention is focused on MJD and how the first PET imaging acquisition performed with fluorine-18-fluoro-2-desoxy-D-glucose ([18F]-FDG) shows an important decrease in brain glucose metabolism in different brain regions, such as cerebral occipital cortex, brainstem, cerebellar vermis, and cerebellar hemispheres. In a PET study using [18F]-FDG, the lentiform nucleus and medulla showed diminished metabolism in patients with MJD. Fluorodopa and raclopride PET studies have also been performed in patients with MJD, and the results suggest that striatal D2 receptors seem to be preserved (Soong et al., 1997; Shinotoh et al., 1997).

Patient management and pharmacological therapies

Currently, there is no specific treatment for MJD/SCA3. The aim of the pharmacological approach used in the clinical routine is to minimize clinical symptoms like parkinsonism, spasticity, dystonia, and other motor (signal) complications. In a small number of patients with MJD/SCA3, clinical trials were performed to evaluate the efficiency of sulfamethoxazole and trimethoprim. The initial results were promising to treat spasticity, gait and coordination, but in contrast, a second study with a large number of patients with MJD/SCA3 revealed no significant effect, and the use of fluoxetine to recover the disability in these patients failed (Bezprozvanny and Klockgether, 2009; Bettencourt et al., 2011).

In a different clinical trial to study the lamotrigine (LTG) effect, a positive effect of gait disorder relief in patients with MJD/SCA3 was reported. To explain the significant benefits of LTG, researchers presented a hypothesis that LTG can suppress the mutant

ataxin-3 expression, which is also observed in MJD lymphoblastoid cells (Bezprozvanny, 2009; Bettencourt et al., 2011).

The use of tandospirone has showed a decrease in leg pain, mitigation of insomnia, ataxia, and depression levels in patients with MJD/SCA3; these results suggest that tandospirone may have significant benefits in treating these symptoms (Bezprozvanny et al., 2009; Bettencourt et al., 2011).

Recently, a new approach has been tested in transgenic MJD mice. In this experiment, MJD mice were submitted to caloric restriction that improved motor incoordination, imbalance, and associated neuropathology. Another effect of caloric restriction was the regulation of sirtuin-1 (SIRT1) levels in transgenic MJD mice, decreasing neuroinflammation and promoting autophagy. In this study, transgenic MJD mice were also treated with resveratrol to promote SIRT1 pharmacological activation, and the results showed an important reduction of motor incoordination. This therapeutic strategy can be useful, in the future, to stop and/or retard the progression of disease in patients with MJD/SCA3 (Cunha-Santos et al., 2016).

In the field of genetic therapy, promising results to treat autosomal dominant disorders have been obtained using small interfering RNA (siRNA). However, studies in ataxin-3 knockout models like mouse and the nematode *Caenorhabditis elegans* show no overt phenotypes, suggesting that ataxin-3 function maybe compensatorily replaced during development.

In the management of patients with MJD/SCA3, non-pharmacological healthcare measures like physiotherapy, speech therapy, occupational therapy, and physical aids (walkers and wheelchairs) may improve the quality of life.

References

Bettencourt C, Silva-Fernandes A, Montiel R, Santos C, Maciel P, Lima M: Triplet Repeats: Features, Dynamics and Evolutionary Mechanisms. In Recent Advances in Molecular Biology and Evolution: Applications to Biological Anthropology. Edited by: Santos C, Lima M. Kerala: Research Signpost; 2007:83-114.

Bettencourt C, Fialho RN, Santos C, Montiel R, Bruges-Armas J, Maciel P, Lima M: Segregation distortion of wild-type alleles at the MachadoJoseph disease locus: a study in normal families from the Azores islands (Portugal). J Hum Genet 2008, 53(4):333-339.

Bettencourt C, Santos C, Montiel R, Costa MC, Cruz-Morales P, Santos LR, Simões N, Kay T, Vasconcelos J, Maciel P, et al: Increased transcript diversity: novel splicing variants of Machado-Joseph Disease gene (ATXN3). Neurogenetics 2010, 11(2):193-202.

Bettencourt, C., & Lima, M. (2011). Machado-Joseph Disease: from first descriptions to new perspectives. Orphanet journal of rare diseases, 6, 35. doi:10.1186/1750-1172-6-35

Bezprozvanny I, Klockgether T. Therapeutic prospects for spinocerebellar ataxia type 2 and 3. Drugs of the future. 2009;34(12):10.1358/dof.2009.034.12.1443434. doi:10.1358/dof.2009.034.12.1443434.

Bürk K, Abele M, Fetter M et al (1996) Autosomal dominant cerebellar ataxia type I clinical features and MRI in families with SCA1, SCA2 and SCA3. Brain 119:1497-1505.

Cancel, G., Abbas, N., Stevanin, G., Durr, A., Chneiweiss, H., Néri, C., Duyckaerts, C., Penet, C., Cann, H.M., Agid, Y. and Brice, A.). Marked phenotypic heterogeneity associated with expansion of a CAG repeat sequence at the spinocerebellar ataxia 3/Machado-Joseph disease locus. Am. J. Hum. Genet. (1995) 57: 809-816.

Carlson KM, Andresen JM, Orr HT: Emerging pathogenic pathways in the spinocerebellar ataxias. Curr Opin Genet Dev 2009, 19(3):247-253.

Carvalho DR, La Rocque-Ferreira A, Rizzo IM, Imamura EU, Speck-Martins CE. Homozygosity enhances severity in spinocerebellar ataxia type 3. Pediatr Neurol. 2008;38:296-9

Costa, MC and Paulson, HL. Toward understanding Machado-Joseph Disease. Prog Neurobiol. 2012 May ; 97(2): 239-257.

Cecchin CR, Pires AP, Rieder CR, Monte TL, Silveira I, Carvalho T, Saraiva-Pereira ML, Sequeiros J, Jardim LB. Depressive symptoms in Machado-Joseph disease (SCA3) patients and their relatives. Community Genet. 2007;10:19-26.

Coutinho P, Andrade C: Autosomal dominant system degeneration in Portuguese families of the Azores Islands. A new genetic disorder involving cerebellar, pyramidal, extrapyramidal and spinal cord motor functions. Neurology 1978, 28(7):703-709.

Coutinho, P., 1992. Doença de Machado-Joseph: Tentativa de definição. Dissertação de Doutoramento, Instituto de Ciências Biomédicas Abel Salazar, Porto, pp.247.

Cunha-Santos J, Duarte-Neves J, Carmona V, Guarente L, Pereira de Almeida L, Cavadas C. Caloric restriction blocks neuropathology and motor deficits in Machado-Joseph disease mouse models through SIRT1 pathway. Nat Commun. 2016;7:11445. doi: 10.1038/ncomms11445.

D'Abreu A, França M Jr, Conz L, Friedman JH, Nucci AM, Cendes F, Lopes-Cendes I. Sleep symptoms and their clinical correlates in Machado-Joseph disease. Acta Neurol Scand. 2009;119:277-80.

D'Abreu A, França M Jr , Appenzeller S, Lopes-Cendes I, Cendes F. Axonal Dysfunction in the Deep. White Matter in Machado-Joseph Disease. J Neuroimaging. 2008 May 8.

D'Abreu A, Marcondes C França Jr, Henry L Paulson, Iscia Lopes-Cendes, . (2010) Caring for Machado-Joseph Disease: current understanding and how to help patients. Parkinsonism Relat Disord. 2010 January ; 16(1): 2.

De Oliveira MS, D'Abreu A, Franca MC Jr, Lopes-Cendes I, Cendes F, Castellano G: MRI-Texture Analysis of Corpus Callosum, Thalamus, Putamen, and Caudate in Machado-Joseph Disease. J Neuroimaging 2010.

Durr A, Stevanin G, Cancel G, Duyckaerts C, Abbas N, Didierjean O, Chneiweiss H, Benomar A, Lyon-Caen O, Julien J, et al: Spinocerebellar ataxia 3 and Machado-Joseph disease: clinical, molecular, and neuropathological features. Ann Neurol 1996, 39(4):490-499.

Etchebehere EC, Cendes F, Lopes-Cendes I, Pereira JA, Lima MC, Sansana CR, et al. Brain single photon emission computed tomography and magnetic resonance imaging in Machado-Joseph disease. Arch Neurol 2001;58:1257-63.

Friedman JH. Presumed rapid eye movement behavior disorder in Machado-Joseph disease (spinocerebellar ataxia type 3). Mov Disord. 2002 Nov;17(6):1350-3.

Friedman JH, Fernandez HH, Sudarsky LR. REM behavior disorder and excessive daytime somnolence in Machado-Joseph disease (SCA-3). Mov Disord. 2003 Dec;18(12):1520-2.

Friedman JH, Amick MM. Fatigue and daytime somnolence in Machado Joseph Disease (spinocerebellar ataxia type 3). Mov Disord. 2008 Jul 15;23(9):1323-4.

França MC Jr, D'Abreu A, Friedman JH, Nucci A, Lopes-Cendes I. Chronic pain in Machado-Joseph disease: a frequent and disabling symptom. Arch Neurol. 2007;64:176-70.

França MC, et al. Muscle Excitability Abnormalities in Machado-Joseph Disease. Arch Neurol 65(4), 2008. 525-529. 4

Gordon, CR, Joffe, V, Vainstein, G, Gadoth, N. Vestibulo-ocular arreflexia in families with spinocerebellar ataxia type 3 (Machado-Joseph disease).J Neurol Neurosurg Psychiatry.2003. 74-1403-1406.

Globas C, du Montcel ST, Baliko L, Boesch S, Depondt C, DiDonato S, Dürr A, Filla A, Klockgether T, Mariotti C, Melegh B, Rakowicz M, Ribai P, Rola R, Schmitz-Hubsch T, Szymanski S, Timmann D, Van de Warrenburg BP, Bauer P, Schöls L. Early symptoms in spinocerebellar ataxia type 1, 2, 3, and 6. Mov Disord. 2008;23:2232-8.

Gwinn-Hardy K, Singleton A, O'Suilleabhain P, Boss M, Nicholl D, Adam A, et al. Spinocerebellar ataxia type 3 phenotypically resembling parkinson disease in a black family. Arch Neurol. 2001;58:296-9.

Hashimoto M, Takahara D, Hirata Y, Inoue K, Miyachi S, Nambu A, Tanji J, Takada M, Hoshi E. Motor and non-motor projections from the cerebellum to rostrocaudally distinct sectors of the dorsal premotor cortex in macaques. Eur J Neurosci 2010; 31: 1402-13.

Horimoto Y, Matsumoto M, Akatsu H, Kojima A, Yoshida M, Nokura K, Yuasa H, Katada E, Yamamoto T, Kosaka K, et al: Longitudinal study on MRI intensity changes of Machado-Joseph disease: correlation between MRI findings and neuropathological changes. J Neurol 2011.

Igarashi S, Takiyama Y, Cancel G, Rogaeva EA, Sasaki H, Wakisaka A, Zhou YX, Takano H, Endo K, Sanpei K, et al: Intergenerational instability of the CAG repeat of the gene for Machado-Joseph disease (MJD1) is affected by the genotype of the normal chromosome: implications for the molecular mechanisms of the instability of the CAG repeat. Hum Mol Genet 1996, 5(7):923-932.

Jardim LB, Silveira I, Pereira ML, Ferro A, Alonso I, do Ceu Moreira M, Mendonca P, Ferreirinha F, Sequeiros J, Giugliani R: A survey of spinocerebellar ataxia in South Brazil - 66 new cases with MachadoJoseph disease, SCA7, SCA8, or unidentified disease-causing mutations. J Neurol 2001, 248(10):870-876.

Jacobi et al., Biological and clinical characteristics of individuals at risk for spinocerebellar ataxia types 1, 2, 3, and 6 in the longitudinal RISCA study: analysis of baseline data. Lancet Neurol 2013; 12: 650-58.

Kawai Y, Takeda A, Abe Y, Washimi Y, Tanaka F, Sobue G. Cognitive impairments in Machado-Joseph disease. Arch Neurol. 2004;61:1757-60.

Kawaguchi Y, Okamoto T, Taniwaki M, Aizawa M, Inoue M, Katayama S, Kawakami H, Nakamura S, Nishimura M, Akiguchi I. CAG expansions in a novel gene for Machado-Joseph disease at chromosome 14q32.1. Nat Genet. 1994;8:221-228.

Koeppen AH, Mazurkiewicz JE. Friedreich ataxia: neuropathology revised. J Neuropathol Exp Neurol 2013; 72: 78-90.

Koeppen AH, Ramirez RL, Bjork ST, Bauer P, Feustel PJ. The reciprocal cerebellar circuitry in human hereditary ataxia. Cerebellum 2013; 12: 493-503.

Klockgether T, Schols L, Abele M, et al. Age related axonal neuropathy in spinocerebellar ataxia type 3/Machado-Joseph disease (SCA3/MJD) J Neurol Neurosurg Psychiatry. 1999;66:222-4.

Klockgether T, Paulson H. Milestones in ataxia. Mov Disord (2011) 26:1134-1141.

Landau WM, Schmidt RE, McGlennen RC, Reich SG. Hereditary spastic paraplegia and hereditary ataxia, Part 2: A family demonstrating various phenotypic manifestations with the SCA3 genotype. Arch Neurol. 2000;57:733-9.

Lu CS, Chang HC, Kuo PC, Liu YL, Wu WS, Weng YH, Yen TC, Chou YH. The parkinsonian phenotype of spinocerebellar ataxia type 3 in a Taiwanese family. Parkinsonism Relat Disord. 2004;10:369-73.

Maruyama H, Nakamura S, Matsuyama Z, Sakai T, Doyu M , Sobue G, Seto M , Tsujihata M, Oh-i T, Nishio T, Molecular features of the CAG Repeats and Clinical Manifestation of Machado-Joseph Disease. Hum. Mol. Genet.4 (5)1995. 807-812.

Matsumura R, Takayanagi T, Murata K, Futamura N, Makito H, Ueno S. Relationship of (CAG)nC configuration to repeat instability of the Machado-Joseph disease gene. Hum Genet (1996) 98:643-645.

Munchau A, Dressler D, Bhatia KP, Vogel P, Zühlke C. Machado-Joseph disease presenting as severe generalised dystonia in a German patient. J Neurol. 1999;246:840-2.

Nakano KK, Dawson DM, Spence A: Machado disease. A hereditary ataxia in Portuguese emigrants to Massachusetts. Neurology 1972, 22(1):49-55.

Onodera O, Idezuka J, Igarashi S, Takiyama Y, Endo K, Takano H, Oyake M, Tanaka H, Inuzuka T, Hayashi T, Yuasa T, Ito J, Miyatake T, Tsuji S. Progressive atrophy of cerebellum

and brainstem as a function of age and the size of the expanded CAG repeats in the MJD1 gene in Machado-Joseph disease. Ann Neurol. 1998;43:288-96.

Padiath QS, Srivastava AK, Roy S, Jain S, Brahmachari SK. Identification of a novel 45 repeat unstable allele associated with a disease phenotype at the MJD1/SCA3 locus. Am J Med Genet B Neuropsychiatr Genet. 2005;133B:124-6.

Paulson H. Machado-Joseph disease/spinocerebellar ataxia type 3. Handb Clin Neurol (2012) 103: 437-449.

Lin KP, Soong BW. Peripheral neuropathy of Machado-Joseph disease in Taiwan: a morphometric and genetic study. Eur Neurol. 2002;48:210-7.

Romanul FC, Fowler HL, Radvany J, Feldman RG, Feingold M: Azorean disease of the nervous system. N Engl J Med 1977, 296(26):1505-1508.

Rosenberg RN, Nyhan WL, Bay C, Shore P: Autosomal dominant striatonigral degeneration. A clinical, pathologic, and biochemical study of a new genetic disorder. Neurology 1976, 26(8):703-714.

Rosenberg RN. Machado- Joseph disease: An autosomal dominant motor system degeneration. Movement disorders Journal. Volume 7, issue 3, 1992 pages 193-203.

Rüb U, Brunt ER, de Vos RA, Del Turco D, Del Tredici K, Gierga K, Schultz C, Ghebremedhin E, Bürk K, Auburger G, Braak H. Degeneration of the central vestibular system in spinocerebellar ataxia type 3 (SCA3) patients and its possible clinical significance. Neuropathol Appl Neurobiol. 2004a;30:402-14.

Rüb U, Brunt ER, Deller T. New insights into the pathoanatomy of spinocerebellar ataxia type 3 (Machado-Joseph disease). Curr Opin Neurol. 2008;21:111-6.

Rüb U, Bürk K, Schöls L, Brunt ER, de Vos RA, Diaz GO, Gierga K, Ghebremedhin E, Schultz C, Del Turco D, Mittelbronn M, Auburger G, Deller T, Braak H. Damage to the reticulotegmental nucleus of the pons in spinocerebellar ataxia type 1, 2, and 3. Neurology. 2004b;63:1258-63.

Rüb U, de Vos RA, Brunt ER, Sebesteny T, Schöls L, Auburger G, Bohl J, Ghebremedhin E, Gierga K, Seidel K, den Dunnen W, Heinsen H, Paulson H, Deller T. Spinocerebellar ataxia type 3 (SCA3): thalamic neurodegeneration occurs independently from thalamic ataxin-3 immunopositive neuronal intranuclear inclusions. Brain Pathol. 2006;16:218-27.

Sakai T, Kawakami H: Machado-Joseph disease: A proposal of spastic paraplegic subtype. Neurology 1996, 46(3):846-847.

Sasaki H, Wakisaka A, Takada A, et al. Mapping of the gene for MachadoJoseph disease within a 3.6-cm interval flanked by D14S291/D14S280 and D14S81, on the basis of studies of linkage and linkage disequilibrium in 24 Japanese families. Am J Hum Genet. 1995;56:231-24.

Schmitz-Hubsch T, Coudert M, Bauer P, Giunti P, Globas C, Baliko L, et al. Spinocerebellar ataxia types 1, 2, 3, and 6: disease severity and nonataxia symptoms. Neurology. 2008;71:982-9.

Sequeiros J, Coutinho P. Epidemiology and clinical aspects of Machado-Joseph disease. Adv Neurol. 1993;61:139-53.

Seidel K., et al. Brain pathology of spinocerebellar ataxias. Acta Neuropathol (2012) 124:1-21.

Soong B, Cheng C, Liu R and Shan D Machado-Josephdisease: Clinical, molecular, and metabolic characterizationin Chinese Kindreds. Ann Neurol (1997) 41:446-452.

Soong BW, Paulson HL: Spinocerebellar ataxias: an update. Curr Opin Neurol 2007, 20(4):438-446.

Suite ND, Sequeiros J, McKhann GM: Machado-Joseph disease in a Sicilian-American family. J Neurogenet 1986, 3(3):177-182.

Takiyama Y, Nishizawa M, Tanaka H, Kawashima S, Sakamoto H, Karube Y, Shimazaki H, Soutome M, Endo K, Ohta S, et al: The gene for MachadoJoseph disease maps to human chromosome 14q. Nat Genet 1993, 4(3):300-304.

Schöls L, Amoiridis G, Epplen JT, Langkafel M, Przuntek H, Riess O. Relations between genotype and pheotype in German patients with the Machado-Joseph disease mutation. J Neurol Neurosurg Psychiatry. 1996; 61:466-470.

Schöls L, Haan J, Riess O, Amoiridis G, Przuntek H. Sleep disturbance in spinocerebellar ataxias: is the SCA3 mutation a cause of restless legs syndrome? Neurology. 1998;51:1603-7.

Subramony SH, Currier RD. Intrafamilial variability in Machado-Joseph disease. Movement Disorders. 1996;11:741-743.

Stefanescu M, Moritz Dohnalek, Stefan Maderwald, Markus Thürling, Martina Minnerop, Andreas Beck, Marc Schlamann, Joern Diedrichsen, Mark E. Ladd, Dagmar Timmann; Structural and functional MRI abnormalities of cerebellar cortex and nuclei in SCA3, SCA6 and Friedreich's ataxia. Brain 2015; 138 (5): 1182-1197. doi: 10.1093/brain/awv064

Tsuji S, Onodera O, Goto J, Nishizawa M: Sporadic ataxias in Japan–a population-based epidemiological study. Cerebellum 2008, 7(2):189-197.

Vale J, Bugalho P, Silveira I, Sequeiros J, Guimaraes J, Coutinho P: Autosomal dominant cerebellar ataxia: frequency analysis and clinical characterization of 45 families from Portugal. Eur J Neurol 2010, 17(1):124-8.

Vora SK, Lyons RW. The Medical Kipling—Syphilis, Tabes Dorsalis, and Romberg's Test. Emerging Infectious Diseases. 2004;10(6):1160-1162. doi:10.3201/eid1006.AD1006.

Watanabe H, Tanaka F, Matsumoto M, Doyu M, Ando T, Mitsuma T, Sobue G. Frequency analysis of autosomal dominant cerebellar ataxias in Japanese patietns and clinical characterization of spinocerebellar ataxia 6. Clinical Genetics. 1998;53:13-19.

Wang YG, Du J, Wang JL, Chen J, Chen C, Luo YY, Xiao ZQ, Jiang H, Yan XX, Xia K, Pan Q, Tang BS, Shen L. Six cases of SCA3/MJD patients that mimic hereditary spastic paraplegia in clinic. J Neurol Sci. 2009;285:121-4.

Wilder-Smith E, Tan EK, Law HY, Zhao Y, Ng I, Wong MC: Spinocerebellar ataxia type 3 presenting as an L-DOPA responsive dystonia phenotype in a Chinese family. J Neurol Sci 2003, 213(1-2):25-28.

Woods BT, Schaumburg HH: Nigro-spino-dentatal degeneration with nuclear ophthalmoplegia. A unique and partially treatable clinicopathological entity. J Neurol Sci 1972, 17(2):149-166.

Yamada S, Nishimiya J, Nakajima T, Taketazu F. Linear high intensity area along the medial margin of the internal segment of the globus pallidus in Machado-Joseph disease patients. J Neurol Neurosurg Psychiatry. 2005;76:573-5.

Yeh TH, Lu CS, Chou YH, Chong CC, Wu T, Han NH, Chen RS. Autonomic dysfunction in Machado-Joseph disease. Arch Neurol. 2005;62:630-6.

Zawacki TM, Grace J, Friedman JH, Sudarsky L. Executive and emotional dysfunction in Machado-Joseph disease. Mov Disord. 2002;17:1004-10.

Zhou YX, Takiyama Y, Igarashi S, Li YF, Zhou BY, Gui DC,Endo K, Tanaka H, Chen ZH, Zhou LS, Fan MZ, Yang BX,Weissenbach J, Wang GX and Tsuji S Machado Joseph disease in four Chinese pedigrees: Molecular analysis of 15 patients including two juvenile cases and clinical correlations. Neurology (1997) 48:482-485.

CHAPTER 2

Fundamentals of magnetic resonance for the study of brain structure and function in Machado–Joseph disease

Introduction

Magnetic resonance is an important modality in medical imaging that has strongly transformed medical diagnosis in the last decades. This is essentially a non-invasive method that provides a unique contrast (often intrinsic) between biological tissues with a relatively high spatial resolution. These features make magnetic resonance imaging (MRI) the method of choice for *in vivo* studies focusing on brain anatomy and function.

This chapter is intended as an introduction to the methods of magnetic resonance used in this project, in order to assess anatomical and functional data of the brain in Machado–Joseph disease.

MR physical principles

The acquisition of MRI images is based on the selective excitation, by radiofrequency pulses, of susceptible nuclei exposed to a constant magnetic field. This interaction results in the emission of radiant energy by protons after returning to the initial energy state.

The nucleus of atoms comprises protons and neutrons that present energy quantification, which is described by specific quantum numbers. These abstract quantities tend to be interpreted resorting to classical examples such as the spin quantum number, which parametrizes the angular momentum of a rotating particle around an axis passing through its center. The spin of the nucleus depends on its specific composition. The resulting angular momentum of spin is parametrized by a quantum number varying at $\frac{1}{2}$ values and can be represented by the letter *I*. The *I* value depends on the number of nucleons and can be integral, half-integral (1/2, 3/2, etc.), and zero. For a nucleus ${}^{A}_{Z}X$ (Geraldes and Gil, 2002):

- *I* = 0, if Z and A are even numbers, such as ${}^{12}_{6}C$, ${}^{16}_{8}O$.
- *I* = integral values, if Z is odd and A is even, for example, ${}^{14}_{7}N$, ${}^{2}_{1}H$.
- *I* = half-integral values, if A is odd, for example *I*= $\frac{1}{2}$ for: ${}^{1}_{1}H$, ${}^{13}_{6}C$, ${}^{15}_{7}N$, ${}^{19}_{9}F$, ${}^{31}_{15}P$ and ${}^{195}_{78}Pt$.

In the absence of a magnetic field, the orientation of the individual nuclear magnetic moments can take any direction in space isotropically. However, the precession is a phenomenon that occurs whenever an object in rotation is influenced by an external magnetic field, B_0 and generates a momentum leading to the spin of the protons.

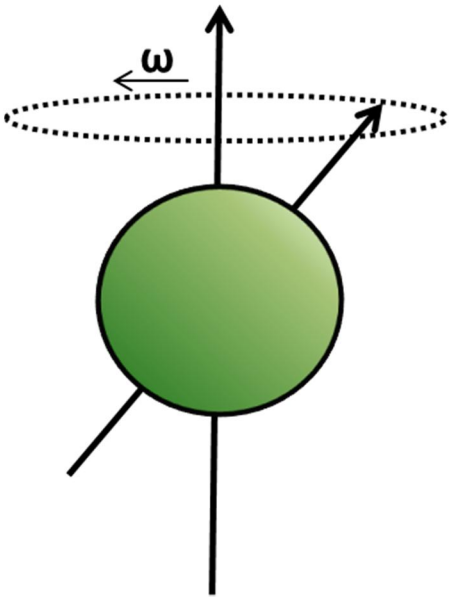

Figure 5: Nuclear spin. The spin precession movement in the presence of the external magnetic field β_0. This movement depends on a specific Larmor frequency (ω).

rotating around B_0. However, the magnetic dipoles of protons may show longitudinal and transverse components in relation to B_0. This styling movement is called precession of Larmor. Precession of the nuclei happens for a specific speed, proportional to the applied magnetic field strength. The frequency of rotation is constant and depends only on the species of the nucleus and the magnetic field. The following equation shows that Larmor frequency is directly proportional to the strength (B_0) of the magnetic field (Faustino, 2009; Buxton, 2013):

$$\omega_0 = \gamma B_0 \qquad \text{[equation 1]}$$

$$\text{or,} \quad \upsilon_0 = (\tfrac{\gamma}{2\pi})B_0 \qquad \text{[equation 2]}$$

where B_0 is the strength of the external magnetic field (measured in Tesla), ω_0 and υ_0 are the angular velocity and frequency (the latter in megahertz, MHz) of the precession, respectively, and γ is the gyromagnetic ratio (a constant specific to a particular nucleus) depending only on the given nucleus at B_0.

The gyromagnetic ratio for protons corresponds to γ = 42.58 MHz/T, which results in a Larmor frequency of 63.9 and 128 MHz at 1.5 and 3 T, respectively (common static magnetic fields used in MRI scanners).

From the exposition at B_0 field, nuclei can be grouped in two (sub-) proton nucleus populations (Zeeman interaction). The orientations that a nuclear magnetic moment can take when under an external magnetic field B_0 are lined either parallel or anti-parallel to

B_0 (Figure 6). These possible orientations present two energy levels, low and high energy (for parallel and anti-parallel orientations, respectively), and consequently determines the nuclear magnetization. In a situation of equilibrium, the nuclear magnetization has a parallel orientation to B_0, and its value, M_0, is proportional to the number of nuclei N and B_0.

In the presence of B_0 spin have different behavior, parallel orientation corresponds to the lower energy (spin up), and the antiparallel orientation corresponds to the higher energy (spin down) The proportion (number) of oriented spin is proportional to the strength of the magnetic field B_0 according to Boltzmann statistics. When the number of transitions from the low to the high energy state is equal to the number of transitions from the high to the low energy states, thermal equilibrium is said to be reached.

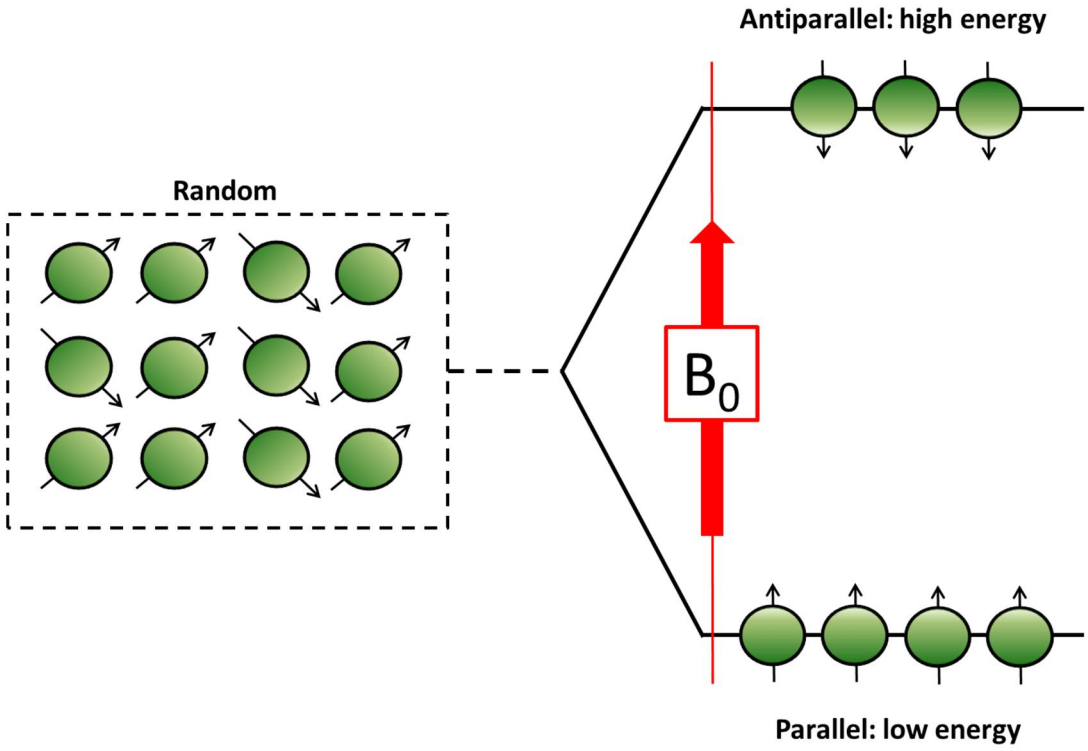

Figure 6: The two possible spin orientations, antiparallel and parallel. In the presence of an external magnetic field, spins have different behaviors according to the energy level (the difference of energy is proportional to B_0. The parallel orientation corresponds to the lower energy (spin up), and the antiparallel orientation corresponds to the higher energy (spin down).

The resonance phenomenon is described as the interaction between a radiofrequency (RF) wave and the spin precession. This phenomenon can be divided into two distinct phases: a first phase, called the excitation and a second relaxation phase. The signal used to create the MR images results from this interaction.

A powerful radio transmitter is able to generate an electromagnetic wave (with equal frequency as the Larmor frequency), which can be applied in a stable spin system through antenna coil positioning; this phenomenon is known as resonance condition.

Excitation of the spin system (or energy absorption) leads to transversal magnetization where the Z component of M_0 is tipped by a 90° pulse. After the pulse, transversal relaxation occurs, and the system starts to return to the equilibrium state.

Longitudinal magnetization is tipped into transverse plane (after RF pulse application), where spins rotate in the M_{xy} plane rather than in the $M_{z\ plane}$.

In the presence of longitudinal magnetization, the spins rotate or precess about the Z-axis, which induces an alternating signal with the same frequency as the Larmor frequency in the receiver coil: the MR signal. Spin excitation is portrayed in Figure 7.

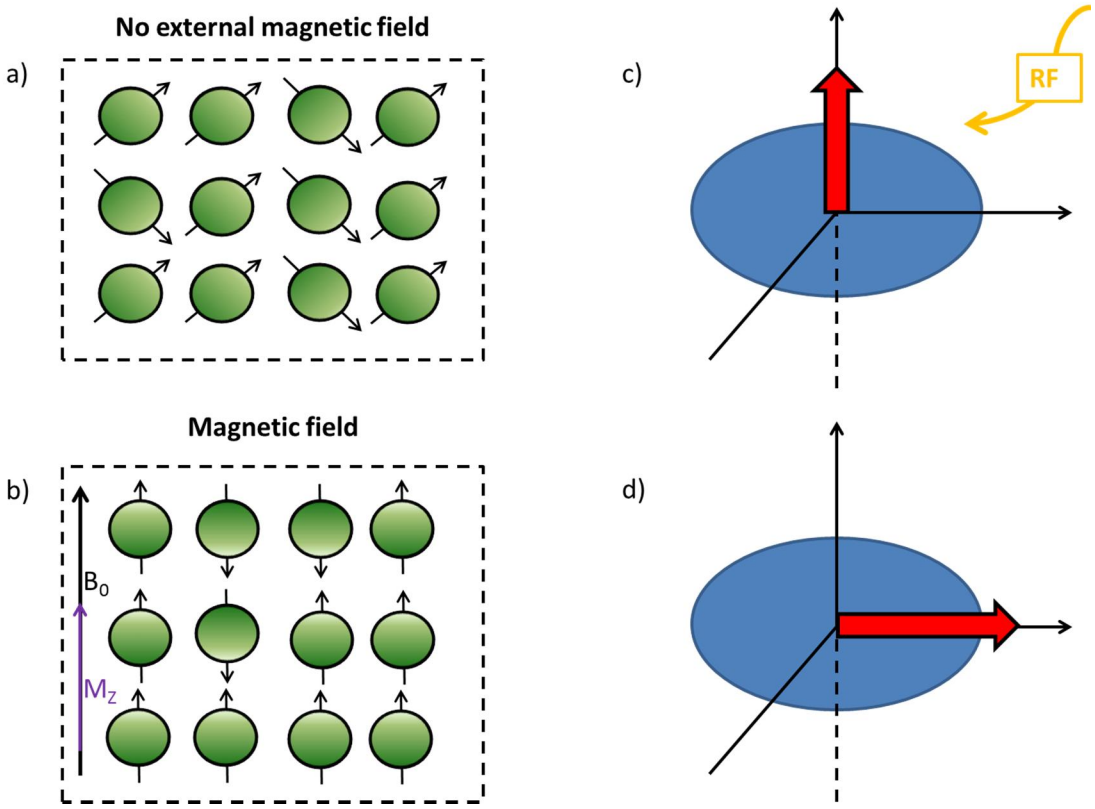

Figure 7(a–d): Spin excitation.. (a) No external magnetic field present, where spins rotate randomly about their axes. (b) Magnetic field application, where more spins are seen to align parallel to B_0 and producing longitudinal magnetization, M_z. (c) An RF pulse tips the magnetization vector by exactly 90º and (d) longitudinal magnetization flips over and rotates into transverse magnetization, M_{xy}.

Free Induction Decay (FID) refers to the signal received by the coil, and regarding hydrogen magnetic resonance, it possesses the following characteristics:

- Oscillation with the Larmor frequency and the applied magnetic field strength.
- FDI presents an initial magnitude proportional to the proton density (hydrogen nuclei).
- Time constant T_2 leads to a exponential decrease in amplitude because of of spin-spin relaxation.

Relaxation refers to proton energy release after the RF pulse has been absorbed by recovery of the original longitudinal magnetization (T1) and decay of transverse magnetization (T2). This is a fundamental MR feature as well as energy absorption, providing the primary mechanism for image contrast. Resonance absorption (by the proton) requires RF signal broadcast at the correct frequency. The equilibrium

arrangement of spin parallel and antiparallel to B_0 is disturbed by the additional energy. After excitation, protons release this added energy (relaxation phenomena) and return to their original state. This process is time-dependent and presents a rate constant (relaxation time).

Relaxation times, known as T_1 and T_2, are measured for the onset of spins, despite the fact that individual protons are responsible for energy absorption. Both relaxation times measure the transferred energy by an excited proton, but they diverge regarding the final energy disposition. In MRI principles, T_1, also known as spin lattice relaxation time and reflects the characteristic tissue-specific exponential time constant related with longitudinal magnetization (M_z) towards the equilibrium state, M_0. In detail, T_1 reflects the time M_z needs to regain 63% $(1 - 1/e)$ of its equilibrium value (Figure 8), immediately after the use of a 90° excitation pulse. This pulse is responsible to tip the longitudinal magnetization in the transverse plane and is represented by the following equation (Tavitian, 2007; Rinck, 2003):

$$M_z = M_0\,(1 - e^{-\frac{t}{T_1}}) \qquad \text{[equation 3]}$$

Where t corresponds to the time after the excitation pulse. T_1 occurs due to thermal energy transmission between the excited nuclei and the neighboring atomic elements. Efficiency of the mechanism involving energy transfer in molecules will determine a shorter (efficient means of energy transfer) or longer T_1 relaxation time.

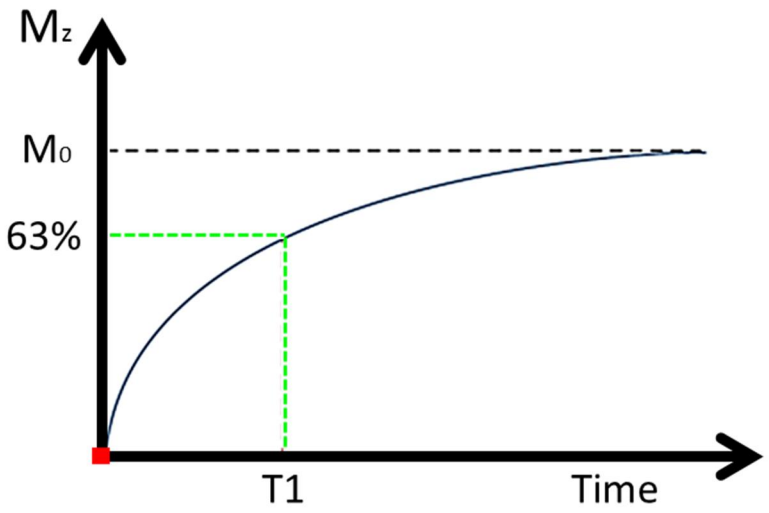

Figure 8: T_1 recovery curve. After a 90° excitation pulse, the time needed for longitudinal magnetization to regain 63% of its equilibrium value is expressed by the T_1 relaxation constant.

RF pulse application tips the longitudinal magnetization into the transverse plane, creating a transverse magnetization. Once the RF pulse is stopped, the transverse magnetization decays back to zero, and this situation is described by the time constant T_2 (Figure 9) and is detailed in the following equation (Tavitian, 2007):

$$M_{xy(t)} = M_{xy(0)}.e^{-\frac{t}{T2}} \qquad \text{[equation 4]}$$

Where t indicates the time right after the excitation pulse, and M_{xy} represents the time required for dissipating 63% of the initial transverse magnetization.

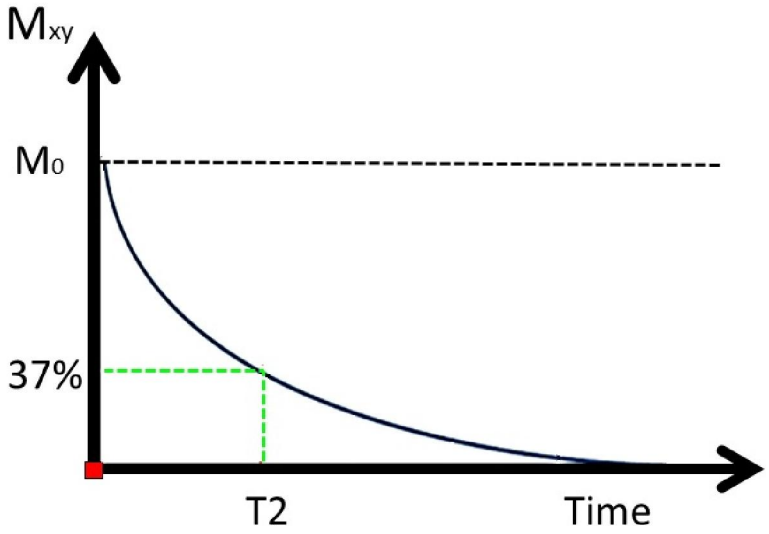

Figure 9: Graphical illustration of the T_2 decay curve. The necessary time for 37% of transverse magnetization decay to its original value is expressed by the T_2 relaxation constant, which is shorter than T_1.

Transverse coherence to *M* decreases due to many causes, and one of them is related to molecular motions of the adjacent spins.

When the protons are under a magnetic field, we can observe that transverse phase coherence is lost. B_0 nonuniformity arises from three sources:

1. *Main field inhomogeneity*. B_0 reveals a nonuniformity (constant during the measurement time) caused by imperfections in magnet production and interactions with metal sources or building walls nearby.

2. *Sample-induced inhomogeneity*. Tissues in close contact with different magnetic susceptibility or degrees of magnetic polarization are able to change the local magnetic field, mainly in their interface. With a static sample, this phenomenon possesses constant magnitude, as long as it remains inside the magnet.

3. *Imaging gradient*. Allows spatial localization and creates a transient inhomogeneity during the measurement, which actually leads to proton dephasing.

Afterwards, there is a faster than normal decrease in the MR signal, due to the contribution of T_2 with a decay constant T_2*.

In order to produce an image, it is necessary to combine RF pulses with magnetic field gradients (for slice selection and spatial encoding). Adjustment of these two important factors, as well as delay time, allows the transverse and longitudinal magnetization manipulation and consequently, the possibility to obtain specific image contrast by taking advantage of different T1 and T2 constants for different type of tissues (arrested below). In general, for data acquisition that will form an image, it is required to repeat a certain number of pulse sequence. The time for one cycle of a pulse sequence is called the repetition time (TR).

Spatial localization

Emitted signal encoding allows the contribution of nuclei spatial position in signal localization through the image reconstruction process. During image acquisition, the use of sets of magnetic field gradients spatially encodes the signal. The use of gradient coils (weaker than the static magnetic field) permits to superimpose a magnetic field gradient, and consequently allows for magnetic field variation. There are three types of gradient coils, each one with the capacity to form a linear variation in the static field along one of the axes x, y, and z. Consequently, the gradient that is produced corresponds to G_x, $G_{y,}$ and G_z, respectively. It is possible to generate a linear gradient in any direction by combining gradients along multiple axes at the same time, allowing to acquire an image in any orientation. Larmor frequency allows the spin position determination along the direction of an applied gradient. The image acquisition process involves four main steps:

1. Slice selection
2. Spatial encoding
3. Signal read-out
4. Image reconstruction

Slice Selection – the localization of slice selection or region of interest is possible due to the application of the linear magnetic field gradients along the three axes (x, y, and z). Two factors control the slice thickness: the amplitude of the magnetic fields affecting

the spatial distribution of the hydrogen nucleus resonant frequencies and the bandwidth of the RF pulse or the range of frequencies present in the pulse.

Spatial encoding – the second step involved in image formation is the identification of coordinated (position) of the hydrogen nucleus within the slice. For this purpose, two different gradients, G_y and G_x, must be applied as follows: the first in the phase-encoding direction (y-direction) and the second in the frequency-encoding direction (x-direction). When both gradients are applied to the frequencies in the x and y directions, they change spatially and the use of these gradients is the basis to calculate the inverse two-dimensional Fourier transformation needed to reconstruct the image.

Signal read-out – after the phase-encode, a signal is read out (spins with different coordinates will send out signals with different values of Larmor frequencies), and a frequency-encoding gradient is applied. Consequently, the position of spin can be calculated from the frequency of the signal when the read-out gradient is switched on.

Image reconstruction – to generate the MR images, two-dimensional k-space (2D k-space) fulfilled is needed; therefore, this operation must be repeated successively several times with different phase encoding gradient (GP) values. The k-space contains the data space that corresponds to the frequency representation of the MR image. The use of two-dimensional Fourier transform imaging (2D-FT) is the most common; however, three-dimensional Fourier transform (3D-FT) imaging can also be used.

To acquire resonance magnetic images with an optimal contrast, we need to control and optimize the timing parameters such as TE (echo time) and TR. The latter is the time between two excitation pulses of RF but can also be understood as the length of the relaxation period between RF pulses. This is why TR is so important to the T_1 contrast of images (Figure 10). In a long TR, the hydrogen nucleus (spin) rotate back in the z-plane, these phenomena are the explanation for the regrowth of longitudinal magnetization. In the presence of a short TR, the image contrast changes dramatically in T_1, and the tissues relax rapidly, contributing to a large signal after the subsequent RF pulse. The manipulations of TR allow controlling the level of T_1 weighting of the MR image.

Brain MR image contrast depends on the difference in physical properties among different types of tissues, and hence different T_1 and T_2 time constants. By carefully selecting the key acquisition parameters, TR and TE, it is not only possible to ensure that the acquired signal/FID is more influenced by T_1 or T_2 decay, but also to enhance the difference in signal between different tissues. For instance, since the T_1 time

constant for gray matter (GM) is higher (i.e. slower recovery) than that for white matter (WM), it is possible to choose TR to maximize this signal difference, yielding a T_1-weighted image, in which the GM signal is lower than the WM signal; similarly, as Cerebrospinal fluid (CSF) has a comparatively higher T_1 than both GM and WM, its signal upon acquisition is low, hence CSF is shown as black in T_1 images (Figure 10). However, T_2-weighted images are the opposite of T_1-weighted images (Figure 11): in the former, TE can also be chosen to optimally differentiate between different tissues, with the high T_2 constant for CSF meaning a low relaxation time and, therefore, a high signal.

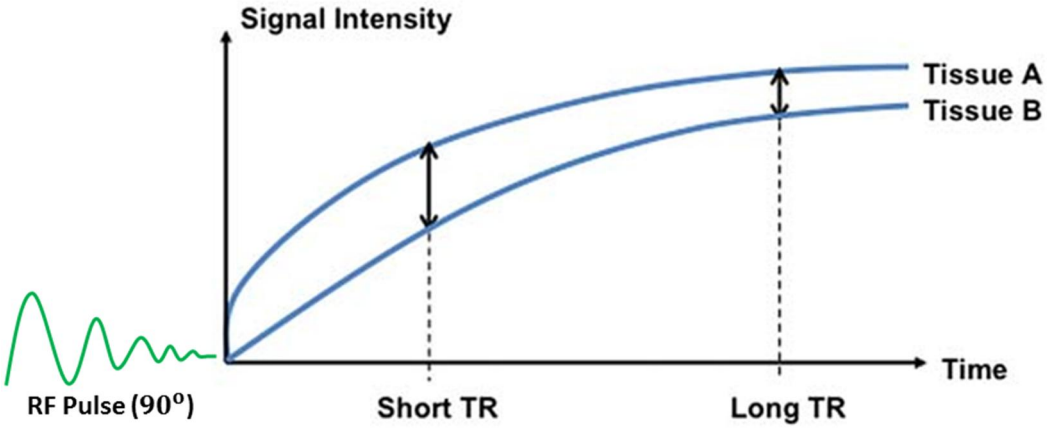

Figure 10: Schematic representation of TR and T_1 contrast correlation. When (A) a short TR is applied on a tissue with short T_1, a high longitudinal magnetization occurs, and a large MR signal is generated. However, with a long T_1, the result is the opposite (small MR signal difference). (B) If the applied TR is long, there are no differences in the signal, basically because the interval is long enough for regrowth of longitudinal magnetization in both tissues. (Adapted from Currie, 2012).

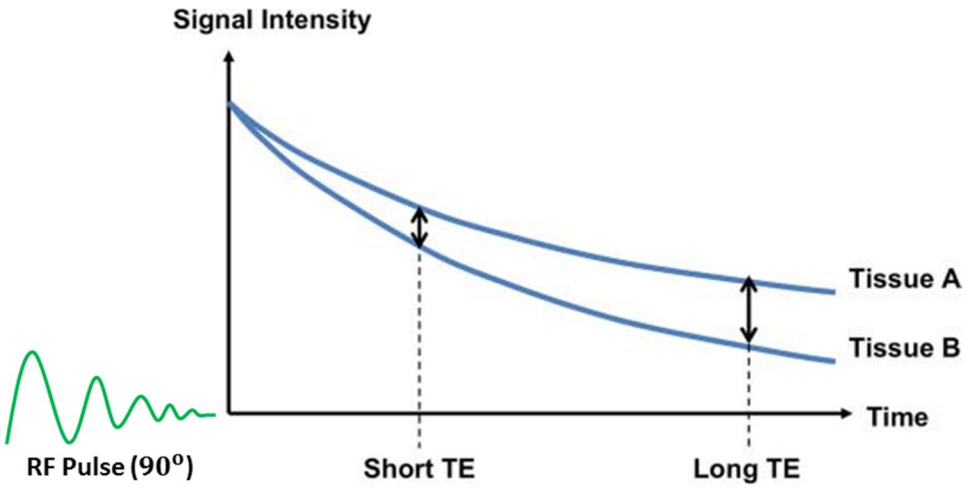

Figure 11: Graphical representation of the TE and T_2 contrast relationship. In the case of a short TE, the produced signal has no difference between two tissues with different T_2 times. On the other hand, for long TE, in a tissue with short T_2, the signal becomes dark (fast signal loss) although a long T_2 reveals a bright difference signal. (Adapted from Currie, 2012).

In MRI, the spin echo (SE) is one of the most used RF pulse sequences. The SE pulse sequence can be described as a 90º excitation pulse that is followed by a 180º rephrasing pulse, further followed by an echo. These mechanisms are on the basis of T_1, T_2, and proton density-weighted images. An SE is obtained when at time τ and a 90º RF pulse, a certain number of hydrogen nucleus (spin) dephasing happens due to B_0 inhomogeneity, and when a 180º RF pulse is applied, the spins precess in the opposite direction. The B_0 field inhomogeneity is still present; however, due to the reversal of the precessional direction, it rephases rather than dephasing the spins. Therefore, transverse magnetization refocuses, with full recovery occurring at time 2τ. Evidently, the SE sequence does not compensate for T_2 effects (spin-spin interactions), and the amplitude of the echo still exponentially decays with a T_2 time constant. In the SE sequence, the time taken for total refocusing (2τ) is the echo time (TE), and the time between 90º pulses is the TR. If more than one 180º pulse is used, more than one echo can be read out.

In a proton density (PD) weighted image, the contrast is principally due to differences in the number of hydrogen protons in the tissue (proton density), and T_1 and T_2 effects can be diminished if a long TR is selected for T_1 and a short TE for T_2 (Figure 12). In the presence of a small number of protons, the tissues are dark because low PD results in a

diminished component of transverse magnetization, resulting in a hypointense signal. The reverse is observed in the presence of high PD in tissues. In this case, the signal is hyper-intense because the high PD results in a large component of transverse magnetization. The features of a PD image with a high signal can be observed for CSF, synovial fluid, slow-flowing blood, infection, edema, cysts, and fat. Images with low or no PD signal are observed in air, fast-flowing blood, tendons, cortical bone, scar tissue, and calcifications. Therefore, to obtain PD weighted images, one should use a long TR in order of 4000 ms and a short TE in order of 20 ms to minimize the T_1 and T_2 image contrast, resulting in a PD contrast image (Tavitian et al., 2007; Rinck, 2003; Geraldes and Gil, 2002; Schild, 1990).

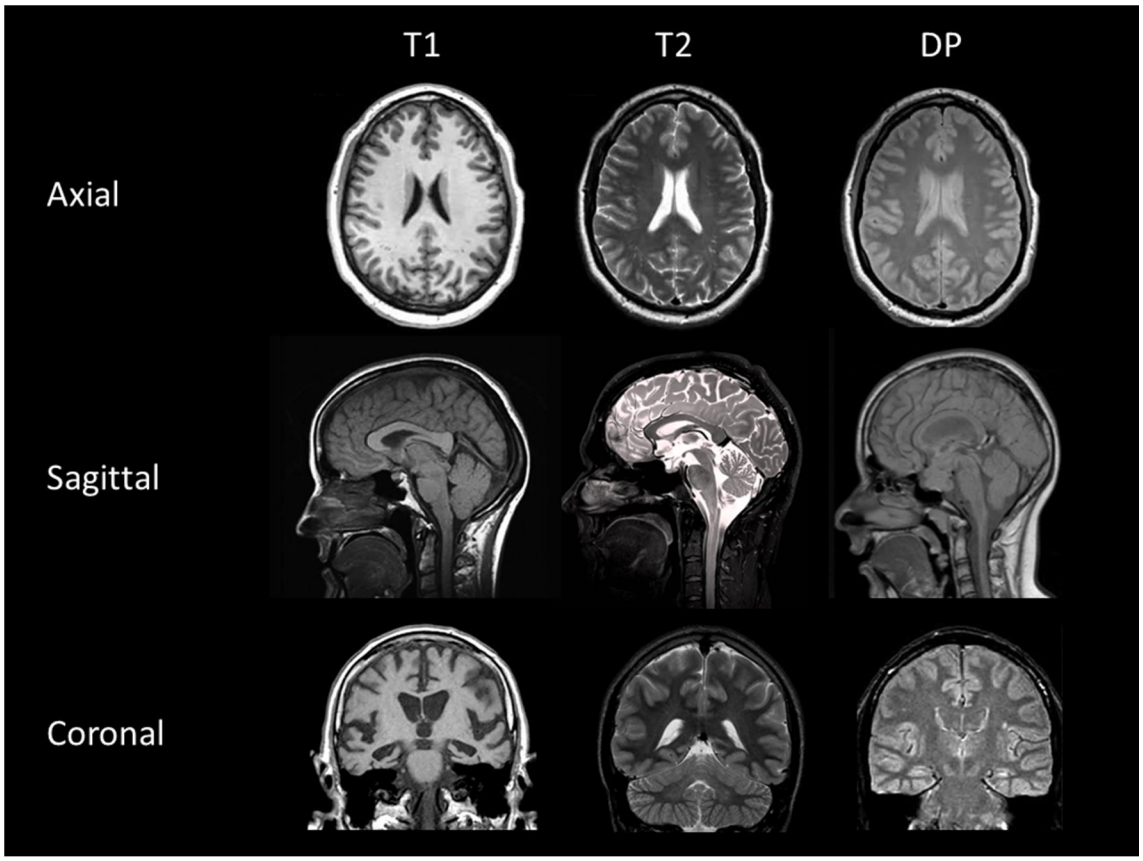

Figure 12: Brain MRI images. In this figure, the three different basic contrasts of brain MR images can be observed: T1-, T2-, and proton density-weighted images. The images are organized to show the difference in contrast between the three anatomical planes: axial, sagittal, and coronal.

Echo-planar imaging (EPI)

BOLD functional studies require the use of fast acquisition sequences to optimize temporal resolution and signal-to-noise ratio. Commonly, a special acquisition called EPI is used to obtain functional data. In other words, echo-planar images are usually produced when it is possible to fill all K-space lines during a single TR (Figure 13). Besides this feature, EPI possess a high T_2* sensitivity, and despite the fact that studies are time-consuming (increasing the possibility of certain movements from the subject under analysis), EPI sequences ally another advantage by possessing a low sensitivity to movement and flow artefacts. EPI sequences are optimal to obtain a good temporal resolution, but some disadvantages need to be highlighted as geometric distortion caused by the presence of differences in magnetic susceptibility between cerebral tissue interface and air. It is possible to fill the lines corresponding to K-space in a single TR. Consequently, spatial resolution decreases and a high number of data points are necessary to obtain sufficient statistical power concerning functional data related to BOLD effect (Faro, 2010).

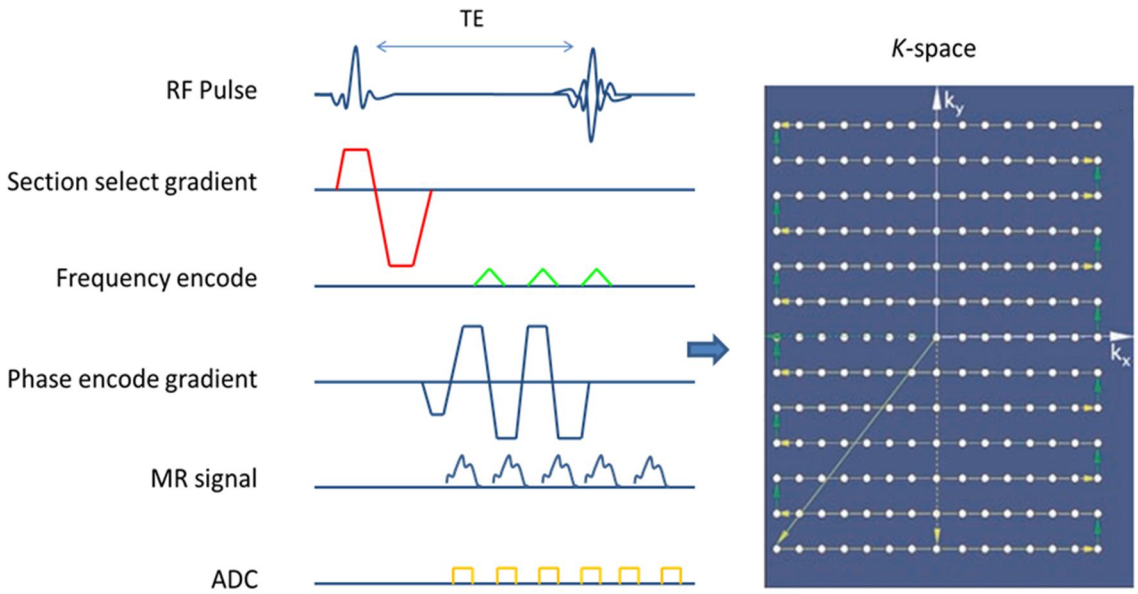

Figure 13: EPI pulse sequence diagram and *k*-space. In the beginning, a pair of gradients is applied in the phase- and frequency-encoding directions to reach the first sample point of the first k-space line. At that moment, an oscillatory gradient is applied along the frequency-encoding direction so that echoes are produced. (Adapted from Faro, 2010).

fMRI imaging

fMRI represents an important imaging modality to study brain function, based on the neuronal activity expressed by several brain regions. The fMRI physiological principle is related to neuronal population activity and its indirect relation with the hemodynamic response from surrounding blood vessels. This relevant and non-invasive imaging modality indirectly allows the study of cerebral brain activity taking into account its sensitivity to detect variations in blood oxygenation levels. Neuronal cells need a high glucose and O_2 uptake in order to perform their functions, and the main functional neuroimaging techniques (fMRI and PET) are based on these properties.

Astrocytes and blood–brain barrier

In most tissues, solutes can diffuse naturally between plasma (existent in the capillaries) and interstitial space; nevertheless, a restricted exchange is observed in the brain, allowing regulation of solutes that arrive to neuronal tissue through endothelial cells. This control is possible due to the blood–brain barrier, which can be described to be a structural relation formed by impermeable junctions of the endothelium, basal lamina, and axon terminal in astrocytes. Through this endothelial barrier, glucose and some amino acids are transported and biomolecules such as proteins and macromolecules are excluded (Magistretti, 2011 and Magistretti, 2016).

Astrocytes present a close physiological relation with neurons, feeding them and controlling the ionic equilibrium by removing the excess extracellular K^+ as well as synaptic neurotransmitters. Besides, they produce neurotrophic factors, such as the NGF (nerve growth factor).

From a bioenergetic point of view, and with special interest in neuronal activity measurement (imaging acquisition principle used in fMRI), neurons highly depend on aerobic respiration for ATP (and other energetic molecules) production. The resultant products from this glycolytic process, lactate and pyruvate, present in astrocytes are used during the Krebs Cycle (Tricarboxylic Acid Cycle) by the mitochondria. Once astrocytes surround blood capillaries and establish contact with neurons, glucose molecules are transported inside astrocytes and neurons. There, glucose is metabolized (or converted) in glycogen or degraded into lactate as consequence of neuronal activity. Glial cells are also responsible for interneuron signaling modulation, by releasing glutamate and ATP (Haines, 2006; Mackay, 2011), which are crucial in the glutamate–glutamine cycle.

BOLD effect and hemodynamic response

As previously described, the increase of neuronal activity in some regions is closely related with local blood flow increase in that area, defined by a hemodynamic response function. Due to its inherent bioenergetic necessity, the brain metabolizes a huge amount of glucose and uses oxygen carried by oxygenated hemoglobin or oxyhemoglobin present in the capillaries.

The presence of oxygen gives diamagnetic properties to hemoglobin molecule, but in the opposite scenario, when hemoglobin molecule does not carry oxygen—deoxyhemoglobin—it acquires paramagnetic properties. This property is responsible for the differences in magnetic susceptibility. Oxyhemoglobin has a negative magnetic susceptibility, whereas deoxyhemoglobin has a positive magnetic susceptibility. It turns out that when a substance presents a positive magnetic susceptibility, the magnetization vector has the same direction as the magnetic field strength. However, when a certain substance has negative susceptibility the magnetization intensity will present an opposite direction to the magnetic field strength (Ogowa et al, 1990 a, b and Ogowa et al., 1998).

Thus, an increase in oxygenated hemoglobin is observed when neuronal activity grows, which supports magnetic field homogeneity in the surrounding tissue (with minimal or inexistent magnetic field distortion) and is responsible for the increase in the T_2* signal (less transversal dephasing). Contrarily, an increase in deoxyhemoglobin leads to local field inhomogeneities due to the concentration of magnetic field lines. Consequently, the magnetic field B_0 is distorted, causing a decrease in the T_2* signal (large transversal dephasing). Based on this biophysical process, the BOLD functional measures can be obtained (Ogawa et al., 1990 a,b), representing the most used methods for functional neuroimaging studies with MRI.

BOLD effect in MRI is dependent on hemodynamic response

During fMRI acquisition, the hemodynamic response function (HRF) presents the differences in the temporal scale when compared with physiological process present in its genesis, which in this case is related to neuronal activity. This temporal limitation is, therefore, related to the fact that neurophysiological activity is being indirectly measured. In order to better understand this phenomenon, a graphical representation of the HRF process is presented and formed by three phases: 1) initial dip, 2) positive BOLD response, and 3) post-stimulus undershoot (Figure 14).

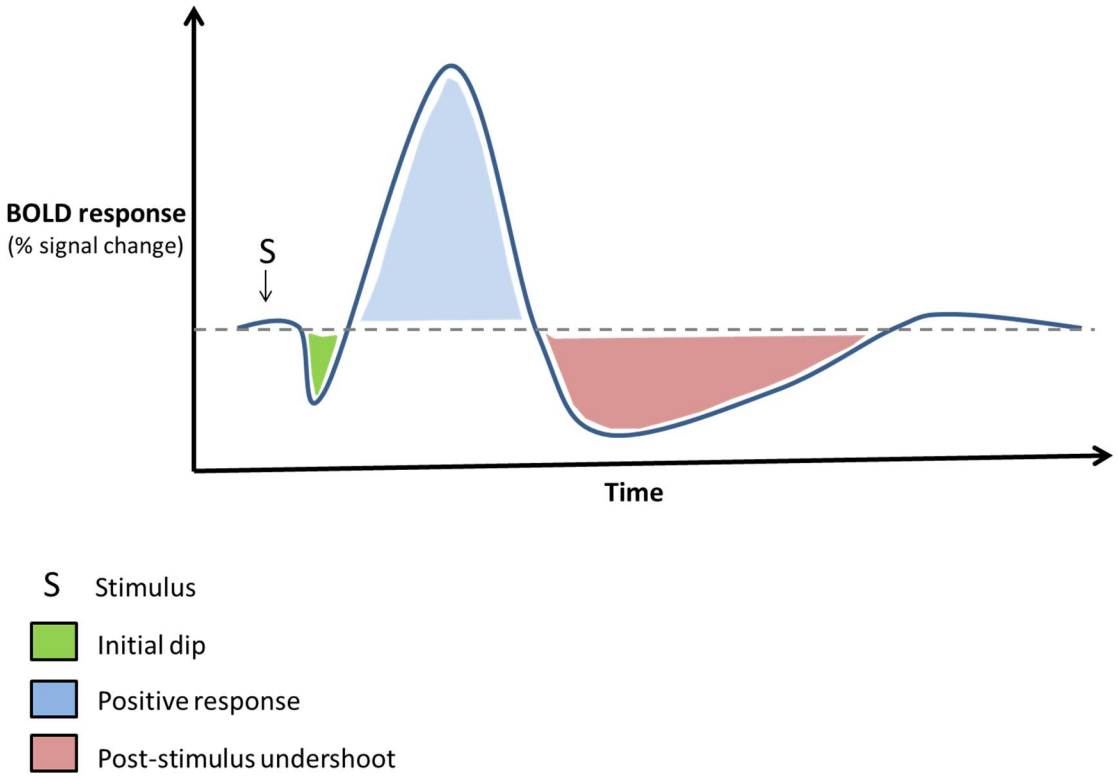

Figure 14: The hemodynamic BOLD response.

After the beginning of electric activity triggered by neurons, a small depression is observed in the BOLD signal intensity caused by high metabolic needs, which increases due to oxygen extraction. This necessity is responsible for the subsequent increase in blood flow, promoting a decrease in blood oxygen levels. In response to rCBF (regional cerebral blood flow), there is a regional increase in cerebral blood flow leading to re-oxygenation (hyper-oxygenation) and triggering a positive BOLD response (Goebel, 2007; Goense and Logothetis, 2008).

After cessation of the stimulus and before the BOLD signal returns to the pre-stimulus baseline level, an undershoot occurs, most probably due to an accumulation of deoxyhemoglobin in the vessels.

The detection of regional variation in blood oxygenation (BOLD effect principle) can be observed with fast MRI acquisition using EPI sequences. Performing a motor task leads to an increase in brain blood flow by 50% after brain activation; however, cell metabolic needs involved in this response are small, about 5% (Fox et al., 1998; Kuwabara et al.,, 1992; Fujita et al., 1999; Mintun et al., 2001) The increase in synaptic activity necessary to accomplish a motor task implies an increased energy uptake, in particular involving glucose and oxygen from the arteriole bed. The response to these

necessities activates a regional rise in blood flow and volume, which is called neurovascular coupling (whose mechanisms are still not completely enlightened). Hemodynamic response corresponds to this variation of blood flow, which is not immediate and reaches its maximum value about four to six seconds after beginning the task. At the same time, one observes a decrease in the oxygen extraction fraction (OEF). For a precise description of oxyhemoglobin and deoxyhemoglobin change over time, it is important to describe the initial moment in which a relative excess of deoxyhemoglobin (called initial dip) precedes the increased blood flow (Hu and Yacoub, 2012). Deoxyhemoglobin concentration reaches a maximum value two seconds after and then decreases, while oxyhemoglobin concentration continues to rise until its maximum (six seconds after the beginning the task). A very high increase in oxygen supply is observed in venules of the activated area. The decrease in deoxyhemoglobin concentration leads to a more local homogenous magnetic field (responsible for high phase coherence) and increased T_2*-weighted signal from about 2 to 5%. The hemodynamic response curve after reaching its maximum remains flat (plateau) for about eight to ten seconds and then the deoxyhemoglobin and oxyhemoglobin return to their baseline levels. This slow return is graphically represented by a decrease in their values due to slow cerebral blood flow and is also visualized by a decrease in values below baseline, right before progressively returning to metabolic equilibrium levels (Buxton, 2013; Logothetis, 2002; Logothetis and Wandall, 2004; Thomas et al., 2014; Figure 15).

In practice, the decrease in deoxyhemoglobin relative concentration relative to oxyhemoglobin, leads to a decrease in blood magnetic susceptibility involving the functional area and related with the motor task when compared to rest periods. It is possible to observe an increased MR signal in that area during a motor task, in this case, due to the pressure executed by both thumbs on a dedicated command.

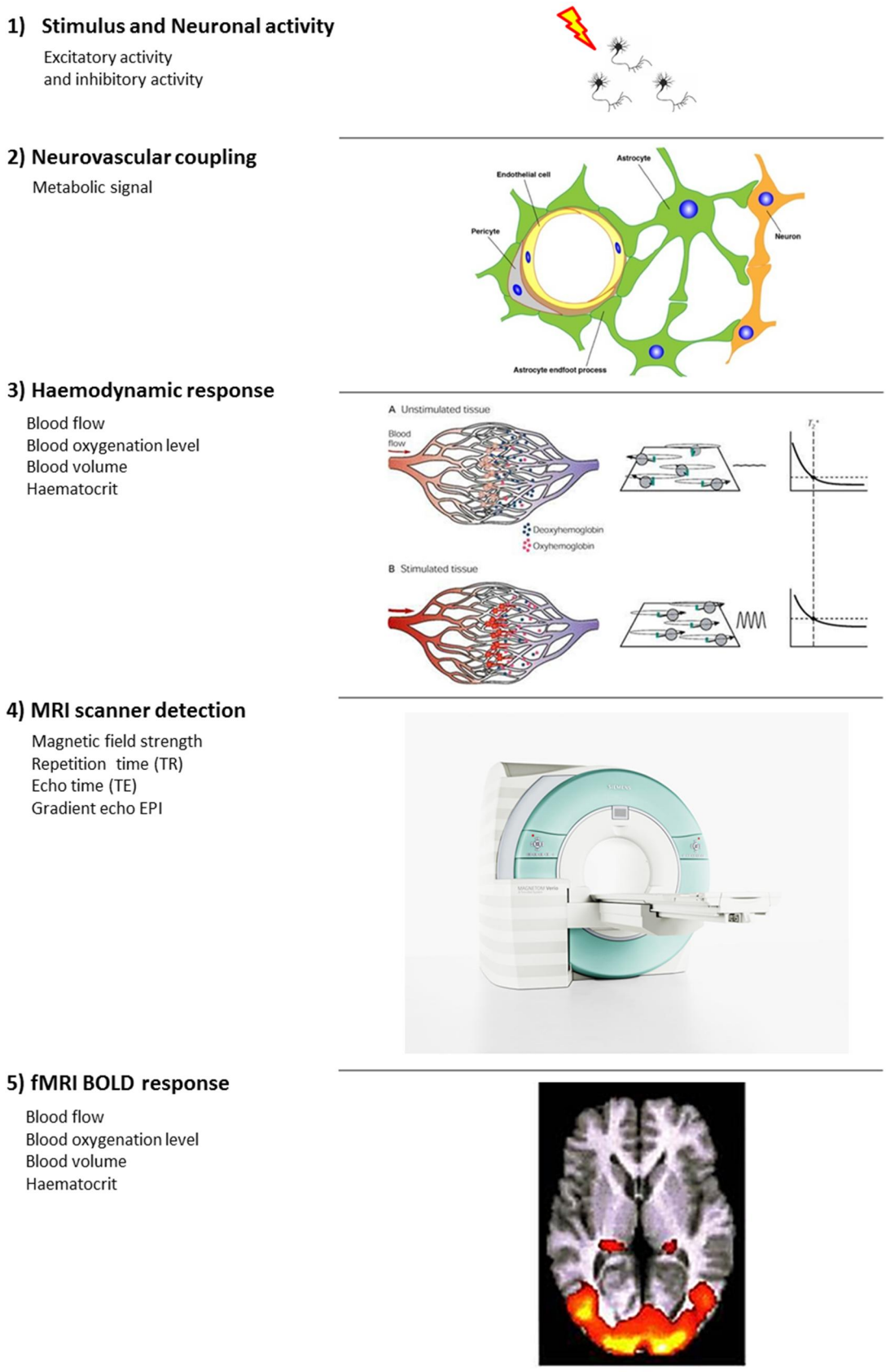

Figure 15: Schematic illustration of biophysical principles involving functional magnetic resonance imaging. Figure adapted from the book "Principles of Neuroscience" (Kandel et al., 2000) and reproduced from http://www.med.kobe-u.ac.jp.

fMRI data and block-design experiment

In order to study the activity of certain brain areas, stimulus presentation paradigms are developed for the subject submitted for an fMRI acquisition. Thus, this process is represented by alternating activation and rest period blocks. During the activation period, subjects perform a specific predetermined task integrated in the experimental design. Generally, this activation paradigm is defined in at least two blocks, in the simplest framework, which correspond to an activation and rest phase alternately executed and repeated through a certain number of times. Simultaneously, brain volumetric data are acquired by EPI-BOLD sequences periodically in function of the TR. Similar to this imaging, data are collected where each voxel is characterized by the temporal variation in the MR signal received as a function of the applied paradigm (Barker and Amaro, 2006; Linquist, 2008).

After performing a statistical analysis to study the significant differences between data collected during both different activation and rest period blocks, activation maps are generated and can be projected in morphological images acquired in 3D MP-RAGE (Magnetization Prepared - RApid Gradient Echo). This three-dimensional T_1-weighted MRI also allows morphometric analysis by using VBM.

Block-design

In this design, different kind of experimental conditions are divided in extended time intervals (or blocks). One block may repeat the process of interest (in this thesis, finger-tapping) during the experimental block (A) or have the subject in rest along a control block (B). Contrast analysis between both blocks can be used to evaluate the differences in signal exhibited by the two conditions. The increase in each block length leads to an increased response during the task, and, consequently, allows high statistical power. Nevertheless, it is also relevant to include several transitions and temporal gaps between conditions, since signal differences, because of low frequency, can be mistaken with different conditions related with the task. In fact, it is essential that the same mental process is evoked during each block. Thus, block lengths should not be too long, otherwise this assumption can be broken due to tiredness. The block-design use includes high statistical power related to activation and this kind of design is robust to uncertainties in the shape of HRF. This last feature is related to the fact that a predictable response depends on global activation caused by numerous individual

stimuli, which make it less sensitive to variations caused by individual stimulus responses (Figure 16). Contrarily, block designs give inaccurate information about specific events responsible for brain region activation and cannot be used to directly estimate significant HRF characteristics, such as the onset or width (Barker, 2006; Linquist, 2008; Logothetis and Wandall, 2004 and Logothetis, 2008).

Event-related designs

In this type of event, the stimulus consists of short discrete events (for example, short light flashes) with generally irregular timing (Figure 16 illustrates two conditions.) Event-related designs are interesting because of their flexibility, allowing the evaluation of key HRF characteristics (for example onset and width) which can be used as empiric assumptions about the time of activation in different conditions.

Event-related designs allow the analysis of different conditions effects, when there is an association of different events and there are important variations of several inter-stimulus interval between experiments. Another benefit is the possibility to avoid effects resulting from tiredness, tedium, and systematic patterns of thought not related with the task during long inter-trial intervals. An inherent disadvantage is the low power to detect activation comparative to block designs, however the ability to obtain images of more experiments per unit time can circumvent this power loss (Linquist, 2008).

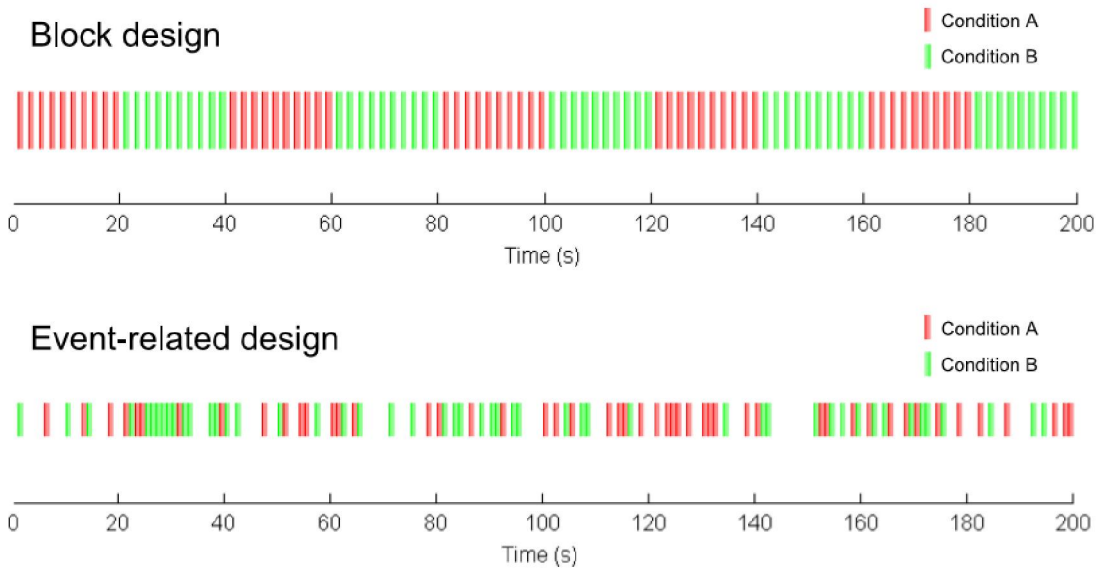

Figure 16: Main experimental design types. Schematic representation of the two experimental design classes most frequently used in fMRI studies, namely block designs and event-related design. In block designs, experimental conditions are

separated by long, equal time intervals or blocks. In an event-related design, stimuli are composed of short and discrete events, where timing and order can be random (reproduced from Linquist, 2008).

Preprocessing of brain fMRI data

The head movement correction is an important component to guarantee the quality of fMRI brain image analysis. Although, all patients with SCA3 and the healthy participants are instructed to remain still, sometimes, it is inevitable to observe changes induced by the magnetic field inhomogeneity caused by tissues (signal intensity loss and shape distortion) and the presence of motion artifacts and, in more severe cases, ring activation around the edges of the head can be observed due to the high variation of voxel intensity at the tissue borders. If each voxel represents one unique location in the brain, the motion becomes an important problem for the statistical analysis of the data.

In an fMRI, experiment functional information is acquired during the task paradigm, which is also known as a run. During a run, several acquisition of functional volume (3D) of the brain is realized at each TR and it is composed of spatial and temporal information, which gives it a 4D dimension. To perform the brain motion correction, one volume was identified to serve as a reference to align all volumes by rigid body transformation. This process can be described by translation along the x, y, and z-axes and rotation around these axes and is composed of six parameters, three translation and three rotation parameters, both in the x, y, and z directions. Iterative calculus was performed to estimate the behavior of these six parameters along a specific time-course, which defines how a specific volume should be translated and rotated to realize the best alignment with the reference volume. Usually, the options available to realize the preprocessing of 3D motion correction are: mean intensity adjustment, slice scan time correction, 3D motion correction, spatial smoothing, and temporal filtering.

fMRI statistical analysis

For extraction of reliable information from data obtained after a particular task associated to a long fMRI study, statistical analysis is fundamentally used to provide an understanding about which cerebral areas were activated by a specific stimulus. From several statistical methods used in fMRI data analysis, the generalized linear model (GLM) is the most used method currently. Identifying differences in response to a stimulus during an fMRI study between two groups is possible by using the GLM

(Figure 17). This method allows the calculation of parametric maps with statistically significant differences. This model is represented by:

$$y = X\beta + \varepsilon \qquad \text{[equation 5]}$$

where y is the variable response representing the signal measured, X is the predictor matrix parameter, β is the matrix of predictor weights, and ε is the error. In other words, GLM determines a prediction of variation associated to a dependent variable of several reference functions (linear combination). The dependent variable corresponds to the time voxel course in fMRI, and predictor variables correspond to the time course associated with modelled functional responses intended to be observed under several paradigm conditions in an fMRI study.

In terms of structure, specific predictors are defined as being the model or experimental plan matrix. From the convolution about a specific time course in blocks, it is possible to obtain the time course of a predictor. This convolution about block time course is related to a specific stimulation protocol and associated to a model hemodynamic response. GLM suits to study information independently for each voxel. Having a look at the mathematical expression, GLM joins to each predictor X and one specific coefficient β, allowing to determine the contribution of each one in the prediction about the time course associated to variable y. The existence of noise fluctuations led to error addition ε to correct the linear model in question (Goebel, 2007).

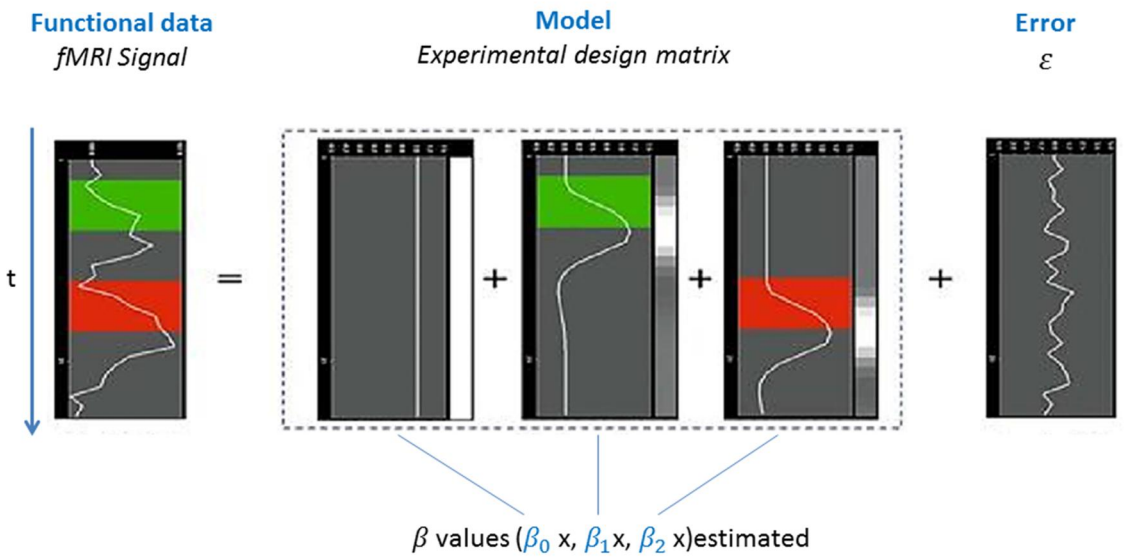

Figure 17: Schematic representation of the generalized linear model. On the left side, one observes the time course of the voxel and its experimental matrix or model, where the three predictors allow to estimate predicted values for fMRI associated with

"y" values. The linear model also considers the noise values, represented on the right side of this image (Goebel, 2007).

The comparison of β values is performed using t statistic that assigns a value to each voxel. Obtaining an activation and deactivation map is done by imposing a set of continuous voxels (also known as clusters) that constitutes the obtained three-dimensional statistical map. It is common in fMRI studies to use the association between a statistical correction for multiple comparisons, such as Bonferroni correction in order to define threshold (and avoiding inactive voxels inclusion), $p<0.05$ (corrected) are accepted for such studies.

Talairach transformation and functional data co-registration

Structural data obtained by cerebral MRI are processed to determine a common stereotaxic space of coordinates, known as Talairach. This transformation makes it possible to compare results from functional and morphometric analysis, as well as to correct small brain structural variations. This coordinated system is based on two anatomical reference points: anterior and posterior commissures. From these two points, the transformation process begins, where a coordinate plan is defined and then the underlying reference lines to the Talairach grid are calculated in function to maximum brain dimensions. These reference lines are expanded and contracted in the image for adjustment, and the coordinate system grid is taken into account. This is a vital step for brain data normalization into a space reference.

Voxel-based morphometry

One of the most usual methods in neuroimaging to identify functional or anatomical difference in the whole brain is VBM. This method is founded on a statistical approach to characterize the level of atrophy in brain pathology. The localization and identification of pattern atrophy was possible because VBM allows a comparison of the GM between distinct groups of subjects.

This method is more effective because the studies are focused on the entire brain, while the common analysis performed in the past were based on drawing regions of interest to calculate the respective anatomical volume on the acquired MRI brain imaging.

The VBM method uses T_1-weighted imaging data of MRI scan to perform statistical analysis across all voxels in the acquired image to localize pattern atrophy of grey matter that correspond to volume difference between groups. This difference in the

brain anatomy between controls and patients was calculated applying t-tests to all voxels in the image.

This neuroimaging method can be applied in different brain pathologies and neurodegenerative disorders like Alzheimer disease (Matsuda, 2013), movement disorders, schizophrenia, epilepsy, and multiple sclerosis. These studies improve our knowledge about structural and functional brain modification and possible physiological adaptations. For this purpose, some specific steps are necessary; all MRI data must be registered because brain anatomy varies across subjects and a spatial normalization permits that a specific brain coordinate correspond to the same brain region (same type of tissues) in the MRI scan of the remaining subjects. To improve this situation, a specific brain template is used to ensure that the same axis of coordinate was used to minimize potential errors due to the segmentation tissues and partial volume effect.

After spatial normalization, brain images are submitted to a process denominated as segmentation. A segmented image is the result of the computational separation of different tissues as GM, WM, and CSF. Usually, VBM studies are focused on GM, and due to the large number of studies performed until now, they provide important and plausible biological results. The segmented images are now smoothed and contrasted. Subsequently, a statistical model is applied (t-test) to identify the brain region with significant levels of atrophy, projected in a statistical parametric map. (Mechelli, 2005; Keller, 2008; Whitwell, 2009).

To ensure the best results, it is necessary to take several measures to not only minimize the sources of potential errors at the maximum, but also understand the basis of VBM analysis properly. In this chapter, we will present a description of the VBM fundamentals used in this academic research and identify the specific cares used in the different steps of these neuroimaging studies from the image acquisitions to the statistical parametric analysis.

Principles of VBM

During the last decades, an increasing number of neuroimaging methods and techniques have been developed to characterize differences *in vivo* as observed by MRI (Good, 2001). One of these methods is VBM.

The purpose of VBM method is to identify possible differences in the structure of brain tissues as GM, WM, and CSF, which was reached by applying five important steps (Friston and Ashburner, 2000), as outlined in Figure 18:

- Normalization and modulation: all MRI data are registered to the same standard space using a specific template.
- Segmentation: Brain imaging is segmented into GM, WM, and CSF.
- Smoothing: the new data are smoothed with a 3D gaussian kernel.
- Statistics: data from each group are averaged together and contrasted; a t-test is performed.
- Glass Brain: the final results are presented as a significance maps thresholded for multiple comparisons.

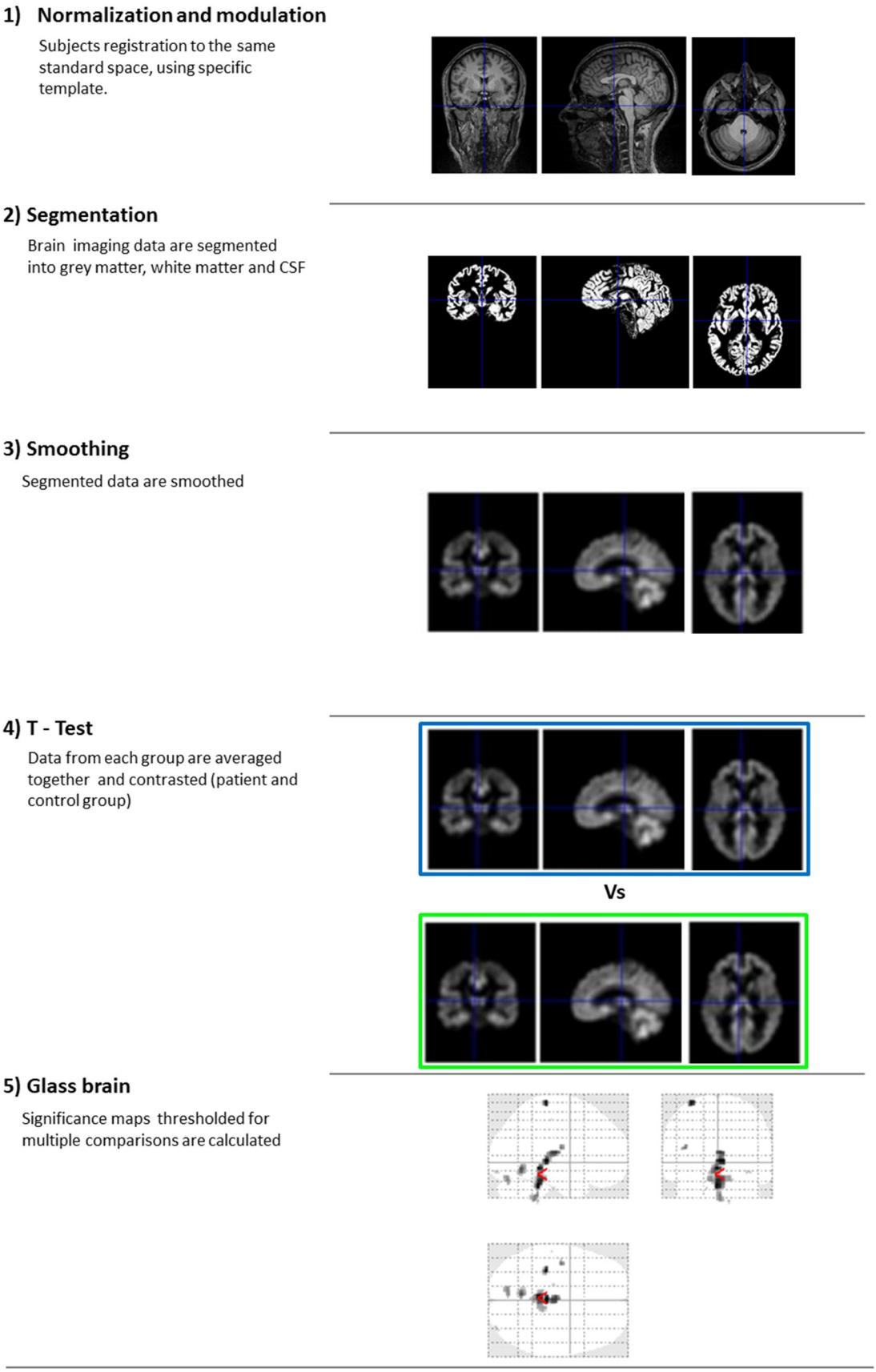

Figure 18: Summary of the different steps in VBM.

Spatial normalization

In this first step, all MRI image are registered in the same stereotactic space using a specific template. The application of this standardization is fundamental to perform an adequate statistical comparison between groups of MR images based in voxels.

For the implementation of spatial normalization, an estimation of the 12-parameter affine transformation was required (degrees of freedom), the objective of this step is to correctly orient all anatomical reference points in MRI images to the template space. Due to the complexity in identifying the subtlest differences, a second step that involves a modulation by a linear combination of smooth spatial basis functions is needed. If the standard normalization is successfully performed, the future results can be presented in a standard system, i.e., the Talairach coordinate system used in brain imaging studies (MNI to Talairach).

Modulation

The process of spatial normalization uses a shape transformation denominated modulation to correct volume change that occurs in this step. During a nonlinear registration, the information about the absolute volume of brain tissue is not preserved and difference can be observed in relative concentrations after statistical analysis, so modulation is necessary to correct these phenomena.

Segmentation

After the spatial normalization and modulation correction, brain images are segmented into three different tissues, GM, WM, and CSF. During this process non-brain elements are also obtained. Usually this is achieved with the combination of *a priori* established probability maps obtained in accordance with the model used in this study (data of healthy subjects), also defined to "Bayesian priors", the foundation of a mixture model cluster analysis responsible for the voxel intensity distributions for a specific tissue considered. After this, a binarization process ("0" and "1") can be applied to the recent tissue images obtained. The classification method produces tissue images with *a posteriori* probability map.

The process of brain segmentation is very sensitive to intensity variation due to the magnetic field imperfections, i.e., inhomogeneities in the RF coils. To correct these inhomogeneities, before the segmentation procedures, a bias correction step was applied. In this study, neuroimaging data was analyzed using SPM8

(http://www.fil.ion.ucl.ac.uk/spm/), where registration and modulation occur simultaneously, for this reason this process is also known as unified segmentation.

Smoothing

After the last steps described above (registration, modulation and segmentation), all imaging data are submitted to a smoothing process. The smoothing step is necessary to obtain a good normal distribution of data applying the central limit theorem, a fundamental aspect to perform valid parametric statistical tests. This blurring of anatomical detail differences establishes a better spatial overlap that decreases morphological error based on registration errors.

Finally, smoothing enhances the difference and turns the statistical analysis more sensitive due to the gain from higher signal to noise ratio (SNR), but this condition is observed if the Kernel used has a full width at half maximum (FWHM) similar to the size of the regional tissue difference being measured.

This smoothing process is possible through convolution with a 3D isotropic Gaussian Kernel characterized by the spatial resolution defined by its FWHM in mm, with a direct accordance with the standard deviation (symbol):

$$FWHM = \sqrt{8ln\,2}.\sigma \qquad \text{[equation 6]}$$

Statistical analysis

The purpose of the statistical analysis of MRI images after the smoothed and segmented steps is to identify morphological differences in the brain (GM) between the group of controls (healthy subjects) and the patients, along the time of this experiment. This analysis uses a parametric statistic based on GLM and the theory of Gaussian random field, producing a series of results on statistical significance represented by the *P*-value.

In the VBM studies, the purpose of the statistical analysis is to identify significant differences (of brain anatomy), represented by t-values corresponding to *P*-values between the brain images of patient and control groups. For this purpose, a t-test is performed, and the values are given by:

$$T = \frac{(\overline{X}_1 - \overline{X}_2) - (\mu_1 - \mu_2)}{s} \qquad \text{[Equation 7]}$$

where,

- $\overline{X}_1 - \overline{X}_2$ is a variable related to the difference in means between the contrasting groups
- $\mu_1 - \mu_2$ is the null hypothesis H_0(usually zero)
- S is a variable related to the standard deviation of both populations.

Two situations can happen in this type of statistical analysis of brain images. In the first case, a false positive or a type I error occurs, where a non-existent anatomical difference is detected. The second case represents the inverse situation, a false negative or a type II error occurs; where a true difference in brain anatomy remains undetected.

A statistical test has one or two tails (unilateral or bilateral), depending on how the null hypothesis is formulated. Considering that null hypothesis is bilateral, the difference between means can either be positive or negative, in this case, the hypothesis is defined as $\mu_1 - \mu_2 \neq 0$. However, in a unilateral hypothesis the possible values are $\mu_1 < \mu_2$ or $\mu_1 < \mu_2$, in this situation t-values have one sign when significant.

The first representation of the statistical values is the "glass-brain" (Figure 19A), a transparent map used to show the significant voxels (clusters); however, a three-dimensional (3D) surface render of brain (Figure 19B) can be employed to improve the topological experience transforming the analysis of results to be more intuitive (Good, 2001; Friston, 1995; Friston and Ashburner, 2000), see Figure 19.

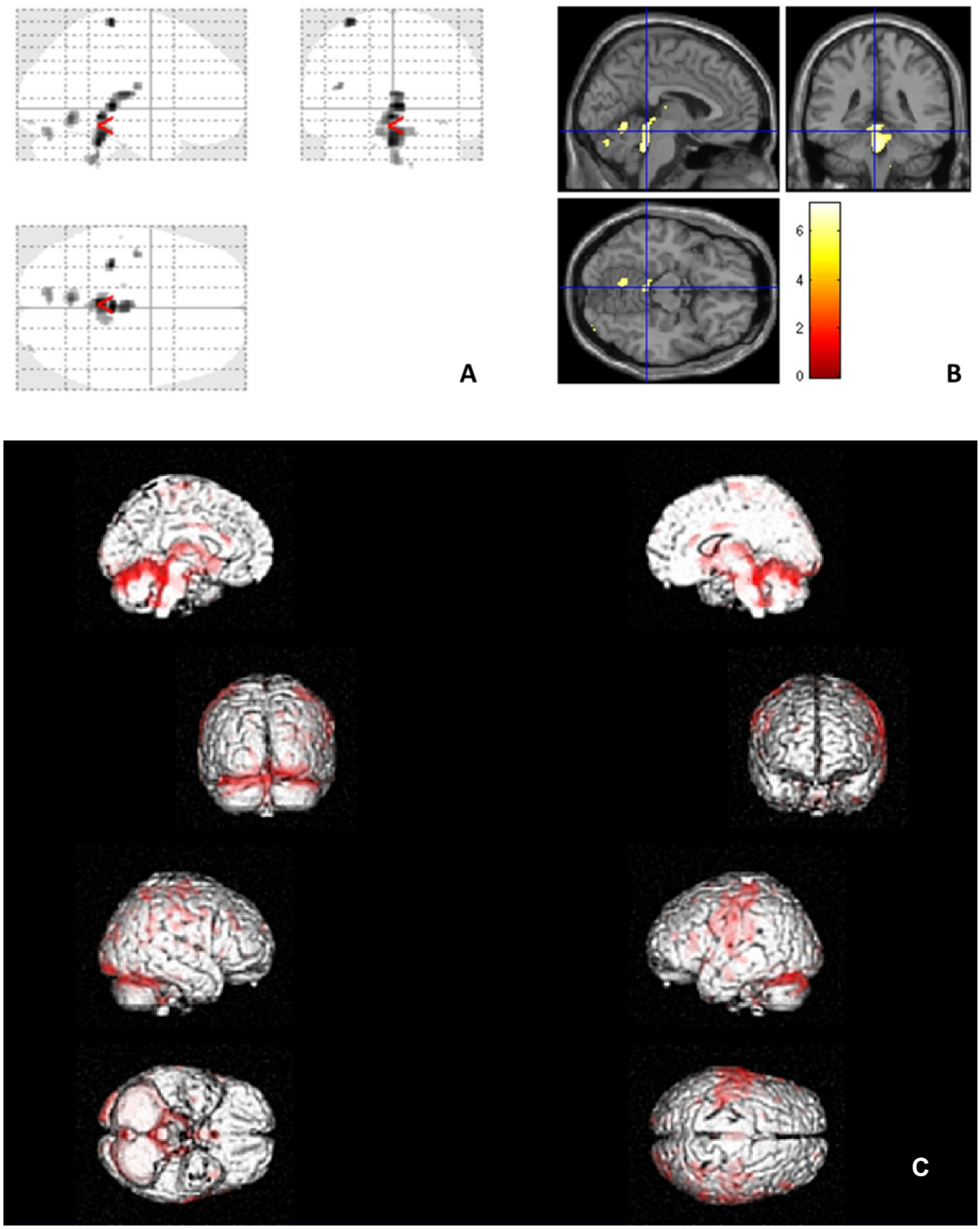

Figure 19: Visualization of statistical values. A) glass brain representation. B) Projection of the detected pattern of atrophy on a single brain T_1 template and the scale bar for *T*-values. C) Representation of a 3D rendering with the different region of neuronal atrophy in red color.

Brainvoyager QX

One of the most commonly used softwares to analyze anatomical and fMRI data is Brainvoyager QX (version 2.4, BrainInnovation, Maastricht, The Netherlands), which also allows the study of Diffusion Tensor Imaging (DTI), Transcranial magnetic brain stimulation (TMS), electroencephalography (EEG), and magnetoencephalography (MEG) data. This software has been programmed in C++ language, providing a useful interface to improve important advanced features in neuroimaging research practices, including 2D and 3D analysis. The first task performed with Brainvoyager is based on a series of pre-processing steps as motion correction, high-pass filtering, and slice scan time correction. The basic statistical analysis performed in Brainvoyager follows a transversal tool used in different neuroimaging methods, the GLM. However, other statistic tests like random effect ANCOVA and multi-voxel pattern analyses can also be applied. The false discovery rate (FDR) is used to define a dynamic statistical threshold, which is relevant for correcting multiple comparisons. To study the brain activation volume, the volume of interest (VOI) can be used to identify the difference in multi-subject analysis.

References

Ashburner, J and Friston, KJ. Unified segmentation. NeuroImage 26 (2005) 839-851.

Barker, GJ. Amaro JR, E. Study design in fMRI: Basic principles. 2006. Brain and Cognition.

Buxton, RB. The physics of functional magnetic resonance imaging (fMRI). Rep Prog Phys. 2013 September ; 76(9): 096601.

Currie S, Hoggard N, Craven IJ, Hadjivassiliou M, Wilkinson ID. Understanding MRI: basic MR physics for physicians. Postgrad Med J. 2013;89(1050):209-223. doi:10.1136/postgradmedj-2012-131342

Faro, S. H. & Mohamed, F. B. BOLD fMRI: A Guide to Functional Imaging for Neuroscientists. (Springer, 2010).

Faustino, R. Efeito Da Exposição A Ressonância Magnética De Elevado Campo No Desenvolvimento Do Organismo: *Caenorhabditis elegans*. Tese de Mestrado,2009, ULHT Lisboa.

Fox, P. T., Raichle, M. E., Mintun, M. A. & Dence, C. Nonoxidative glucose consumption during focal physiologic neural activity. Science 241, (1988).

Friston, K. J. et al. Statistical parametric maps in functional imaging: A general linear approach. Hum. Brain Mapp. 2, (1995).

Friston, KJ. Ashburner J. Voxel-Based Morphometry – The methods. NeuroImage 11. 805-821 (2000).

Fujita H, Kuwabara H, Reutens DC, Gjedde A. Oxygen consumption of cerebral cortex fails to increase during continued vibrotactile stimulation. J Cereb Blood Flow Metab. 19:266-271.(1999).

Good, CD. Johnsrude, IS. Ashburner, J. Henson, RNA. Friston, KJ. Frackowiak. A Voxel-Based Morphometric study of ageuing in 465 normal adult human brains. NeuroImage 14, 21-36 (2001).

Goebel, R. in Clinical Functional MRI 9-51 (2007).

HAINES, Duane E. Neurociencia Fundamental: Para aplicações básicas e clinicas. 3ª Edição, Churchill Livingstone. ISBN-10: 85-352-1977-3.

Hu, X. & Yacoub, E. The story of the initial dip in fMRI. Neuroimage 62, 1103-1108 (2012).

Geraldes C., Gil V., Ressonância Magnética Nuclear: Fundamentos, Métodos e Aplicações, 2002, Fundação Calouste Gulbenkian. ISBN:9789723109696

Goebel R. Localization of brain activity using functional magnetic resonance imaging. In: Clinical Functional MRI Presurgical Functional Neuroimaging 2007.

Goense JB, Logothetis NK. Neurophysiology of the BOLD fMRI signal in awake monkeys. Curr Biol. 18:9 (2008) 631-640.

Keller, SS. Roberts, N. Voxel-based morphometry of temporal lobe epilepsy: An introduction and review of the literature. Epilepsia, 49(5):741-757, 2008.

Kuwabara H., Ohta S., Brust P., Meyer E., Gjedde A. Density of perfused capillaries in living human brain during functional activation. Prog. Brain Res. 91, 209-215.(1992).

Mackay, William. Neurofisiologia Sem Lágrimas, 2011, Fundação Calouste Gulbenkian. ISBN: 9789723111620

Magistretti, P. J. Neuron-glia metabolic coupling and plasticity. Exp. Physiol. 96, (2011).

Magistretti, P. J. Imaging brain aerobic glycolysis as a marker of synaptic plasticity. Proc Natl Acad Sci U S A. 2016 Jun 28; 113(26): 7015-7016.

Matsuda, H. Voxel-based Morphometry of Brain MRI in Normal Aging and Alzheimer's Disease. Aging and Disease. Volume 4, Number 1; 29-37, 2013.

Mechelli, A. Price, CJ. Friston, KJ. Ashburner, J. Voxel-Based Morphometry of the human brain: Methods and Applications. Current Medical Imaging Reviews, 2005, 1, 00-00.

Mintun M., Lundstrom B., Snyder A., Vlassenko A., Shulman G., Raichle M.. Blood flow and oxygen delivery to human brain during functional activity: Theoretical modeling and experimental data. Proceedings of the National Academy of Sciences, 98 (12) 6859-6864; (2001). DOI: 10.1073/pnas.111164398.

Ogawa S, Lee TM, Kay AR, Tank DW. Brain magnetic resonance imaging with contrast dependent on blood oxygenation. Proc Natl Acad Sci U S A. 87:24 (1990) 9868-9872.

Ogawa, S., Lee, T.-M., Nayak, A. S. & Glynn, P. Oxygenation-sensitive contrast in magnetic resonance image of rodent brain at high magnetic fields. Magn. Reson. Med. 14, 68-78 (1990).

Ogawa, S., Menon, R. S., Kim, S.-G. & Ugurbil, K. On the characteristics of functional magnetic resonance imaging of the brain. Annu. Rev. Biophys. Biomol. Struct. 27, (1998).

Lindquist, MA. The statistical Analysis of fMRI Data. Statistical Science, 2008, Vol.23, Nº. 4, 439-464.

Logothetis, N. K. The neural basis of the blood-oxygen-level-dependent functional magnetic resonance imaging signal. Philos. Trans. R. Soc. Lond. B. Biol. Sci. 357, 1003-1037 (2002).

Logothetis, N. K. & Wandell, B. A. Interpreting the BOLD signal. Annu. Rev. Physiol. 66, 735-769 (2004).

Logothetis, N. K. What we can do and what we cannot do with fMRI. Nature 453, (2008).

Rinck PA Magnetic resonance in medicine: the basic textbook of the European Magnetic Resonance Forum, 5th Edition. Oxford ; Boston: Blackwell Scientific Publications. 2003.

Thomas M. Talavage, Javier Gonzalez-Castillo, and Sophie K. Scott. Auditory Neuroimaging with fMRI and PET. Hear Res. 2014 January ; 307: 4-15.

Tavitian B, Leroy-Willig A, Ntziachristos V. Textbook of in vivo Imaging in Vertebrates, 2007 John Wiley & Sons, Ltd. Print ISBN: 9780470015285.

Schild, H. H. MRI made easy. (Schering AG, 1990).

Shinotoh H, Thiessen B, Snow BJ, Hashimoto S, MacLeod P, Silveira I, Rouleau GA, Schulzer M, Calne DB. Fluorodopa and raclopride PET analysis of patients with Machado-Joseph disease. Neurology. 1997 Oct;49(4):1133-6.

Soong, BW. Liu, RS. Positron emission tomography in asymptomatic gene carriers of Machado-Joseph disease, J Neurol Neurosurg Psychiatry 1998;64:499-504.

Whitwell, JL. Voxel-Based Morphometry: An automated Tecnique for assessing structural changes in the brain. The Journal of Neuroscience, August 5, 2009. 29(31): 9661-9664.

Chapter 3

Research methodology

Ethics statement

The research work is part of the project "From molecules to man: novel diagnostic imaging tools in neurological and psychiatric disorders. An integrated multidisciplinary project". The supervisor of this thesis and principal investigator was Professor Miguel Castelo Branco, MD, PhD. The procedures performed in this study have been reviewed and approved by the ethics committee of the Faculty of Medicine of the University of Coimbra. Informed consent was obtained from all patients and volunteers. This study is in accordance with the principles of the Declaration of Helsinki.

Recruitment and selection of participants

Participants were recruited in neurogenetics consultation of neurology B service in the Hospitals of the University of Coimbra. The criteria for this study were:

Inclusion criteria

- Age > 18 years
- SCA3 diagnosis according to the genetic test performed at IBMC (Instituto de Biologia Molecular e Celular), University of Porto.

Exclusion criteria

- Head trauma
- Neurosurgery
- Radiosurgery and radiotherapy
- Brain chemotherapy
- Neurooncological disease
- Epilepsy
- Psychiatric disorders
- Visual deficits
- Motor deficit
- Claustrophobia

The control group (families) is totally composed by healthy volunteers with no history of psychiatric or neurological disorders. The patient group comprised subject with positive genetic test for SCA3/MJD and patients with familial genetic diagnosis for SCA3 at early clinical stage. The patients were enrolled in neurogenetics consultation where they are monitored.

Research timeline

The aim of this thesis is to develop a biomarker based on advanced neuroimaging techniques that allows us to define patterns and detect early cerebellar lesions without ruling out the identification of other lesions at the cerebral level. A longitudinal study conducted on Machado–Joseph Disease (symptomatic and asymptomatic patients with positive genetic diagnosis) and control group (individuals without disease) to potentially generalizes, in the future, other pathologies that affect the cerebellum (Bettencourt, 2011; Table 2).

Acquisition of imaging data

Neuroimaging assessment has a high potential to detect the occurrence of early morphological and functional changes even before the onset of the initial symptoms (Globas, 2008). Structural data acquisitions were performed using a 3 T research scanner (Magnetom TIM Trio, Siemens, Erlangen, Germany) phased array 12 channel birdcage head coil), using a 3D anatomical MP-RAGE (magnetization prepared rapid gradient echo) scan using a standard T_1 gradient echo pulse sequence.

The fMRI motor paradigm involved bilateral, audio-paced thumb movements. Participants were instructed to use their thumbs simultaneously to press alternately on one button of two hand-held MRI compatible response boxes. Movements were paced by audio-tones at temporal frequencies of 1, 3, and 5 Hz, delivered by MRI-compatible headphones.

All experiments were performed between 2012 and 2016 (Table 2). Patients and control participants visited our institute at least once to perform structural MRI acquisition and acquire functional MRI data, which included an audio-cued thumb tapping task at different frequencies (1, 3, and 5 Hz). Patients and control participants were informed about the objective of the experiment and they were positioned to train and test the command and other devices necessary to perform the motor tasks.

Chronogram and milestones – PhD project

New morphometrics and functional biomarkers of cerebellum by magnetic resonance: validation in Machado–Joseph disease

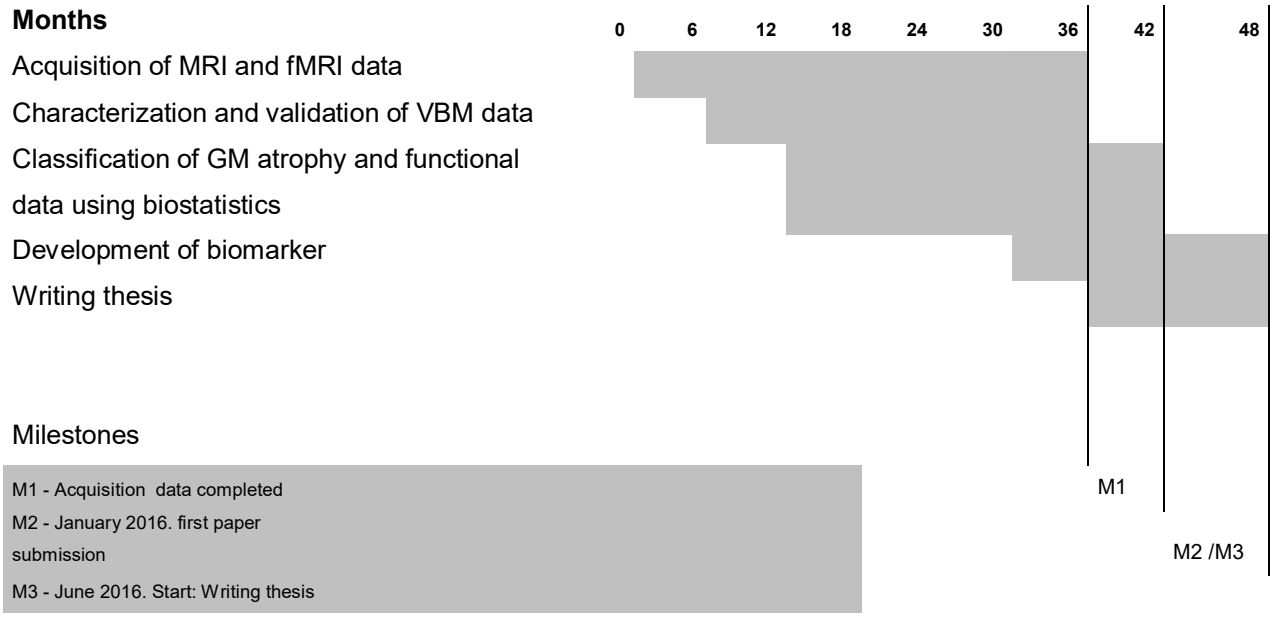

Table 2: Research timeline (chronogram and milestones). In this chronogram we observe that the study was initiated in September 2012 and finished in July 2015. The grey area of the horizontal bars presented in this figure show the duration of each task analyzed and presented in this thesis. The first item corresponds to the acquisition of functional and structural data presented in this thesis. The last MRI and fMRI acquisitions were performed in July 2015. M1, M2, and M3 are the milestones defined for this research.

Characterization and validation of data

The VBM method allows the whole brain to be analyzed without the bias of regional hypotheses, generating a statistical map of structural changes associated with the pathology under analysis (Goel, 2011). This method allows analysis of the volume of structures element by element (voxel a voxel), in order to create a statistical map of significant differences against a group of healthy patients (controls). It consists of the application of a series of spatial processing steps made through the freely available SPM software (http://www.fil.ion.ucl.ac.uk/spm/) causing the normalization of images to a standardized space, segmentation in different tissue classes (GM focus) and Gaussian smoothing, followed by the calculation, voxel a voxel, using a statistical model that reveals differences or correlations associated with the volume of each coordinate (Lukas, 2006: Eichler, 2011; Abreu, 2012; Friston and Ashburner, 2000).

Classification of GM atrophy and functional data using biostatistics

It should be noted that if it is possible to extract a small number of classifying characteristics, it will be feasible to perform biostatistical studies to obtain ROC curves to test the performance of the classification system and define the best threshold value, which optimizes diagnostic decision-making. The comparison between methods, namely between the imaging analysis of the structural images of the brain and cerebellum performed by a neuroradiologist (clinical gold standard) and the morphometric and functional analysis methods (functional morphometry) performed were performed to assess specificity and sensitivity of our biomarker.

Rationale of biomarker development

The development of imaging biomarkers (Baldarçara, 2015) for the early detection of cerebellar lesions may represent an important step in monitoring available treatments, in addition to disease progression monitoring. The development of novel biomarkers is important for clinical trial design. The implementation of our biomarker may also help understand the mechanisms of the disease in this region.

Genetic characterization of participants with SCA3

The participants with SCA3/MJD underwent genetic analysis. The biological samples (blood) needed for analysis followed the recommendations of the document "instruções para a colheita e envio de amostras" ("Instruction for harvesting and shipment of samples") from the Preventive and Predictive Genetic Center of the Molecular and Cell Biology Institute (IBMC) at the University of Porto.

The SCA3 genetic analysis is based on investigation of the expansion of CAG motif repetition located within exon 10 of ATXN3 gene using Polymerase Chain Reaction (PCR) and triplet repeat primed PCR (TP-PCR) methods.

Neurological assessment

Before the visit to ICNAS, all patients were studied by a neurologist by a neurogenetics examination to evaluate the scale for assessment and rating of ataxia (SARA) and the scale description neurological examination score for the assessment of spinocerebellar ataxia (NESSCA) evaluation. SARA is a neurological scale based on a semiquantitative assessment of cerebellar ataxia on an impairment level. SARA is a structured eight-item performance-based scale, on which a total score of 0 and 40 represent no ataxia and severe ataxia, respectively. The score is based on patient performance of stance, speech

disturbance, gait, sitting, nose–finger test, finger chase, fast alternating hand movements, and heel–shin slide.

NESSCA is also a semiquantitative scale based on 40-point, covering 18 different items, with high values indicating poor performance. In NESSCA scale, 14 items correspond to a neurological examination and four items rely on patient information.

Neuroradiological assessment

The patients and control group were subjected to an anatomical evaluation, performed by a neuroradiologist, from images acquired on T_1-weighted sequence, denominated MP-RAGE. The fMRI data consisted of a sequence of 148 gradient-echo EPI. Images were acquired at the National Brain Imaging Network facilities of the Institute for Nuclear Science Applied to Health (ICNAS) of the University of Coimbra.

References

Abreu A, França MC Jr, Yasuda CL, Campos BA, Lopes-Cendes I, Cendes F. Neocortical atrophy in Machado-Joseph disease: a longitudinal neuroimaging study. J Neuroimaging 2012;22:285-291.

Ashburner, J and Friston, KJ. Unified segmentation. NeuroImage 26 (2005) 839-851.

Baldarçara, L et al., Consensus Paper: Radiological Biomarkers of Cerebellar Diseases. Cerebellum . 2015 April ; 14(2): 175-196. doi:10.1007/s12311-014-0610-3.

Bettencourt and Lima Orphanet Journal of Rare Diseases 2011, 6:35.

Eichler L, Bellenberg B, Hahn HK, Köster O, Schöls L, Lukas C. Quantitative assessment of brain stem and cerebellar atrophy in spinocerebellar ataxia types 3 and 6: impact on clinical status. AJNR Am J Neuroradiol 2011;32:890-897.

Globas, ST du Montcel, L Baliko et al. Early symptoms in spinocerebellar ataxia type 1, 2, 3, and 6 Mov Disord, 23 (2008), pp. 2232-2238.

Gaurav Goel, Pramod Kumar Pal, Shivashankar Ravishankar, Ganesan Venkatasubramanian, Peruvumba N. Jayakumar, Nithin Krishna, Meera Purushottam, Jitender Saini, Mohammed Faruq, Mitali Mukherji, Sanjeev Jain. Gray matter volume deficits in spinocerebellar ataxia: An optimized voxel based morphometric study. Parkinsonism & Related Disorders - August 2011 (Vol. 17, Issue 7, Pages 521-527.

Lukas C, Schöls L, Bellenberg B, et al. Dissociation of gray and white matter reduction in spinocerebellar ataxia type 3 and 6: a voxel-based morphometry study. Neurosci Lett. 2006;408:230-235.

CHAPTER 4

Results: parametric fMRI of paced motor responses uncovers novel whole-brain imaging biomarkers in spinocerebellar ataxia type 3

Introduction

Spinocerebellar ataxia type (SCA3, Machado-Joseph Disease, MJD) is an inherited neurodegenerative disease (Woods et al., 1971; Rosenberg et al., 1976; Coutinho et al., 1978) caused by an expanded (CAG)n motif repeat mutation in the coding region of the ATXN3 gene, in chromosome 14q32.1 (Maciel et al., 2001; Martins et al., 2006). Normal alleles have usually a number of repeats ranging between 12-41, whereas in disease carriers this range is between 53-86 repeats (Bettencourt et al., 2010; Kawaguchi et al., 1994; Schöls et al., 2004). CAG repeat length exhibits an inverse correlation with age at onset (Klockgether et al., 1996; Abe et al., 1998) and determines 46% of onset variability in addition to non-repeat related factors (Globas et al., 2008; Swami et al., 2009) such as paternal transmission and intragenic CGG/GGG polymorphism (Martins et al., 2006; Takiyama et al., 1995).

Recent studies emphasized the importance of early symptom detection (Globas et al., 2008; Jardim et al., 2001; Garrard et al., 2008). Neuropathology and immunohistochemistry suggest involvement of a broad array of cortical and subcortical regions (Coutinho et al., 1982; Rüb et al., 2002; Kumada et al., 2000; Rüb et al., 2004; Lukas et al., 2008; Yamada et al., 2001), which is consistent with neuroradiological studies (Murata et al., 1998; Horimoto et al., 2008).

So far, neuroimaging studies in SCA3 focused on structural or resting state changes (Hashimoto et al., 2011). Functional MRI (fMRI) is based on the blood oxygenation level dependent (BOLD) signal changes (Ogawa et al., 1990), and still infrequently used in clinical practice (Pillai et al., 2010). It has focused only on the cerebellum as the region of interest in hereditary ataxias (Stefanescu et al., 2015). One way to overcome the limitations of fMRI in clinical research is to use level-dependent parametric designs coupled with whole-brain analysis. For example a quantitative change in motor performance patterns, such as frequency of movement alternation, can potentially be related with neuroactivation in clinically impaired groups. Parametric manipulation of the task demands maybe critical in identifying regions specifically performing the physiologically relevant computations (Müller et al., 2003).

Here we searched for the neural correlates of deficits in rhythmic motor planning of sequences of increasing frequency associated with SCA3. We set to assess motor coordination of hand movements (assessing the ability to accurately perform discrete voluntary movements at increasing temporal frequency levels) and to parametrically

correlate behaviour with neuroactivation (for the feasibility of this approach see Wurster et al., 2015; Riecker et al., 2003). The aim was to identify fingerprints of altered functional patterns in relatively early stages of the disease, of potential use to monitor disease progression. We found evidence for performance level-dependent neuroactivation in SCA3 suggesting early functional reorganization in a broad array of cortical areas contrasting with low cerebellar activation. Such fMRI activation patterns can be used in reliable statistical classification of disease states.

Materials and methods

Participants

Eighteen SCA3 patients (mean age, 40.57±12.44 years; 9 female) and twenty-one control participants (32.24±9.68; 11 female) were included. All patients, with genetically proven disease (through investigation of the expansion of CAG motif repetition located within exon 10 of ATXN3 gene), were recruited from the Neurogenetics Unit of the University Hospital of Coimbra (CHUC - Coimbra, Portugal). Control participants had no personal or family history of neurological or psychiatric diseases. All participants were right handed. The Helsinki Declaration guidelines were followed throughout the study. The Ethics Committee of the Faculty of Medicine of the University of Coimbra approved the study.

At the day of the MRI examination neurological examination was performed in all participants. We defined as the onset of the disease when a permanent neurological disturbance appeared (mean ± SD = 32.94±11.44 years). Disease severity and clinical ataxia scores were assessed also on the same day based on the Scale for the Assessment and Rating of Ataxia (SARA. Schmitz-Hübsch et al., 2006) and the Neurological Examination Score for the assessment of Spinocerebellar Ataxia type 3 (NESSCA. Kieling et al., 2008). Clinical and demographic data are summarized in Table 3.

Table 3. Demographic characteristics and of the study participants

	SCA3	Controls	P-value[a]
N	18	21	
Age (years)	40.57 (12.44)	32.24 (9.68)	n.s.
Gender (M/F)	9/9	10/11	n.s.
Disease onset (at age)	32.94 (11.44)		
NESSCA score	12.33 (6.67)		
SARA score	13.88 (10.78)		
CAG expanded	69.31 (17.02)		
CAG normal	21.17 (4.04)		

NESSCA = Neurological Examination Score for Spinocerebellar Ataxia. SARA = Scale for the Assessment and Rating of Ataxia. Data presented as mean (± standard deviation).

Data presented as mean (± standard deviation). [a] Between-group differences were tested using Mann-Whitney test for age and χ^2-test for gender distribution.

MRI scanning

Structural and functional MRI acquisitions were performed at the National Brain Imaging Network facilities, on a 3T research scanner (Magnetom TIM Trio, Siemens, phased array 12-channel birdcage head coil).

Structural MRI data acquisition

We acquired a 3D anatomical MPRAGE (magnetization-prepared rapid gradient echo) scan using a standard T_1w gradient echo pulse sequence (TR = 2530 ms; TE = 3.42 ms; TI = 1100 ms; flip angle 7°; 176 slices with voxel size 1mm x 1mm x 1mm; FOV 256 mm).

***Voxel-Based** Morphometry analysis*

Data were pre-processed using SPM8 software (Wellcome Trust Centre for Neuroimaging, UCL, London, UK, http://www.fil.ion.ucl.ac.uk/spm). T1-weighted native images were aligned onto the axis of the anterior and posterior commissures, automatically corrected for inhomogeneity of the magnetic field and segmented into

grey matter (GM), white matter (WM), and cerebrospinal fluid (Ashburner and Friston, 2000, 2005). We used the standard MNI template for spatial normalization and segmentation followed by a non-linear only ‘‘modulation’’ step (Ashburner, 2009, 2000; Buckner et al., 2004). We smoothed the modulated normalized GM volume images with 3-dimensional 8-mm full-width at half-maximum (FWHM) isotropic Gaussian kernels. We then applied a GLM at each voxel to investigate between-group differences in regional volumes, including age as a covariate. Volumetric differences (SCA3 vs. controls) was compared using voxel-wise two-sample t-tests corrected for multiple comparisons (voxel level P-value < 0.05 corrected employing the family wise error (FWE) rate) (Hayasaka et al., 2004; Worsley et al., 1999).

Behavioral task and fMRI data acquisition

The fMRI motor paradigm involved bilateral, audio-paced thumb movements. Participants were instructed to use their thumbs simultaneously to press alternately on one button of two hand-held MRI compatible response-boxes (Cedrus Lumina LP-400, LU400 PAIR, Cedrus Corporation, San Pedro, CA - USA). Movements were paced by audio-tones at temporal frequencies of 1, 3 and 5 Hz, delivered by MRI compatible headphones (Avotec, Inc., FL - USA). Twelve blocks of stimulation, four per frequency, were interleaved with thirteen rest periods. Block duration was 28 seconds (stimulation) and 14 seconds (rest). The total scanning time was 518 seconds. Stimulation was synchronized to the acquisition using a PC running the Psychophysics Toolbox (PTB3) (Brainard, 1997; Pelli, 1997), on Matlab R2008a (MathWorks, Natick, MA-USA).

fMRI series consisted of a sequence of 148 gradient-echo echo-planar imaging (EPI) scans (TR 3500 ms; TE = 30 ms; flip angle 90°; 36 interleaved slices with voxel size 3mm x 3mm x 3mm; FOV 256 mm) in a parametric block-design stimulation paradigm, covering the whole brain, including cerebellum, brainstem and motor cortex.

A control cohort of 9 participants (4 patients/5 controls) performed the finger-tapping task at a temporal frequency of 1, 2 and 3 Hz. Neurobehavioral findings were similar but we do not present these data to focus on the larger group of 27 participants, (13 SCA3 patients and 14 controls), from which we can generalize the results to the population, using random effects analysis.

Behavioural performance analysis

During fMRI the time of button presses were recorded and stored. Average thumb movement frequency over block type for each prescribed audio-pacing frequency of 1, 3 and 5 Hz was calculated as number of thumbs, as well as the standard deviation, as a measure of movement synchronization. Between-group motor performance was compared using the Mann-Whitney test at P-value (2-tailed) = 0.05.

fMRI data preprocessing and analysis

Preprocessing/statistical analyses of functional imaging data were performed using BrainVoyager QX 2.4 (BrainInnovation, Maastricht, The Netherlands). Scans were preprocessed by applying slice scan time correction, linear trend removal, temporal high-pass filtering (2 cycles/run) and head-motion correction. We did not apply temporal smoothing to the data but we did apply spatial smoothing, to ensure normality of the data and satisfy the requirements of the random field theory. Scans were excluded when >2 voxel motion was detected. Functional data were co-registered to each subject's structural T1 image in stereotaxic Talairach space. For statistical comparisons, we performed an RFX (random effects) GLM (general linear model) analysis which allows modelling explicitly both within-subjects and between-subjects variance components in order to generalize findings to the population level (Penny et al., 2003). Predictors corresponding to the 3 prescribed stimulation frequencies, were used to estimate condition effects (beta values) separately for each subject (first-level), allowing to localize areas exhibiting parametric modulation, i.e. in which BOLD signal changes differentially with movement frequency. Then the estimated first-level mean effects per subject enter the second level as the new dependent variable and serve as input to the group analysis. Analysis at the second-level explicitly models the variability of estimated effects across subjects, to generalize to the population (Beckmann et al., 2003). Statistical maps were corrected for multiple comparisons using the false-discovery rate (FDR) correction at P-value < 0.01 with cluster extent threshold (Fig 21 and 22). We further examined the mean activation values and the average BOLD fMRI response time courses for each stimulation condition in selected regions of interest (Fig 21-22).

Regions-Of-Interest based analysis of BOLD response

To perform independent parametric ROI analyses, these were first selected based on the contrast (1 Hz + 3 Hz + 5 Hz > baseline), in all pooled participants. All subsequent hypotheses about parametric effects and between-group differences are explicitly independent from this contrast. Furthermore, we circumscribed the analysis to regions that were identified in a large voxel-wise, coordinate-based meta-analysis on 685 sets of activation foci in Talairach space gathered from 38 published studies employing finger-tapping tasks (Witt et al., 2008). Clusters of concordance in audio paced finger-tapping tasks were identified within the primary sensorimotor cortices, supplementary motor area, premotor cortex, basal ganglia, and anterior cerebellum. After investigating BOLD response individually in each ROI we merged ROIs in three groups, cerebellum, sub-cortical and cortical regions, as the response profiles were similar across ROIs within these categories.

For each grouped ROI we performed a ROI-GLM analysis in each group to extract the mean activation values in response to each frequency and we also investigated the full BOLD response time course during finger-tapping periods.

Parametric analysis

In each grouped-ROI we performed a mixed ANOVA with one between-subjects factor (group) and one within-subjects factor (frequency) with repeated measures to compare the mean difference between groups. In case there was an interaction effect between the two factors we further tested the simple main effect and pairwise comparison of frequencies in each group, to quantitatively assess the parametric modulation effect of the finger-tapping task in brain activation.

ROC analysis

We hypothesized that the parametric effect would be lost in SCA3 group, and the BOLD response would not follow the parametric variation of frequencies in SCA3 patients as in controls. Thus, we set to investigate the potential role of this parametric modulation of BOLD response as a biomarker of early SCA3 and computed receiver operating characteristic (ROC) curves for the discrimination of SCA3 patients and control participants based on the activation difference between every two prescribed frequencies: (3 Hz – 1 Hz), (5 Hz – 3 Hz) and (5 Hz – 1 Hz).

Cerebellar activation

The individual activation volume in the cerebellum was obtained from statistical maps of activation with the previously described contrast, thresholded at P-value < 0.01 using Bonferroni correction for multiple comparisons.

Results

VBM analysis of whole-brain group differences

VBM results are presented in Fig 20 and Table 4. We found clusters of significant grey matter reduction in SCA3 patients in multiple brain regions over the thalamus, cerebellum, parietal lobe (postcentral gyrus) and insula.

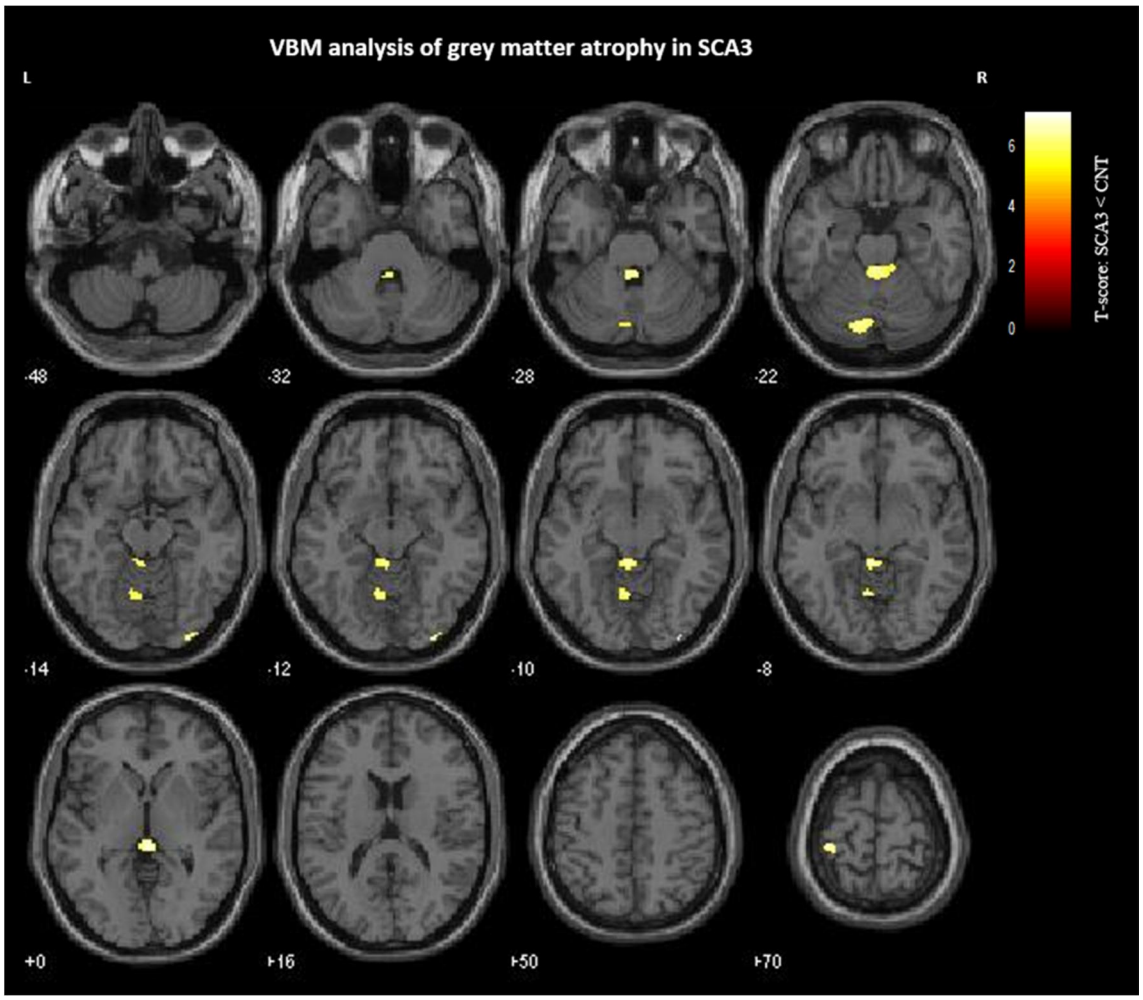

Figure 20: Significant grey matter reduction in SCA3 patients. Results are presented at a voxel-level P-value < 0.05 corrected for family-wise error rate and non-stationary smoothness. The spatial extent threshold was set at 10 voxels. Voxels showing significant grey matter relative volume between-groups reduction are overlaid on canonical single T1-weighted MRI subject template.

Table 4. Significant grey matter regions with neurodegenerative atrophy in SCA3 patients

Region	Cluster size	X	Y	Z	P-value[a]	Z_{max}
Right Brainstem, midbrain	157	1.0	-32.0	1.0	<0.001	5.59
Left Cerebrum, Parietal Lobe, Postcentral Gyrus	43	-33.0	-37.0	61.0	<0.001	5.56
Left Cerebellum, Anterior Lobe, Culmen	259	-2.0	-38.0	-7.0	<0.001	5.43
Left Cerebellum, Anterior Lobe		-2.0	-37.0	-25.0	<0.001	5.37
Left Cerebellum, Posterior Lobe, Pyramis	113	-10.0	-72.0	-24.0	<0.001	5.36
Right Cerebrum, Occipital Lobe, Inferior Occipital Gyrus	20	30.0	-87.0	-14.0	0.003	5.28
Left Cerebellum, Posterior Lobe, Declive	53	-7.0	-59.0	-12.0	<0.001	5.23
Left Brainstem, Medulla	27	-1.0	-39.0	-37.0	0.002	4.96
Right Cerebellum, Anterior Lobe, Culmen	259	8.0	-32.0	-17.0	<0.001	4.80

Coordinates are presented in Talairach space. [a] P-value was corrected at threshold 0.05 with family-wise error (FWE) rate and cluster size was controlled with a cluster extent threshold of 10 voxels.

Behavioral performance: evidence for increasingly degraded performance as a function of frequency

All subjects were able to rhythmically perform thumb movements but with different performance patterns, which are presented in Table 5.

Table 5. Behavioural performance and cerebellar activation volume

	SCA3	Controls	P-value[a]
Nr of thumbs at 1 Hz	1.04 (0.04)	1.01 (0.02)	0.029
Nr of thumbs at 3 Hz	2.58 (0.46)	2.98 (0.13)	0.010
Nr of thumbs at 5 Hz	2.90 (0.78)	4.02 (0.59)	< 0.001
CAV (mm^3)	4571.69 (1823.38)	7102.57 (1782.73)	0.120

CAV = cerebellar activation volume. SD = standard deviation.

Data presented as mean (± standard deviation). [a] Between-group differences were tested using t-test or Mann-Whitney test when data were not normally distributed (both were corrected with Bonferroni method).

Motor performance of patient and control groups were significantly different. They showed similar of number of thumb movements (NT) at low frequencies ($NT_{1Hz, SCA3}$ = 1.04; $NT_{1Hz, CNT}$ = 1.01) but diverged at higher frequencies ($NT_{3Hz, SCA3}$ = 2.58; $NT_{3Hz, CNT}$ = 2.98; $NT_{5Hz, SCA3}$ = 2.90; $NT_{5Hz, CNT}$ = 4.02). Between-group differences in motor performance were significant at all prescribed frequencies (P-value < 0.05, all comparisons, corrected for multiple comparisons; see Table 5). The increased deviation of the motor performance from the prescribed frequencies in the SCA3 group demonstrates diminished movement synchronization. One-sample t-test of frequency *deviation* was applied for each frequency in both groups. We found significant deviations with effect size increasing gradually, being higher for the mean number of thumbs at 5 Hz than for the mean number of thumbs at 1 Hz and 3 Hz in SCA3 patients and controls. These results support the notion that this parametric design of the motor task enabled the identification of 5 Hz as the performance limiting condition for both groups, ensuring asymptotic neuroactivation, which was correlated with movement frequency.

Correlation between genetics, behaviour, age and cerebellar activation

In the SCA3 group age had a positive strong correlation with the number of thumb alternations at 1 Hz (r = 0.648, P-value < 0.001) and an inverse significant correlation with the motor response at 3 Hz (r = -0.494, P-value = 0.009) and 5 Hz (r = -0.542, P-value = 0.003). This pattern was not found in the control group. The overall correlation analysis is presented in Table 6 and 7.

Table 6. Correlation between genetics, behaviour, age and cerebellar activation

	Age		Cerebellar activation volume	
	Rho	P-value	Rho	P-value
NESSCA	0.018	0.969	-0.284	0.536
SARA	0.047	0.879	-0.168	0.583
Disease onset	0.849	<0.001	-0.159	0.603
CAG expanded	-0.387	0.304	0.203	0.601
CAG normal	-0.263	0.528	0.313	0.450
Nr of thumbs at 1 Hz	0.648	<0.001	-0.203	0.311
Nr of thumbs at 3 Hz	-0.494	0.009	0.288	0.145
Nr of thumbs at 5 Hz	-0.542	0.003	0.382	0.049

NESSCA = Neurological Examination Score for Spinocerebellar Ataxia. SARA = Scale for the Assessment and Rating of Ataxia. CAV = cerebellar activation volume.
Correlation was tested using Spearman's rank-order correlation in all participants.

Correlation between clinical ratings and genetics

Strong correlations were found between the two clinical scales: scale for the assessment and rating of ataxia (SARA) and the neurological examination score (NESSCA) (r = 0.953, P-value < 0.05). However, no significant correlations were found between the expanded CAG repeats length and neurological examination measures.

The age of disease onset presents a strong inverse correlation with expanded CAG repeat length (r = -0.88, P-value = 0.02), confirming previous evidence that CAG length influences disease onset (Abe et al., 1998; Globas et al., 2008). The disease duration showed a strong correlation with SARA (r = 0.872, P-value = 0.024).

Sensitivity analysis of behavioral performance

We performed sensitivity and specificity analysis of behavioral performance of patients versus controls. We computed the ROC (receiver operating characteristic) curve for the number of button presses at each prescribed frequency. The area under the curve (AUC) was found to be highly significantly different from the null hypothesis of no between-group discrimination for 1 Hz (AUC = 0.812, SEM = 0.082, P-value = 0.002), 3 Hz (AUC = 0.898, SEM = 0.065, P-value < 0.001) and 5 Hz (AUC = 0.910, SEM = 0.067, P-value < 0.001). Additionally, we investigated for each group the sensitivity of task performance to discriminate the prescribed frequency. We found the motor task performance to be significantly discriminative of all the prescribed frequencies in controls. In SCA3, interestingly, the within group discrimination between 3 Hz and 5 Hz was the only not significant ROC curve, suggesting loss of the parametric effect.

Cerebellar activation volumes

Quantitative analysis of cerebellar activation volume (CAV) is shown in Table 5. The average CAV in SCA3 patients and controls were (mean ± SD) 4571.69 ± 1823.38 and 7102.57 ± 1782.73 mm^3, respectively. In Fig 21A representative examples of CAVs are shown for a patient and a healthy participant. However the difference in CAV was not significantly different between-groups (Mann-Whitney test, P-value = 0.120, Table 5). We did not find significant correlations between CAV and age or clinical variables at P-value < 0.05 (see Table 7). Concerning correlations between CAV and motor performance in the SCA3 and control groups a significant correlation was found specifically for the demanding rate of 5 Hz (see Table 7).

Table 7. Correlation between genetics, behaviour, age and cerebellar activation

	Disease duration		Cerebellar activation volume	
	Rho	P-value	Rho	P-value
NESSCA	0.709	0.074	-0.284	0.536
SARA	0.460	0.114	-0.168	0.583
Disease duration	---	---	-0.314	0.297
CAG expanded	-0.076	0.847	0.203	0.601
CAG normal	0.192	0.649	0.313	0.450
CAV	-0.314	0.297	---	---
Nr of presses at 1 Hz	0.313	0.297	-0.203	0.311
Nr of presses at 3 Hz	0.071	0.817	0.288	0.145
Nr of presses at 5 Hz	0.137	0.655	0.382*	0.049

NESSCA = Neurological Examination Score for Spinocerebellar Ataxia; SARA = Scale for the Assessment and Rating of Ataxia; CAG expanded/normal = repeat length of the respective alleles; CAV = cerebellar activation volume. Correlation was tested using Spearman's rank-order correlation in all participants. * Correlation is significant at the 0.05 level (2-tailed).

Whole-brain fMRI analysis and ROI definition

The fMRI statistical map extracted from the whole brain RFX-GLM analysis yielded significantly activated voxels in expected regions, according to the meta-analysis of finger-tapping studies (Witt, et al., 2008). We observed significant bilateral activation in the postcentral gyrus (Brodmann area 3, BA3; TAL coordinates [L: -36 -33 50; R: 37 -29 54]), primary motor cortex in the precentral gyrus (M1/BA4; TAL [L: -37 -21 50; R:

38 -22 55]), supplementary motor area (SMA/BA6; TAL [1 -18 59]) and inferior right parietal cortex in the area of the supramarginal gyrus (BA40; TAL [L: -41 -38 50; R: 39 -38 52]). We also observed significant activation of three sub-cortical regions: Putamen (TAL [L: -23 -8 9; R: 24 0 9]), Globus Pallidus (TAL [L: -22 -9 5: R: 25 -14 2]) and Thalamus (TAL [L: -23 -20 8; R: 14 -21 8]), as well as in the cerebellum (TAL [L: -13 -55 -18; R: 13 -56 -18]).

As mean BOLD amplitude and response profiles were similar in regions in the cortex or in sub-cortical regions, we grouped BA3, BA4, BA6 and BA40 in a ROI called *cortical*. The same was observed in Putamen, Globus Pallidus and Thalamus, thus we grouped them in a ROI called *sub-cortical*. We investigated the within-group effect of parametric modulations across the three grouped-ROIs: cerebellum, sub-cortical and cortical brain regions. A mixed ANOVA with one between-subjects factor (group) and one within-subjects factor (frequencies) was conducted to examine the effect of the disease and prescribed frequency on BOLD response in the cerebellum, sub-cortical regions and cortical regions. Moreover we tested between-group effect of this parametric finger-tapping task in brain activation and further assessed the potential role of a parametric finger-tapping task as a biomarker for the discrimination of early SCA3 patients.

Importantly, we tested the effect of age in the functional MRI results by running an ANCOVA model including *Age* as a covariate. This covariate did not show any significant contribution to the analyzed BOLD responses.

BOLD response in the cerebellum

Parametric analysis

Fig 21B shows the whole brain statistical RFX map, depicting significant activation in the anterior cerebellum of the whole group of participants, at a low and corrected P-value. After drawing an ROI for the cerebellum as described earlier, we plotted the mean BOLD amplitude in each group separately at each prescribed frequency (Fig 21C). We can clearly see that control participants are able to increase the response in the cerebellum with increasing frequencies, while SCA3 participants are only able to do it for the intermediate increase in cue frequency (from 1 Hz to 3 Hz) but not for the most demanding frequency (5 Hz), indeed decreasing BOLD signal amplitude in this condition. The same effect is observable in the full time course of BOLD response, plotted in Fig 21D and E for patients and controls, respectively. While SCA3 patients

show close (and often mixed) profiles across frequencies, control participants exhibit a clearly separated response profile for each frequency with distinct amplitudes across time.

Quantitatively, the repeated measures ANOVA analysis showed a statistically significant interaction between the effects of group and tapping frequency on the BOLD response in the cerebellum, $F(2, 50) = 9.029$, P-value < 0.001 (Table 8). Computation of simple main effects revealed that frequency variation in SCA3 patients had a much smaller effect size ($\eta p^2 = 0.320$) and was significant only for the pairwise comparison of 1 Hz vs 3 Hz. In controls a larger effect size was found ($\eta p^2 = 0.638$) and all pairwise comparisons of frequencies were significant (see Table 8). This results suggest loss of the parametric effect in SCA3 in the cerebellum.

Table 8. Regions-Of-Interest analysis of BOLD response with repeated measures ANOVA

ROI-based Repeated measures ANOVA			Stats	**Cerebellum**	**Sub-cortical**	**Cortical**
Interaction Frequency x Group			df (error)	2 (50)	2 (158)	2 (212)
			F	9.029	3.043	21.148
			P-value	< 0.001	0.050	< 0.001
			ηp²	0.265	0.037	0.166
SCA3	Simple main effect		df (error)	1.386 (16.630)	1.570 (59.649)	2 (102)
			F	5.635	2.868	31.989
			P-value	0.021	0.077	< 0.001
			ηp²	0.320	0.070	0.385
	Pairwise comparisons	1Hz - 3Hz	P-values	< 0.001	0.005	< 0.001
		3Hz - 5Hz		1.000	1.000	0.086
		1Hz - 5Hz		0.198	0.586	< 0.001
CNT	Simple main effect		df (error)	2 (26)	1.559 (63.902)	1.634 (89.884)
			F	22.892	9.888	52.595
			P-value	< 0.001	0.012	< 0.001
			ηp²	0.638	0.115	0.489
	Pairwise comparisons	1Hz - 3Hz	P-values	0.071	1.000	< 0.001
		3Hz - 5Hz		0.003	0.051	< 0.001
		1Hz - 5Hz		< 0.001	0.045	< 0.001

ηp² = partial eta squared, a measure of the estimated effect size; df = degrees of freedom.

Pairwise comparisons are post hoc tests corrected with Bonferroni correction for multiple comparisons.

When sphericity was not verified we used a Greenhouse-Geisser correction.

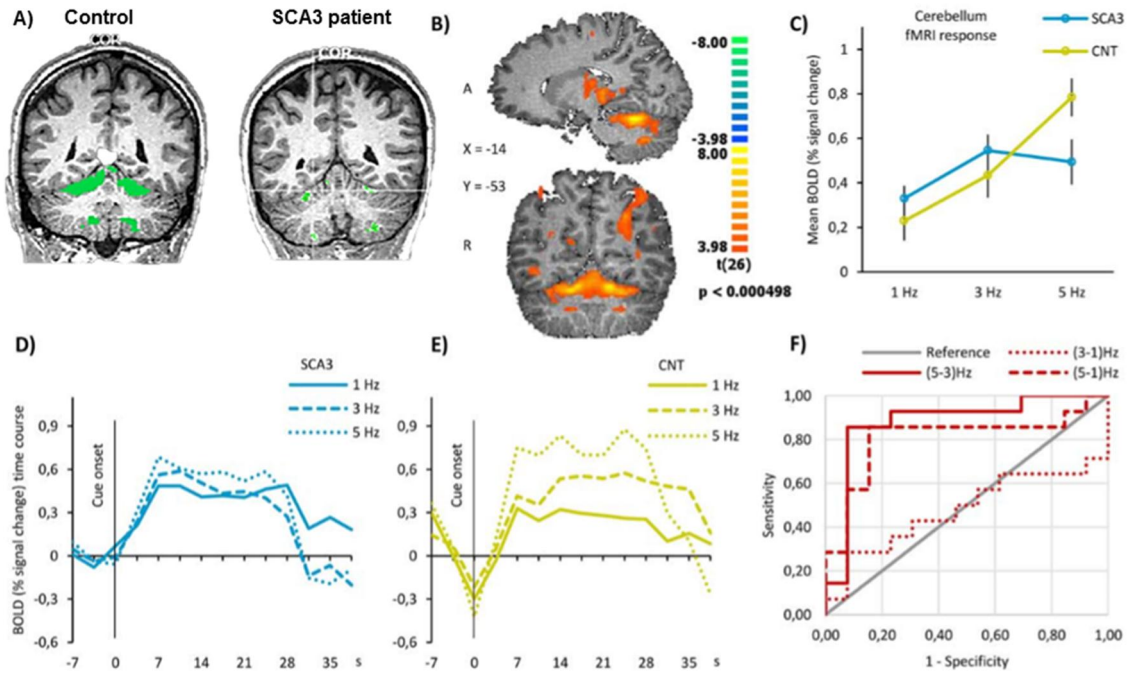

Figure 21: Functional MRI results in the cerebellum. A) Actual cerebellar activation volumes in a 33 year-old control participant, on the left, and a 21 year-old SCA3 patient, with mild disease (SARA score = 6 and NESSCA score = 14), on the right. In these individual cases cerebellar activation volumes were 18869 mm3 and 1766 mm3, respectively. No visible gross atrophy is visible. B) Hand movement-related RFX statistical parametric map in sagittal and coronal sections showing significant neuronal activation in cerebellum. Data are shown at a height threshold of P-value < 0.05 corrected for false discovery rate. C) Mean BOLD activity within cerebellum during finger-tapping task in SCA3 patients and controls. Data are presented as mean % signal change ± standard error of the mean. D) and E) Averaged time course of the BOLD response in the cerebellum, respectively in SCA3 patients and controls, during finger-tapping task at the three prescribed frequencies. F) Sensitivity analysis of BOLD signal in cerebellum. We computed the ROC curve for the difference in BOLD signal between every two frequencies of finger-tapping. ROC curve analysis shows up to 85.7% and specificity 84.6% (AUC = 0.879) to discriminate SCA3 patients from controls.

ROC analysis

The discrimination between early SCA3 patients and healthy controls based on BOLD response to the parametric finger-tapping task is presented in Fig 21F.

We can observe that the difference in BOLD response at frequencies (5 Hz – 3 Hz) and (5 Hz – 1 Hz) are highly discriminative between groups, unlike the difference between (3 Hz – 1 Hz). Both 5 Hz – 3 Hz (AUC = 0.879) and 5 Hz – 1 Hz (AUC = 0.808) BOLD differences-based discrimination curves are significant, P-value = 0.001 and P-

value = 0.007 respectively, reaching sensitivity 85.7% and specificity 84.6% in the former (solid red line in Fig 21D).

BOLD response in cortical and sub-cortical regions

The results of both whole-brain RFX-GLM, parametric analysis and ROC analysis in sub-cortical and cortical regions are presented in Fig 22. Significant activation in clusters located in Putamen, Globus Pallidus and Thalamus is observable in Fig 22A, showing the same whole-brain statistical RFX map described before. These clusters were used to draw the corresponding ROIs, then transformed in the grouped-ROI *sub-cortical*. The same map is shown in an inflated version of a template brain in Talairach space in Fig 22D, with the four described cortical regions highlighted. These clusters were used to draw the corresponding ROIs, then transformed in the grouped-ROI *cortical*.

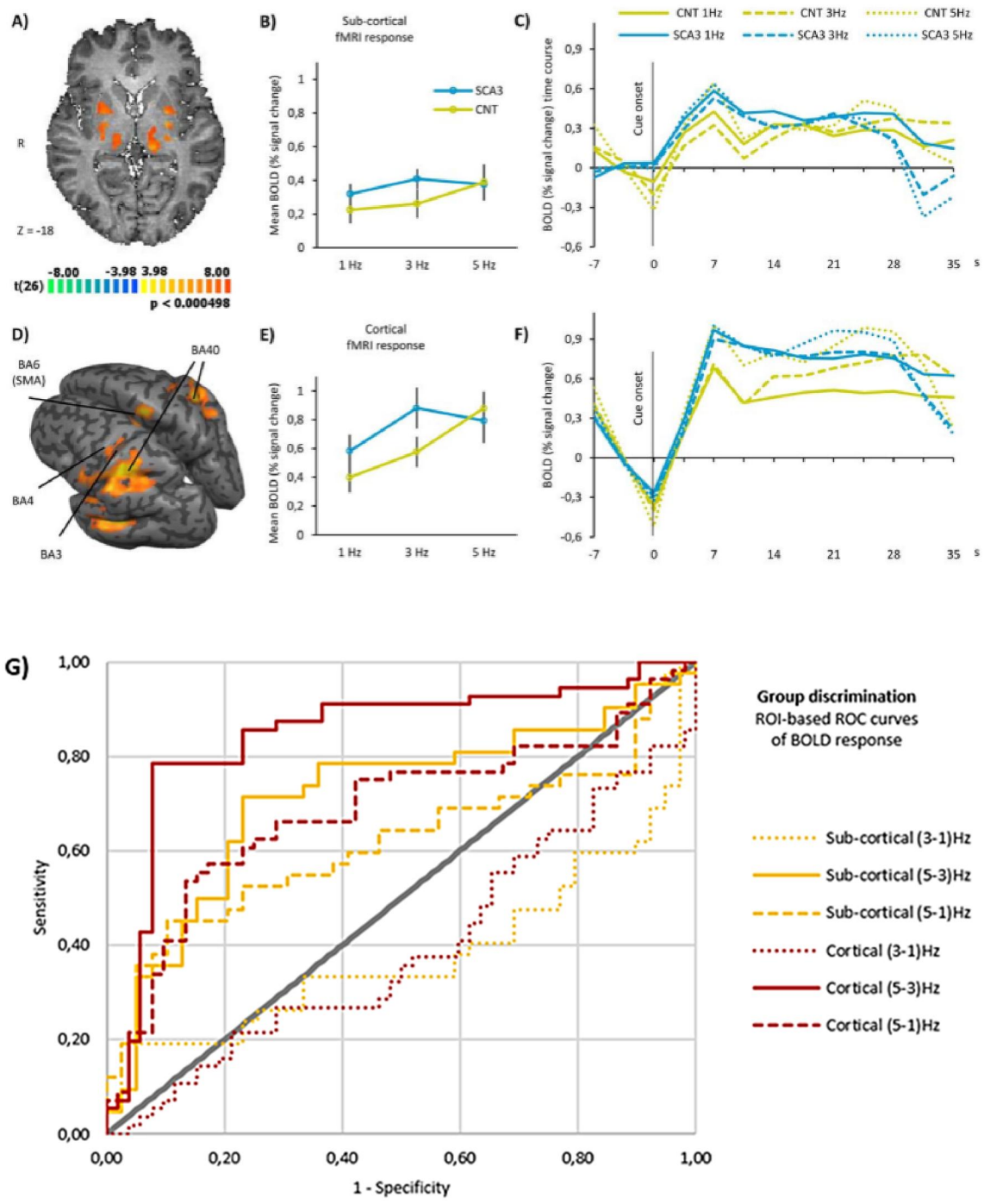

Figure 22: Functional MRI results in sub-cortical and cortical regions. A) Hand movement-related RFX statistical parametric map in axial section showing significant neuronal activation in Putamen, Globus Pallidus and Thalamus. Data are shown at a height threshold of P-value < 0.05 corrected for false discovery rate. B) Mean BOLD activity in SCA3 patients and controls within sub-cortical regions, during finger-tapping task. Data are presented as mean % signal change ± standard error of the mean. C) Averaged time course of the BOLD response in SCA3 and controls in sub-cortical regions, during finger-tapping task at the three prescribed frequencies. D) Hand movement-related RFX statistical parametric map in inflated template brain showing significant neuronal activation in BA3, BA4, BA6/SMA and BA40. Data are shown at a height threshold of P-value < 0.05 corrected for false discovery rate. E) Mean BOLD activity in SCA3 patients and controls within cortical regions, during finger-tapping

task. Data are presented as mean % signal change ± standard error of the mean. F) Averaged time course of the BOLD response in SCA3 and controls in cortical regions, during finger-tapping task at the three prescribed frequencies. G) Sensitivity analysis of BOLD signal in cortical (red lines) and sub-cortical (yellow lines) regions. We computed the ROC curve for the difference in BOLD signal between every two frequencies of finger-tapping. ROC curve analysis shows up to sensitivity 71.4% and specificity 76.9% (AUC = 0.717) to discriminate SCA3 patients from controls in sub-cortical regions. In cortical regions ROC analysis reached sensitivity 85.7% and specificity 76.9% (AUC = 0.846) in group discrimination.

Parametric analysis

Similarly to the cerebellum, the mean activation amplitude was higher in SCA3 patients, except for the most demanding frequency of 5 Hz, both in sub-cortical (Fig 22B) and cortical regions (Fig 22E). Furthermore, the variation of the BOLD response is also not able to fully trail the variation in the tapping frequency in SCA3 patients, unlike in control participants. In both the plots of the mean response and full response time courses (Fig 22C for sub-cortical regions and Fig 22F for cortical regions) we can observe that SCA3 patients are able to increase the BOLD response from tapping at 1 Hz to tapping at 3 Hz but not when they are asked to tap at 5 Hz. Control participants on the other hand are able to linearly increase BOLD response values within these two groups of regions whenever the prescribed frequency increases, they even show a more pronounced increase from 3 Hz to 5 Hz, particularly in the late part of the tapping periods (see Fig 22C and F).

In both sub-cortical and cortical regions we observed a significant interaction effect, between group and frequency of finger-tapping, in the BOLD response. Simple main effects revealed different effects of frequency variation in SCA3 patients and controls across sub-cortical and cortical regions.

Sub-cortical regions: Putamen, Globus Pallidus and Thalamus

The repeated-measures ANOVA showed a significant interaction between the effects of group and tapping frequency on BOLD response in sub-cortical regions, $F(2, 158) = 3.043$, P-value = 0.050, as presented in Table 8. SCA3 patients had a small main effect size ($\eta p^2 = 0.070$) of frequency that was not significant (P-value = 0.077). In controls the simple main effect in sub-cortical regions had a larger and significant effect size ($\eta p^2 = 0.115$, P-value = 0.012) (see Table 8). These results suggest predominant loss of the parametric effect in SCA3 in sub-cortical regions.

Cortical regions: BA3, BA4, BA6 (SMA) and BA40

The repeated-measures ANOVA revealed a statistically significant interaction between the effects of group and tapping frequency on BOLD response in cortical regions, F (2, 212) = 21.148, P-value < 0.001, as presented in the last column of Table 8. In the case of cortical regions both SCA3 patients and control participants had a significant main effect (P-value < 0.001), but the effect size was smaller in SCA3 patients ($\eta p^2 = 0.385$) than in controls ($\eta p^2 = 0.489$). When looking at the pairwise comparisons we observed that all were significant in control participants, while in SCA3 patients the increase from 3 Hz to 5 Hz finger-tapping did not yield a significant increase in BOLD response. These results suggest loss of the parametric effect in SCA3 in cortical regions as well.

Overall, in all analyzed ROIs the mean BOLD response was higher in SCA3 patients for finger-tapping at 1 Hz and 3 Hz but lower than in controls when tapping at the most demanding frequency of 5 Hz. This was due to the loss of parametric modulation of neuronal BOLD response by increasing tapping frequencies as also supported by the behavioral results (Table 5).

In sum neuroactivation was larger in SCA3 in a broad array of neocortical regions and the cerebellum, but SCA3 patients are not able to effectively maintain a parametric modulation of neuroactivation.

ROC analysis

We performed a sensitivity and specificity analysis of the BOLD response of SCA3 patients versus healthy controls in sub-cortical and cortical grouped-ROIs. Discrimination between early SCA3 patients and controls based on BOLD response to the parametric finger-tapping task is presented in Fig 22G. Note that, the way we computed the discrimination variables – BOLD difference between frequencies – allows the ROC curves to be symmetrically informative both in the upper or lower part of the graph, depending on whether the BOLD amplitude increases or decreases from one frequency to the other. As we have seen in the results of the parametric analysis, in the SCA3 group the BOLD response decreases from the 3 Hz to the 5 Hz frequency, while in control participants it increases.

Sub-cortical regions: Putamen, Globus Pallidus and Thalamus

We can observe that the difference in BOLD response at frequencies (5 Hz – 3 Hz) is highly discriminative between groups (AUC = 0.717, P-value = 0.001, sensitivity 71.4% and specificity 76.9% - solid yellow line in Fig 22G).

Cortical regions: BA3, BA4, BA6 (SMA) and BA40

We observed that the differences in BOLD responses at frequencies (5 Hz – 3 Hz) and (5 Hz – 1 Hz) are highly discriminative between groups. Both (5 Hz – 3 Hz, AUC = 0.846) and (5 Hz – 1 Hz, AUC = 0.688) BOLD differences-based discrimination curves are significant, (P-value < 0.001 and P-value = 0.001 respectively, sensitivity 85.7% and specificity 76.9% in the former - solid red line in Fig 22G).

References

Abe Y, Tanaka F, Matsumoto M, et al. CAG repeat number correlates with the rate of brainstem and cerebellar atrophy in Machado-Joseph disease. Neurology 1998;51:882-884.

Ashburner J. Computational anatomy with the SPM software. Magn. Reson. Imaging 2009;27(8):1163-1174.

Ashburner J, Friston KJ. Unified segmentation. Neuroimage 2005;26(3):839-51.

Ashburner J, Friston KJ. Voxel-Based Morphometry - The Methods. Neuroimage 2000;11(6):805-821.

Bettencourt C, Santos C, Montiel R, et al. The (CAG)n tract of Machado-Joseph Disease gene (ATXN3): a comparison between DNA and mRNA in patients and controls. Eur. J. Hum. Genet. 2010;18:621-623.

Beckmann CF, Jenkinson M, Smith SM. General multilevel linear modeling for group analysis in FMRI. Neuroimage 2003;20:1052-1063.

Bernard R, Goran D, Sakai S, et al. Cortical activation during rhythmic hand movements performed under three types of control: an fMRI study. Cogn. Affect. Behav. Neurosci. 2002;2(3):271-281.

Brainard DH. The Psychophysics Toolbox. Spat. Vis. 1997;10(4):433-436.

Buckner RL, Head D, Parker J, et al. A unified approach for morphometric and functional data analysis in young, old, and demented adults using automated atlas-based head size normalization: reliability and validation against manual measurement of total intracranial volume. Neuroimage 2004;23(2):724-738.

Carel C, Loubinoux I, Boulanouar K, et al. Neural Substrate for the Effects of Passive Training on Sensorimotor Cortical Representation : A Study With Functional Magnetic Resonance Imaging in Healthy Subjects. J. Cereb. Blood Flow Metab. 2000;20:478-484.

Coutinho P, Guimarães A, Scaravilli F. The pathology of Machado-Joseph Disease: Report of a possible homozygous case. Acta Neuropathol. 1982;58:48-54.

Coutinho P, Andrade C. Autosomal dominant system degeneration in Portuguese families of the Azores Islands: A new genetic disorder involving cerebellar, pyramidal, extrapyramidal and spinal cord motor functions. Neurology 1978;28:703-709.

Falcon M, Gomez C, Chen E, et al. Early Cerebellar Network Shifting in Spinocerebellar Ataxia Type 6. Cereb. cortex 2015;1-14.

Garrard P, Martin NH, Giunti P, Cipolotti L. Cognitive and social cognitive functioning in spinocerebellar ataxia: A preliminary characterization. J. Neurol. 2008;255:398-405.

Globas C, du Montcel ST, Baliko L, et al. Early symptoms in spinocerebellar ataxia type 1, 2, 3, and 6. Mov. Disord. 2008;23:2232-2238.

Hashimoto R-I, Javan AK, Tassone F, et al. A voxel-based morphometry study of grey matter loss in fragile X-associated tremor/ataxia syndrome. Brain 2011;134(3):863-878.

Hayasaka S, Phan KL, Liberzon I, et al. Nonstationary cluster-size inference with random field and permutation methods. Neuroimage 2004;22(2):676-687.

Horimoto Y, Matsumoto M, Yuasa H, et al. Brainstem in Machado-Joseph Disease: Atrophy or small size? Eur. J. Neurol. 2008;15:102-105.

Jardim LB, Pereira ML, Silveira I, et al. Neurologic Findings in Machado-Joseph Disease: Relation with disease duration, subtypes, and (CAG)n. Arch. Neurol. 2001;58:899-904.

Kawaguchi Y, Okamoto T, Taniwaki M, et al. CAG expansions in a novel gene for Machado-Joseph Disease at chromosome 14q32.1. Nat. Genet. 1994;8:221-228.

Kieling C, Rieder CRM, Silva ACF, et al. A neurological examination score for the assessment of spinocerebellar ataxia 3 (SCA3). Eur. J. Neurol. 2008;15:371-376.

Klockgether T, Kramer B, Lüdtke R, et al. Repeat length and disease progression in spinocerebellar ataxia type 3. Lancet 1996;348:830.

Kumada S, Hayashi M, Mizuguchi M, et al. Cerebellar degeneration in hereditary dentatorubral-pallidoluysian atrophy and Machado-Joseph disease. Acta Neuropathol. 2000;99:48-54.

Lanciego JL, Luquin N, Obeso J a. Functional neuroanatomy of the basal ganglia. Cold Spring Harb. Perspect. Med. 2012;2(12).

Lukas C, Hahn HK, Bellenberg B, et al. Spinal cord atrophy in spinocerebellar ataxia type 3 and 6: Impact on clinical disability. J. Neurol. 2008;255:1244-1249.

Maciel P, Costa M do C, Ferro A, et al. Improvement in the molecular diagnosis of Machado-Joseph Disease. Arch. Neurol. 2001;58:1821-1827.

Martins S, Calafell F, Wong VCN, et al. A multistep mutation mechanism drives the evolution of the CAG repeat at MJD/SCA3 locus. Eur. J. Hum. Genet. 2006;14:932-940.

Müller NG, Donner TH, Bartelt OA, et al. The functional neuroanatomy of visual conjunction search: a parametric fMRI study [Internet]. Neuroimage 2003;20(3):1578-1590.[cited 2013 Apr 8] Available from: http://linkinghub.elsevier.com/retrieve/pii/S1053811903004166

Murata Y, Yamaguchi S, Kawakami H, et al. Characteristic magnetic resonance imaging findings in Machado-Joseph Disease. Arch. Neurol. 1998;55:33-37.

Ogawa S, Lee T-M, Nayak AS, Glynn P. Oxygenation-sensitive contrast in magnetic resonance image of rodent brain at high magnetic fields. Magn. Reson. Med. 1990;14(1):68-78.

Pelli DG. The VideoToolbox software for visual psychophysics: transforming numbers into movies. Spat. Vis. 1997;10(4):437-442.

Penny W, Holmes A, Friston KJ. Random effects analysis in Human Brain Function. London: Academic Press; 2003.

Pillai JJ. The evolution of clinical functional imaging during the past 2 decades and its current impact on neurosurgical planning. Am. J. Neuroradiol. 2010;31:219-225.

Riecker A, Wildgruber D, Mathiak K, et al. Parametric analysis of rate-dependent hemodynamic response functions of cortical and subcortical brain structures during auditorily cued finger tapping: an fMRI study. Neuroimage 2003;18(3):731-739.

Rosenberg RN, Nyhan WL, Bay C, Shore P. Autosomal dominant striatonigral degeneration: A clinical, pathologic, and biochemical study of a new genetic disorder. Neurology 1976;26:703-714.

Rüb U, de Vos RAI, Schultz C, et al. Spinocerebellar ataxia type 3 (Machado-Joseph Disease): severe destruction of the lateral reticular nucleus. Brain 2002;125:2115-2124.

Rüb U, Brunt ER, De Vos RAI, et al. Degeneration of the central vestibular system in spinocerebellar ataxia type 3 (SCA3) patients and its possible clinical significance. Neuropathol. Appl. Neurobiol. 2004;30:402-414.

Schmitz-Hübsch T, Du Montcel ST, Baliko L, et al. Scale for the assessment and rating of ataxia: Development of a new clinical scale. Neurology 2006;66:1717-1720.

Schöls L, Bauer P, Schmidt T, et al. Autosomal dominant cerebellar ataxias: clinical features, genetics, and pathogenesis. Lancet. Neurol. 2004;3:291-304.

Stefanescu MR, Dohnalek M, Maderwald S, et al. Structural and functional MRI abnormalities of cerebellar cortex and nuclei in SCA3, SCA6 and Friedreich's ataxia. Brain 2015;138:1182-1197.

Swami M, Hendricks AE, Gillis T, et al. Somatic expansion of the Huntington's disease CAG repeat in the brain is associated with an earlier age of disease onset. Hum. Mol. Genet. 2009;18(16):3039-3047.

Takiyama Y, Igarashi S, Rogaeva EA, et al. Evidence for inter-generational instability in the CAG repeat in the MJD1 gene and for conserved haplotypes at flanking markers amongst Japanese and Caucasian subjects with Machado-Joseph Disease. Hum. Mol. Genet. 1995;4:1137-1146.

Witt ST, Meyerand ME, Laird AR. Functional neuroimaging correlates of finger tapping task variations: An ALE meta-analysis. Neuroimage 2008;42(1):343-356.

Woods BT, Schaumburg HH. Nigro-spino-dentatal degeneration with nuclear ophthalmoplegia: A unique and partially treatable clinico-pathological entity. J. Neurol. Sci. 1972;17:149-166.

Worsley KJ, Andermann M, Koulis T, et al. Detecting changes in nonisotropic images. Hum. Brain Mapp. 1999;8(2-3):98-101.

Wurster CD, Graf H, Ackermann H, et al. Neural correlates of rate-dependent finger-tapping in Parkinson's disease. Brain Struct. Funct. 2015;220:1637-1648.

Yamada M, Hayashi S, Tsuji S, Takahashi H. Involvement of the cerebral cortex and autonomic ganglia in Machado-Joseph disease. Acta Neuropathol. 2001;101:140-144.

CHAPTER 5

Discussion and conclusion

Discussion and conclusion

This study show the evidence of cortico-cerebellar functional dissociation in early MJD/SCA3 patients during a parametric motor tapping task, where different pacing rates were imposed to vary performance load. This parametric design allowed to discriminate with high specificity and sensitivity between patients and controls across brain regions beyond the cerebellum. The tapping task paced by a series of periodic auditory signals (1-3-5 Hz) yielded significant BOLD effects within the cerebellum and several cortical and sub-cortical areas characterized by distinct rate/response functions in SCA3 patients compared to controls.

We found significant activation in the anterior part of the cerebellum. However volumes of activation of this structure did not discriminate between SCA3 patients and controls, unlike rate dependent changes in BOLD response signals. Among others, cerebellar disorders give rise to slowed and more irregular movements during finger-tapping (Riecker et al., 2003). In accordance with this, activation volumes (a functional morphometry measure) in the cerebellum were correlated significantly with measured motor task performance at the most demanding frequency (see Table 7). This result supports previous findings of the significant contribution of the cerebellum to repetitive finger movements to be restricted to faster rates above a level of about 3 Hz (Riecker et al., 2003). Furthermore, we found motor performance to be significantly diminished in SCA3 group (Table 5), corroborated by ROC analysis of behavioural data, which showed significant discrimination power between patients and controls.

In addition to the significant rate dependent difference in cerebellar activation levels found between groups functional MRI findings in this study show a consistent pattern of activations in both groups in Brodmann area 40 (BA40). BA40 is involved in somatosensory processing as well as of repetitive passive movements (Carel et al., 2000). Moreover, we also found neuronal activations in BA3, BA4 and BA6. BA3 includes the somatosensory cortex and lesions affecting this region produce astereognosia, which can be related to the task employed in this study (Bernard et al., 2002). BA4 includes the primary motor cortex, and is connected to anterior BA6. BA6 (premotor cortex and supplementary motor area, SMA) receives input from cerebellum and is involved in sensory guidance and planning of coordinated movements based on external cues.

Finally, the activation paradigm also revealed significant clusters in sub-cortical regions: putamen, globus pallidus and thalamus. The motor circuitry originates in several frontal areas and projects mainly to the putamen, and that information is returned via ventrolateral thalamus back to the neocortex (Riecker et al., 2003). Besides this "direct" putaminal–pallidal pathway, the striatum targets the basal ganglia output stage via the external segment of the globus pallidus and the subthalamic nucleus ("indirect" pathway) (Riecker et al., 2003; Lanciego et al., 2012). Here, we found significantly different BOLD responses within the indirect motor circuitry of the basal ganglia between SCA3 patients and controls.

The significant activation of these regions beyond cerebellar activation in SCA3 patients might also represent a mechanism of compensation. This whole brain mechanism is reminiscent of the early intracerebellar network shifting that is observed in spinocerebellar ataxia type 6 (Falcon et al., 2015).

Importantly, our parametric design enabled group discrimination with high sensitivity and specificity. The striking pattern of cortico-cerebellar modulation of activity was characterized by hyperactivation at the least demanding frequencies (1 Hz and 3 Hz), particularly in cortical regions, and decreased activation at the most demanding frequency (5 Hz), particularly in the cerebellum, in SCA3 patients as compared to healthy controls. Interestingly, principally in cortical regions, the mean BOLD response is much higher in SCA3 patients than in controls for 1 Hz and 3 Hz, revealing a possible compensatory recruitment of sensorimotor areas to overcome cerebellum dysfunction. However, when participants were asked to finger tap at 5 Hz BOLD response decreased in all analyzed regions, suggestion that patients had surpassed the dynamic range of maintained function. Accordingly, in control participants the frequency variation had a linear parametric effect on BOLD signal modulation in all regions, while in SCA3 patients the parametric effect was lost and both performance and BOLD responses collapsed from 3 Hz to 5 Hz. This differential modulation of BOLD signal in response to variation in the frequency of the finger-tapping task revealed to be a significant discrimination tool between SCA3 patients and controls, as supported by the sensitivity ROC analysis of the fMRI signal.

To conclude, the striking early rate dependent cortico–subcortical pattern of activation, beyond the cerebellum, seen in coupled behavioural and parametric fMRI measurements suggest a possible role for whole brain fMRI as a potential useful tool for clinical evaluation of MJD/SCA3 patients before overt disease manifestations, as

corroborated by ROC analysis of both behavioural and imaging data. Our results suggest that functional measures (morphometric and non-morphometric) provide added value and may outperform conventional anatomical voxel based morphometry.

References

Bernard R, Goran D, Sakai S, et al. Cortical activation during rhythmic hand movements performed under three types of control: an fMRI study. Cogn. Affect. Behav. Neurosci. 2002;2(3):271-281.

Carel C, Loubinoux I, Boulanouar K, et al. Neural Substrate for the Effects of Passive Training on Sensorimotor Cortical Representation : A Study With Functional Magnetic Resonance Imaging in Healthy Subjects. J. Cereb. Blood Flow Metab. 2000;20:478-484.

Falcon M, Gomez C, Chen E, et al. Early Cerebellar Network Shifting in Spinocerebellar Ataxia Type 6. Cereb. cortex 2015;1-14.

Lanciego JL, Luquin N, Obeso J a. Functional neuroanatomy of the basal ganglia. Cold Spring Harb. Perspect. Med. 2012;2(12).

Riecker A, Wildgruber D, Mathiak K, et al. Parametric analysis of rate-dependent hemodynamic response functions of cortical and subcortical brain structures during auditorily cued finger tapping: an fMRI study. Neuroimage 2003;18(3):731-739.